ACIBADEM MEHMET ALI AYDINLAR UNIVERSITY
INSTITUTE OF HEALTH SCIENCES

DEVELOPMENT OF 3D-BIOPRINTED GLIOBLASTOMA MODEL TO MIMIC *IN VIVO* TUMOR MICROENVIRONMENT

ŞEYMA IŞIK

PH.D. THESIS

DEPARTMENT OF MEDICAL BIOTECHNOLOGY

SUPERVISOR
Prof. Vasıf Nejat HASIRCI

SECONDARY SUPERVISOR
Assoc. Prof. Deniz YÜCEL

ISTANBUL-2025

ACIBADEM MEHMET ALI AYDINLAR UNIVERSITY
INSTITUTE OF HEALTH SCIENCES

DEVELOPMENT OF 3D-BIOPRINTED GLIOBLASTOMA MODEL TO MIMIC *IN VIVO* TUMOR MICROENVIRONMENT

ŞEYMA IŞIK

PH.D. THESIS

DEPARTMENT OF MEDICAL BIOTECHNOLOGY

SUPERVISOR
Prof. Vasıf Nejat HASIRCI

SECONDARY SUPERVISOR
Assoc. Prof. Deniz YÜCEL

ISTANBUL-2025

DECLARATION

I declare that this thesis work is my own work, I had no unethical behavior at any stages from the planning to the writing of the thesis, I obtained all the information in this thesis in accordance with academic and ethicel rules, I cited all the information and comments that were not obtained with this thesis work, and I provided resources in the list of references. I also declare that there was no violation of any patents and copyrights during the study and writing of this thesis.

13/10/2025

Şeyma Işık

PREFACE AND ACKNOWLEDGEMENT

Statistician George Box quoted that “All models are wrong, but some are useful.” This perspective has guided my thinking throughout this thesis. Rather than pursuing absolute correctness, I’ve come to value what brings clarity, relevance, and impact in real world settings. This mindset not only shaped how I approached problems in this thesis but also reminded me that the true worth of scientific work often lies in its ability to inform, guide, and serve beyond theory.

I would like to express my gratitude to my advisor, Prof. Vasıf Hasırcı, for his invaluable guidance, support, and encouragement throughout my research. His insights have played a crucial role in shaping this work and in my development as an independent researcher. I would also like to thank my co-advisor, Assoc. Prof. Deniz Yücel, for her kind support and thoughtful contributions during this process. I would like to extend my appreciation to the members of my thesis committee, Prof. Özge Can, Prof. Gamze Torun Köse and Prof. Dr. Semih Keskil for their valuable time, comments, and evaluation, which contributed significantly to the improvement of this study.

I sincerely thank my colleagues and labmates for their support, ideas, and teamwork throughout this study. I am thankful to my dear frentors, Gözde Ervin Köle, Neval Sevinç, and Deniz Başöz, whose kindness, humor, and unwavering support made even the most challenging days manageable and memorable. I feel truly fortunate to have shared this journey with them. I am grateful to all members of the ACU Biomaterials Center, Prof. Halime Kenar, Şimal Yaren Şahin, Arden Çınar, and Tuna Özürün, for their collaborative spirit and consistent support.

I would like to thank Prof. Nesrin Hasırcı for being an inspiring presence as a strong and successful woman in science. I would also like to thank Dilara Tamay, Damla Arslantunalı Şahin and Hilal Selamet for their collaboration, dedication, and support throughout our projects. Their contributions made this journey both more productive and enjoyable.

I am truly grateful to Tuğçe Doğruel, Kübra Coşkun, Feyza Erdemir, Furkan Şahin, Müge Serhatlı and Kübra Akalın for their genuine friendship and invaluable support throughout this journey. Their presence, encouragement, and thoughtful contributions made a meaningful difference.

Above all, I am deeply thankful to my family, who have been the unwavering foundation behind every step I've taken. Their lifelong support, sacrifices, and constant encouragement have shaped the person I am today. I am profoundly grateful to my husband, Mert Işık, whose unwavering support, quiet strength, and unconditional love carried me through every high and low of this journey. His presence has been both my anchor and my light, a constant reminder of how incredibly lucky I am to walk this path with him.

A very special thank you to my little sister Ceren, whose endless energy, laughter, and unconditional love have been a constant source of joy and inspiration in my life.

To Luther, my dearest Son, whose quiet presence gave this journey a kind of meaning that words could never fully express. You remind me every day of what truly matters. For that, and all the serenity and calm, I am deeply thankful.

This study was funded by the Scientific and Technological Research Council of Turkey (TUBITAK) under Grant No 323S338, and by the Scientific Research Projects Coordination Unit of Acıbadem University under Project No 2312. I thank TUBITAK and Acıbadem University for their support, and ACU Biomaterials Center for providing access to their research facilities. I also acknowledge the support of TUBITAK through the 2211-C National Ph.D. Scholarship Program.

TABLE OF CONTENTS

ABBREVIATIONS AND SYMBOLS

3D	Three dimensional
BCA	Bicinchoninic acid
$CaCl_2$	Calcium chloride
CD44	Cluster of differentiation 44
CHI3L1	Chitinase-3-like protein 1
DAPI	4',6-diamidino-2-phenylindole
dECM	Decellularized extracellular matrix
DMEM	Dulbecco's modified eagle's medium
DMMB	1,9-dimethylmethylene blue
DNA	Deoxyribonucleic acid
ECM	Extracellular matrix
EGFP	Enhanced green fluorescent protein
EGFR	Epidermal growth factor receptor
FTIR	Fourier transform infrared spectroscopy
G′	Elastic modulus
G″	Viscous modulus
GAG	Glycosaminoglycan
GAPDH	Glyceraldehyde-3-phosphate dehydrogenase
GFAP	Glial fibrillary acidic protein
GBM	Glioblastoma multiforme
HAMA	Hyaluronic acid methacrylate
HCl	Hydrochloric acid
H&E	Hematoxylin eosin
HIF1A	Hypoxia-inducible factor 1-alpha
IC_{50}	Half maximal inhibitory concentration
IDH	Isocitrate dehydrogenase
LVR	Linear viscoelastic region
$MgCl_2$	Magnesium chloride
MMP2	Matrix metallopeptidase 2

MMP9	Matrix metallopeptidase 9
Mw	Molecular weight
NaOH	Sodium hydroxide
OCT	Optimal cutting temperature
PDMS	Polydimethylsiloxane
PTEN	Phosphatase and tensin homolog
RNA	Ribonucleic acid
RT-PCR	Reverse transcription polymerase chain reaction
SDS	Sodium dodecylsulfate solution
SEM	Scanning electron microscopy
SOX2	SRY-Box transcription factor 2
TERT	Telomerase reverse transcriptase
TGF-β	Transforming growth factor beta
TME	Tumor microenvironment
TMZ	Temozolomide

LIST OF FIGURES

LIST OF TABLES

ABSTRACT

Development of 3D-Bioprinted Glioblastoma Model to Mimic *In Vivo* Tumor Microenvironment

Glioblastoma (GBM) represents one of the most aggressive primary brain tumors, known for a complex microenvironment that promotes invasion, resistance to treatment, and recurrence. In this study, a bioprinted GBM model was developed by integrating hyaluronic acid methacrylate (HAMA) with decellularized brain extracellular matrix (dECM), preparing a bioink that closely mimics the biochemical composition and mechanical properties of native brain tissue. The compressive modulus of the composite hydrogels was measured at 9.44 ± 0.73 kPa, while the elastic modulus was found to be 458.30 ± 13.39 Pa, close to that of native GBM tissue. By preserving the biochemical components of the brain, the hydrogels contributed to essential cellular activities such as adhesion, invasion and matrix remodeling, which are pivotal for replicating the highly invasive and adaptive nature of glioblastoma. The model was created by compartmental co-culturing glioblastoma (U87) and microglia (HMC3) cells in mimicking the cellular interactions between tumor and microenvironment. Co-culturing with microglia distinctly increased glioblastoma progression, as shown by the 43% increase in Ki67 expression and 41% increase in invasion distance. Furthermore, the chip model replicated the hypoxic gradients typically observed in GBM tumors. This *in vitro* model reproduced key pathological characteristics of GBM, including pseudopalisading necrosis, hypoxia induced gene expression, invasion and cellular heterogeneity. Finally, the model demonstrated its potential as a drug screening platform during the determination of the IC_{50} for temozolomide, which showed reduced drug sensitivity under hypoxic conditions, further supported by the upregulation of resistance related genes including SOX and NES. This physiologically relevant *in vitro* system is a promising tool to study glioblastoma biology and therapeutic strategies.

Keywords: Glioblastoma microenvironment, Tissue engineering, *In vitro* models, 3D bioprinting

ÖZET

In Vivo Tümör Mikro Ortamını Taklit Etmek İçin 3B-Biyobasılı Glioblastoma Modelinin Geliştirilmesi

Glioblastoma (GBM), yüksek invazifliği, tedaviye dirençli yapısı ve tekrarlama eğilimi ile bilinen en agresif beyin tümörlerinden biridir. Bu çalışmada, hyalüronik asit metakrilat (HAMA) ve hücresizleştirilmiş beyin ekstrasellüler matriksi (dECM) kullanılarak doğal dokuyu biyokimyasal ve mekanik açıdan taklit eden bir GBM modeli geliştirilmiştir. Mekanik olarak, bu kompozit hidrojeller 9.44 ± 0.73 kPa'lık bir basma modülü ve 458.30 ± 13.39 Pa'lık bir elastik modül sergileyerek doğal GBM dokusunu taklit etmiştir. Beyin ECM'inin biyokimyasal bileşenlerini büyük ölçüde içeren hidrojeller, hücre yapışması, matriksin yeniden yapılandırılması ve invazyon gibi temel biyolojik süreçleri etkin biçimde yansıtmıştır. Model, tümör mikroçevresindeki hücresel etkileşimleri taklit etmek amacıyla glioblastoma (U87) ve mikroglia (HMC3) hücrelerin birlikte kültürlenmesini kapsamaktadır. Bu kültür, Ki67 ekspresyonunda %43'lük ve invazyon uzaklığında %41'lik bir artışla glioblastoma agresifliğini önemli bir düzeyde artırmıştır. Ayrıca, GBM tümörlerine özgü hipoksik gradyanlar *in vitro* çip sisteminde oluşturulabilmiştir. Geliştirilen bu hipoksi modeli, pseudopalisadik nekroz, hipoksiye bağlı gen ekspresyonu, invazyon ve hücresel heterojenlik gibi GBM'ye özgü patolojik özellikleri iyi bir şekilde taklit etmiştir. Buna ek olarak, modelin bir anti kanser ilacı olan temozolomide karşı duyarlılığını belirlemek amacıyla yapılan testlerde, modelin klinik öncesi ilaç tarama platformu olarak kullanılabilir olduğu gösterilmiştir. Hipoksik koşullar altında azalan ilaç duyarlılığı, direnç mekanizmalarında yer alan genlerin ekspresyonundaki artışla birlikte moleküler düzeyde desteklenmiştir. Geliştirilen bu *in vitro* model, glioblastoma biyolojisinin daha iyi anlaşılmasını ve yeni tedavi stratejilerinin geliştirilmesini sağlayarak *in vivo* deneyleri azaltma potansiyeli de taşımaktadır.

Anahtar Sözcükler: Glioblastoma mikroçevresi, Doku mühendisliği, *In vitro* modeller, 3B biyobasım

1 INTRODUCTION AND AIM

1.1 Impact of the Tumor Microenvironment on Glioblastoma Progression and Therapeutic Strategies

Glioblastoma (GBM) is a deadly adult brain tumor with a high recurrence rate and resistance to treatment. Every year, an estimated 17,000 new patients are diagnosed with GBM, at a rate of 3.19 cases per 100,000 persons (1). GBM pathogenesis is the sequential accumulation of genetic abnormalities and inadequate regulation of growth factors signaling pathways that lead to malignant transformation. The current standard of care for GBM is surgery followed by irradiation and chemotherapy, which has yet to produce satisfactory results (2). Overall survival duration is 3-6 months after surgical excision of the tumor. Postoperative radiation (RT) is the main option after surgical resection. Since the 1970s, this has been considered standard therapy. The introduction of radiotherapy to the treatment protocol increases the life expectancy to 12.1 months, 10.4% (2-year survival percent). Since 2005, temozolomide (TMZ) has been recommended as the first line treatment for newly diagnosed GBM patients after surgery and concomitant RT (3). Despite great tolerance towards TMZ, only about a third of GBM patients respond to alkylating drugs because others have innate or acquired chemoresistance. The combination of concomitant and adjuvant TMZ treatment can result in a slight increase in survival to 14.6 months, 26.5% (2 year survival percent) (4). These indicate that, even though we now have a better understanding of GBM genetics, biology, and microenvironment than in the past, it is still mainly incurable today. The management of GBM patients is complicated due to a variety of reasons. These factors include tumor location, inter and intratumor heterogeneity, comlex tumor microenvironment, invasive nature of GBM, the status of molecular markers, chemotherapeutic drug delivery, and resistance (5). Despite the years of research and technological advances, the prognosis for GBM has not improved significantly. For decades, studies focusing on the genetic and molecular alterations that occur in cancer cells and their contributions to unregulated cell proliferation have primarily shaped our understanding of GBM biology. However, GBM growth is highly dependent on growth regulatory signals that originate from the

tumor microenvironment. The interaction between the microenvironment and glioblastoma cells promotes tumor growth, proliferation, immune surveillance, and resistance to therapeutic agents (6). Presence of *in vitro* models to test drug candidates and understand the disease mechanism would have enabled move tests under well-defined conditions of a model.

1.2 Objective and Significance of the Developed *In Vitro* Model

Before clinical trials, drugs are tested first on cell cultures and then on animals to evaluate their effectiveness and safety; however, these models do not completely reflect human physiology. In order to decrease the risk of any undesirable reaction in humans, the *in vivo* experiments use a large number of animals. This highlights the urgent need for advanced *in vitro* models that can better replicate the biological and biomechanical features of diseases, in this case, glioblastoma, providing a more reliable platform for preclinical testing, bridging the gap to clinical studies, and enabling a deeper understanding of the underlying mechanisms.

Considering the necessity for a tissue model that reflects the essential properties of the native microenvironment, it was aimed to develop a glioblastoma model that mimics the tumor microenvironment. The GBM model aimed to replicate the tumor microenvironment by creating a hypoxic gradient that is a property of glioblastoma tumors, mimicking the biological composition and mechanical properties of ECM, and simulating the GBM-microglia interactions in a synergic manner. Although recent models are quite advanced, replicating the complete microenvironment remains a challenge, as none of them represent the native ECM, GBM-microglia interactions, and hypoxic features simultaneously. This study aimed to develop a GBM model that could better mimic *in vivo* tumor environment and offer a more precise platform for drug efficacy testing. Earlier models used molecules such as hyaluronic acid, decellularized patient tissues, collagen, and fibrinogen (7-9), which could replicate certain structural aspects of the tumor to a limited extent. However, they lacked the biochemical and mechanical complexity characteristic of the native ECM. For instance, hyaluronic acid based models (7) did not accurately replicate the native ECM

composition, as they lacked key polysaccharides and structural proteins. Decellularized ECM from brain tissue preserves the natural composition of the ECM (10), and in this study, decellularized brain tissue was used to closely mimic the biological composition of the native GBM ECM. Decellularized brain tissue was used in earlier GBM models (11), but mechanical strength was not mimicked. Moreover, printing using dECM has limitations such as low resolution and prolonged crosslinking (about 1 h) which hinder the formation of realistic, layered structures. Combining decellularized brain ECM with hyaluronic acid methacrylate was used to strengthen the mechanical properties. The low dose of UV exposure used was found to be not harmful to cells (12). Further, considering the hyaluronic acid rich environment of glioblastoma, incorporating HAMA helps introducing this critical component in resulting matrix, thereby better simulating native tissue composition. Another aim for appropriate mimicking in this study was to create a hypoxic gradient in the model. In order to achieve hypoxic conditions, different strategies have been followed. Hypoxia chambers offer a basic approach but are limited to control of precise oxygen levels (13). Microfluidic systems that adjust O_2 levels through gas channels (14, 15) are effective but require a complex setup. Enzyme based methods using oxygen consuming agents (e.g., glucose oxidase) generate H_2O_2, limiting their use in cell studies due to toxicity (16). The approach used in this study involves a diffusion barrier to establish oxygen gradients, eliminating complex systems or toxic agents. Similar diffusion barrier methods, such as PMMA layers (17) and PC films (18), have also successfully created hypoxic gradients. However, these closed systems had problems integrating layered structures and diverse cell types. Our model is able to integrate both multicellular layered structures and organotypic cultures in one setup, offering a more flexible system. This allows the production of precise internal structures and layering of different cells and materials, enabling a more functional model.

This study aims to create an *in vitro* glioblastoma model that integrates native ECM components, hypoxia gradients, and GBM microglia interactions to replicate the tumor microenvironment more accurately, allowing better understanding of GBM progression, and a reliable drug efficacy testing.

2 BACKGROUND

2.1 GBM Pathogenesis and Clinical Challenges

Glioblastoma multiforme (GBM) represents the most aggressive and deadly primary brain tumor in the central nervous system. It is classified as Grade IV astrocytoma by the World Health Organization (WHO) (19), and is pathologically known for characteristics such as extensive proliferation, microvascular hyperplasia, and pseudopalisading necrosis which help its highly infiltrative growth and resistance to therapy (20-22). GBM originates from genetic mutations, epigenetic alterations, and dysregulated molecular signaling. These changes disrupt molecular pathways involved in cell cycle regulation, DNA repair, apoptosis, and metabolic homeostasis. There are two subtypes of GBM, primary and secondary GBM. Primary GBM arises *de novo* and is common in older patients, often is IDH-wild type and has alterations such as TERT promoter mutations, EGFR amplification, PTEN deletions, and chromosomal abnormalities including a gain of chromosome 7 and loss of chromosome 10 (23-25). On the other hand, secondary GBM progresses from lower grade gliomas and affects younger individuals (26) and is characterized by P53 and IDH mutations (27-30).

GBM progression is driven by tumor intrinsic factors with GBM cells existing in four main transcriptional states including mesenchymal-like (MES-like), neural progenitor-like (NPC-like), astrocyte cell-like (AC-like), and oligodendrocyte progenitor-like (OPC-like), and they are highly plastic which allow transitions between states within single tumors (31, 32). This heterogeneity of distinct subclones with varied therapy responses complicates treatment (33). Notably, recurrent GBMs display increased cellular diversity, including stemness and proliferation-linked subclones, and introduces resistance and invasiveness (34). In addition to this cellular diversity, recurrent GBMs often show O6-methylguanine-DNA methyltransferase (MGMT) overexpression, which increases resistance to TMZ by repairing DNA damage (35). Standard clinical management includes surgical resection, radiotherapy, and concomitant chemotherapy with TMZ, however, the median survival time for

GBM patients remains approximately 15 months and a five-year survival rate is below 10% (4). GBM progression is further shaped by complex and dynamic tumor microenvironment complicating the treatment (36).

2.2 Tumor Microenvironment

Tumor microenvironment (TME) is a complex network of cellular and extracellular components that drive tumor progression. The cells include cancer stem cells (GSCs), astrocytes, neurons, endothelial cells, and immune cells such as tumor-associated microglia and macrophages (TAMs), myeloid-derived suppressor cells (MDSCs), and regulatory T cells (Tregs). The non-cellular components consist of the extracellular matrix (ECM), which provides structural and biochemical support (37-40). GBM TME consists of spatially distinct regions (Figure 1) including the necrotic core which is mechanically soft due to severe hypoxia and vascular occlusion, leading cell death. Pseudopalisading regions consist of a high density of migrating cells surrounded by hypoxic zones with increased stiffness and ECM deposition. In hypervascular zones, GBM shows abnormal, leaky neovasculature, causing increased interstitial fluid pressure. The infiltrative rim contains invaded GBM cells in a healthy parenchyma along myelinated tracts, and the perivascular niche where tumor cells invade the vasculature (21, 41, 42).

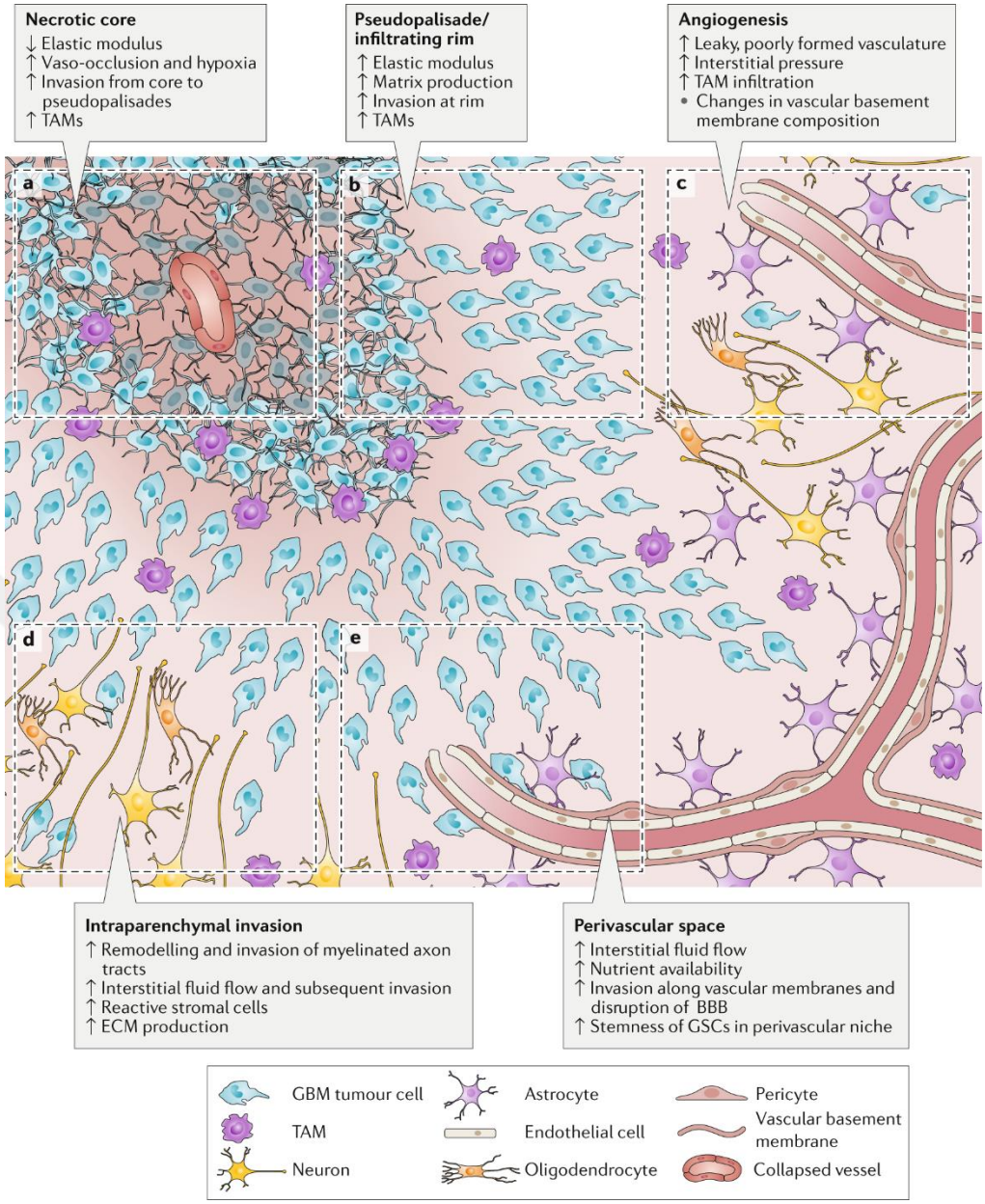

Figure 1 Schematic presentation of glioblastoma microenvironment across distinct spatial regions. Adapted with permission (41).

The ECM of the brain is a highly specialized and tightly regulated network that plays a significant role in maintaining neural homeostasis. Unlike the ECM in other tissues, the brain ECM is uniquely soft, highly hydrophilic, and lacks abundant structural proteins, which are predominantly composed of hyaluronic acid, chondroitin sulfate proteoglycans (CSPGs), tenascin-R, and minimal amounts of collagen IV and laminin (Figure 2). This composition creates a hydrated, loosely organized, and low

stiffness matrix that supports normal brain physiology, including cellular communication and neurovascular integrity (9, 43-45). During GBM progression, this balance is disrupted through biochemical and mechanical remodeling of the ECM (46). GBM and stromal cells secrete matrix remodeling enzymes including matrix metalloproteinases, hyaluronidases, and cathepsins that degrade the native matrix and enable cellular infiltration. Also, abnormal ECM deposition occurs with the accumulation of components such as collagens I, III, VI, fibronectin, periostin, osteopontin, and SPARC, which remodel the ECM into a stiff, fibrotic, and mesenchymal-like microenvironment (47, 48).

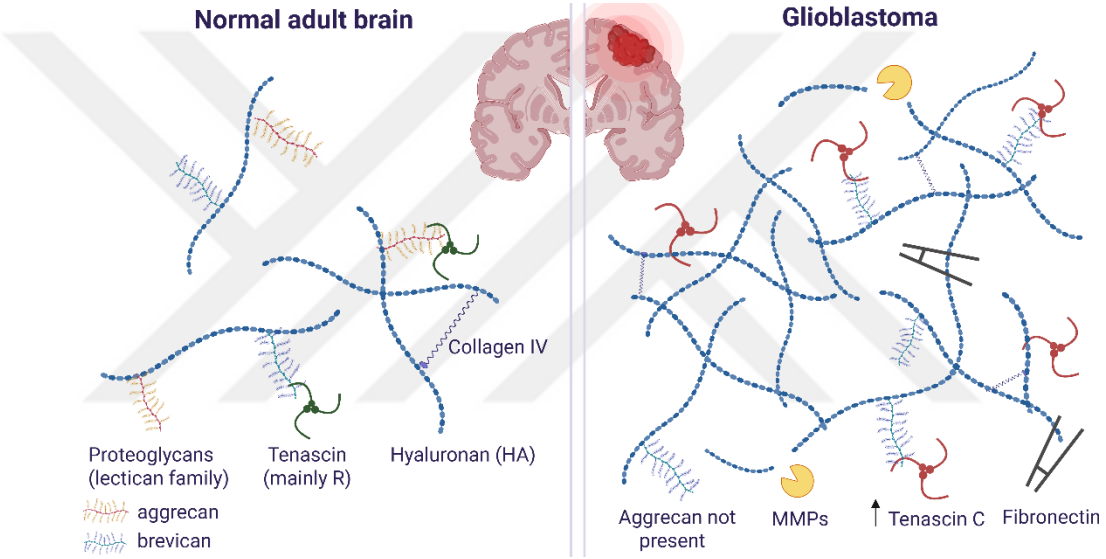

Figure 2 Schematic overview of glioblastoma ECM. In healthy brain tissue, ECM is characterized by low stiffness and the absence of neurodevelopmental proteins, while the GBM ECM becomes denser, stiffer, and enriched in oncogenic components (e.g., tenascin-C, fibronectin), facilitating invasion and angiogenesis. (Adapted from Biorender).

Hyaluronic acid (HA), a key constituent of the ECM in healthy brain tissue, undergoes significant alterations in GBM, leading to the formation of a dense and disorganized viscoelastic matrix (49). These changes are induced through the upregulation of hyaluronidases, hyaluronan synthases, CD44, and RHAMM (46, 50, 51). This increased and altered HA composition promotes tumor cell migration, angiogenesis, and immune evasion. The ECM remodeling was primarily driven by the

upregulated expression of matrix metalloproteinases (MMPs) which degrade ECM components, enable tumor-specific matrix deposition, and create pathways for tumor cell invasion into the surrounding healthy brain (52-54).

Collagen constitutes only a small fraction of healthy brain ECM (primarily localized in the basement membrane) and becomes significantly upregulated in GBM. Collagen supports glioblastoma cell adhesion, migration, and survival through interactions with integrins, activating signaling pathways that promote tumor invasion and resistance to apoptosis (55, 56). Fibronectin is also upregulated in GBM which facilitates cell adhesion and proliferation, thereby promoting the invasive and proliferative behavior of glioblastoma (45). Laminin is overexpressed in GBM, especially in the perivascular niche that supports glioblastoma stem cell maintenance. Laminin interacts with integrins to promote tumor cell adhesion, migration, and maintenance of stem-like properties by activating signaling pathways (43, 56-58).

Tenascin-C (TNC) as a glycoprotein is present at very low levels in healthy brain ECM but becomes a major component of the GBM ECM. Unlike its neural isoform tenascin-R, TNC disrupts adhesion, modulates integrin and syndecan signaling, and activates oncogenic cascades. It further contributes to GSC maintenance and immune evasion, thereby promoting tumor heterogeneity and compartmentalization (9, 45, 59, 60).

Biomechanical properties of the ECM in glioblastoma are also significantly altered. Increased fibrillar proteins, lysyl oxidase (LOX) mediated crosslinking, and cell driven matrix deposition collectively increase tissue stiffness (61, 62). In healthy brain tissue, the Young's modulus is around 1 kPa (63, 64), whereas in high grade GBMs, it increases dramatically, reaching up to 11.4 ± 4.9 kPa (65). Importantly, ECM stiffness in GBM is spatially heterogeneous that tumor periphery is mechanically stiffer than the necrotic core, creating a stiffness gradient that guides invasive behavior (66). The increased stiffness is not just a consequence of tumor growth, but an active contributor to malignancy. It serves as a barrier to drug diffusion, elevates interstitial pressure, and activates survival programs that mitigate the effects of chemotherapy

and radiotherapy. It activates mechanosensitive pathways such as YAP/TAZ, FAK, and Rho/ROCK, which directly contributes to therapy resistance. In particular, YAP/TAZ signaling has been linked to resistance to temozolomide through the upregulation of anti apoptotic and DNA repair genes (38, 67, 68). Moreover, this stiff ECM limits immune cell infiltration and promotes M2-like polarization, promoting the immunosuppressive character of the TME (51, 69).

In conclusion, the ECM in GBM is not a passive structural scaffold but an actively altered and mechanobiologically important component of the TME. Its alteration into a fibrotic, stiff, and immunosuppressive network supports cancer growth and reduces the effectiveness of treatments. Incorporating ECM focused approaches into both experimental models and clinical strategies will be essential for overcoming therapeutic resistance and improving translational outcomes in GBM (43, 51).

The cellular composition of the GBM microenvironment is defined by pronounced heterogeneity and a highly dynamic interaction between tumor cells and their surrounding stroma. Rather than representing a homogenous tumor mass, GBM presents a dynamic microenvironment composed of diverse tumor cell subpopulations and a variety of nonmalignant cells (Figure 3).

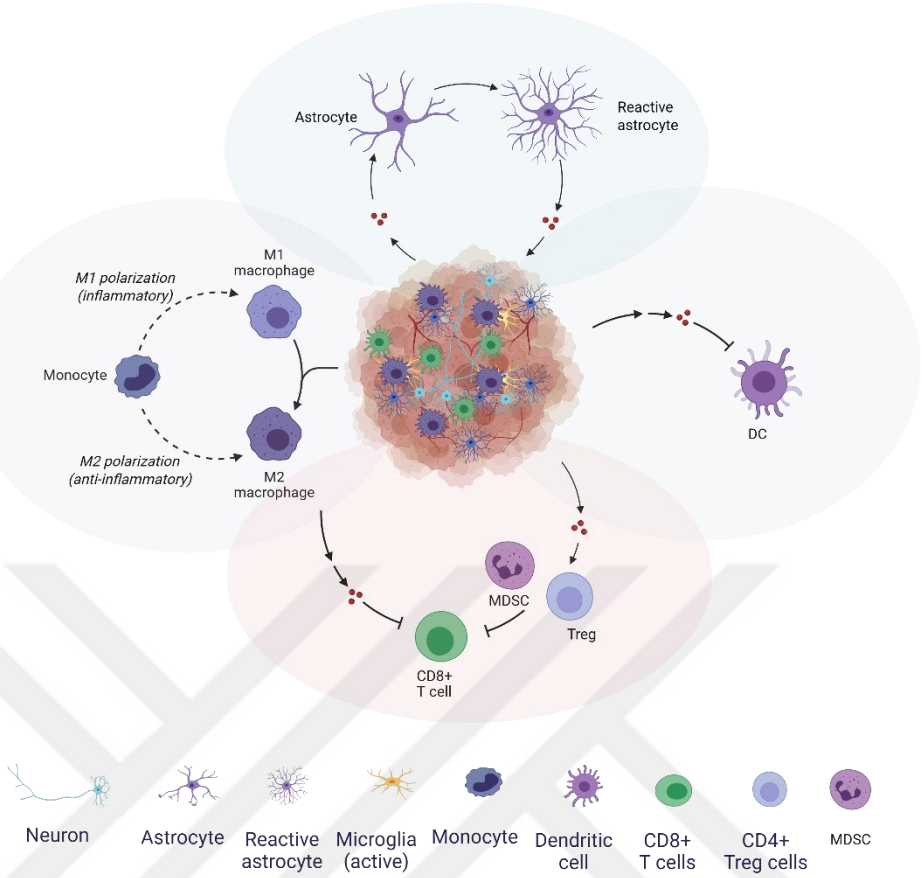

Figure 3 Schematic overview of GBM cellular microenvironment**.** The immunosuppressive and protumorigenic interactions between glioma cells and stromal components including tumor associated microglia and macrophages (TAMs), reactive astrocytes, cancer associated fibroblasts (CAFs), myeloid derived suppressor cells (MDSCs), tolerogenic dendritic cells (DCs), and $CD8^+$ T cells. (Adapted from Biorender).

Glioblastoma stem cells (GSCs), as a key cellular component of the TME, possess self renewal capacity, multilineage differentiation potential, and high resistance to standard treatments (70). GSCs preferentially localize in perivascular and hypoxic niches, where they are maintained by endocrine cues such as VEGF, nitric oxide, and Notch ligands. The phenotypic plasticity of GBM allows them to dedifferentiate into GSC-like states even after differentiation. Their plasticity is promoted by hypoxia inducible factors (HIFs) and cytokine signaling from adjacent stromal cells (32, 71, 72). Transcriptionally, these cells can shift between neural progenitor-like, astrocyte-like, mesenchymal-like, and oligodendrocyte precursor-like states in response to external stimuli, contributing to therapeutic resilience (73).

GBM exists within a profoundly immunosuppressive microenvironment, both due to the inherent immunological properties of the CNS and also due to tumor-specific mechanisms. The landscape of the immune cells within the TME is primarily composed of tumor-associated microglia and macrophages (TAMs), myeloid-derived suppressor cells (MDSCs), and regulatory T cells (Tregs) (74). However, GBM fails to generate an effective anti-tumor immunity; instead, it creates immune-excluded niches with attributes of malfunctioning T cells, the reprogramming of myeloid cells, and immunoregulatory interaction with stromal components (38, 75).

Microglia, the primary immune cells in the CNS, are central to GBM progression (76). The tumor-associated microglia and macrophages (TAMs), derived from both resident microglia and recruited monocytes, account for around 50% of the tumor mass and greatly promote its immunosuppressive environment. These cells exhibit phenotypic plasticity, allowing them to polarize into two main states: the M1 state, marked by its anti-tumorigenic potential and the expression of pro-inflammatory cytokines, such as, interleukin-12 (IL-12), interleukin-6 (IL-6), and tumor necrosis factor-alpha (TNF-α); and the M2 state, which is pro-tumorigenic and secretes immunosuppressive factors, such as, interleukin-10 (IL-10), transforming growth factor-beta (TGF-β), and matrix metalloproteinases (MMPs) (77, 78). This plasticity is also regulated through hypoxic environments and metabolic remodeling, through the shift to aerobic glycolysis. These adaptations support the survival of microglia and the secretion of cytokines under hypoxic conditions, hence driving tumor progression (76, 78). Besides, microglia are central to the maintenance of the GSC niche, fundamental to tumor initiation, progression, and drug resistance (79).

$CD8^+$ T cell exhaustion is a key feature of the suppressed immune response in GBM and is caused by the increased expression of inhibitory receptors. This immunosuppressive state is further promoted by the TME with cytokines, and the presence of Tregs and MDSCs, which inhibit dendritic cell activation and disrupt the function of effector $CD8^+$ T cells (38, 80-85).

Endothelial cells are critical for the aggressive progression of GBM, contributing to the development of an abnormal and highly disorganized vascular network (Figure 4). These cells are stimulated by tumor secreted proangiogenic factors such as VEGF and FGF2, which promote angiogenesis to sustain oxygen and nutrient supply to the tumor (86). However, the resulting vasculature is structurally and functionally disorganized, leading to hypoxic zones that support GSC niches (87).

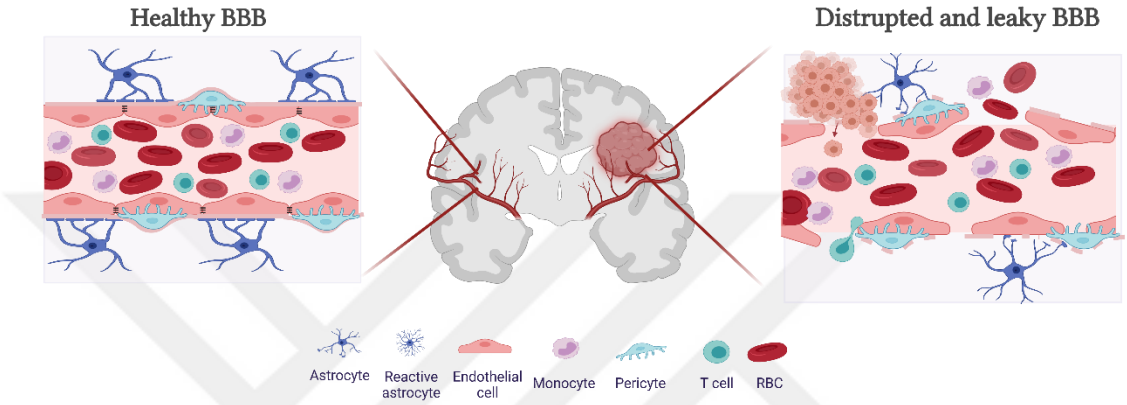

Figure 4 Schematic overview of glioblastoma blood-brain barrier (BBB). BBB is shown with compact endothelial cells connected by tight junctions and a dense basement membrane. In contrast, the GBM-associated BBB (right) is disrupted, featuring leaky endothelial cells, widened tight junctions, and loss of contact with astrocytic endfeet. (Adapted from Biorender).

Astrocytes also play an important role in glioblastoma progression. They are reprogrammed into reactive astrocytes to produce IL-1β, CXCL1, and VEGF, leading to blood brain barrier (BBB) compromise and matrix remodeling via MMP secretion (88-90). These astrocytes further promote tumor survival by transmitting anti apoptotic factors and drug resistance signals through gap junctions and extracellular vesicles (32).

Hypoxia is a defining characteristic of the GBM TME and plays a central role in intratumoral heterogeneity and therapeutic resistance (91, 92). Spatial gradients in oxygen availability within the tumor lead to the formation of distinct regions, including necrotic cores and hypercellular compartments (Figure 5) (42, 93). The necrotic core is marked by severely hypoxic zones caused by impaired blood flow, leading to extensive cell death and the release of proinflammatory mediators that support tumor

growth and invasiveness (94, 95). Hypoxic areas within the necrotic core harbor therapy resistant cancer stem cells and other highly aggressive subpopulations, further driving tumor progression (96, 97). GBM cells tend to accumulate around the periphery of necrotic regions, forming pseudopalisading structures indicative of cellular migration in response to hypoxic and nutrient-deprived conditions. Hypercellular areas, while relatively less hypoxic, still maintain a low-oxygen environment that promotes malignant phenotypes and contributes to therapeutic resistance (40, 95, 97, 98).

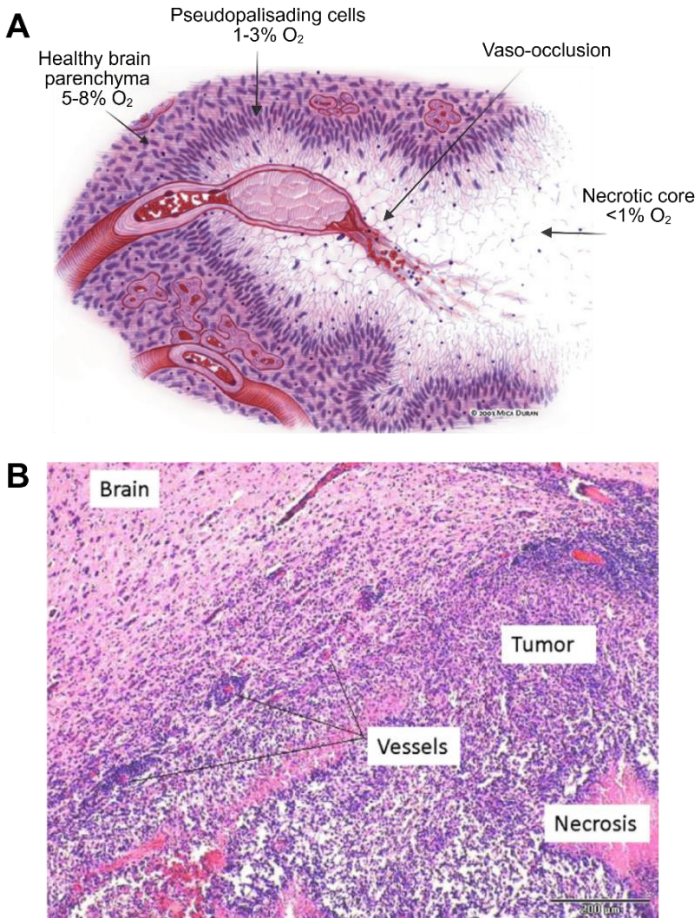

Figure 5 Histopatology of GBM. (A) Schematic representation of pseudopalisade formation in GBM (42). (B) Representative hematoxylin and eosin staining of GBM pathology (93). Adapted with permission.

The hypoxic microenvironment is closely linked to the activation of hypoxia inducible factors (HIFs), particularly HIF-1α, initiates transcriptional changes that facilitate tumor cell adaptation and survival under oxygen deprived conditions (99, 100). Among these changes, HIF-1α regulates the transcriptional activation of genes associated with angiogenesis, including vascular endothelial growth factor (VEGF), a key driver of neovascularization (95, 97). HIF-1α also regulates the expression of several microRNAs, which plays a significant role in promoting proliferation, migration, and resistance to apoptosis (101-103).

2.3 Current GBM Models and Limitations

Despite years of research and technological advances, the prognosis for GBM has not improved significantly. Glioblastoma remains incurable and is recognized as the most devastating tumor in the central nervous system (104, 105). In order to bring a new drug to market, the current pipeline takes about 15 years and costs $2.6 billion (106). Preclinical evaluation of drug candidates generally involves initial efficacy testing in 2D cell culture platforms, then in animal models prior to clinical translation. Current GBM model systems are incapable of mimicking some of the complex aspects of the disease (107). Spatial organization of *in vivo* tissues cannot be replicated by 2D cell cultures, and when cells are cultivated on a plastic petri dish, they contact a stiff surface (approximately 10^5 kPa for a petri dish versus 2-10^2 kPa for general soft tissues), which affects the cell behavior especially gene expression and drug sensitivity (108, 109). Furthermore, they fail to mimic the complex TME, including dynamic interactions between cells and their surrounding matrix, temporally and spatially regulated signaling pathways, oxygen gradients, and physical constraints. As a result, cells rapidly lose intrinsic traits and functions (110, 111). The implantation of patient-derived glioblastoma stem cell-like cultures into mice and organotypic brain slices are two fundamental preclinical models that have been used to assess the efficacy of new treatments for glioblastoma (112, 113). Organotypic cultures provide abundant ECM signals but offer limited control over experimental variables, making functional research challenging (114). Although patient-derived xenograft models accurately reproduce the characteristics of the native tumors, their clinical utility for point-of-care

testing is limited by the long time required to establish (40-50 days), low success rates, high costs, and ethical concerns (115). Moreover, investigating the behavior of human cancer cells in animal models often necessitates the use of immunocompromised animals, thereby excluding the contribution of immune components to tumor progression. These limitations in current platforms for studying GBM biology highlight the need for alternative *in vitro* platforms that enable the analysis of tumor-microenvironment interactions under physiologically relevant and experimentally controllable conditions (114).

Since glioblastoma microenvironment has a significant influence on tumor progression, advanced GBM microenvironment models provide a valid option as experimental GBM models with the advantage of overcome the limitations associated with conventional models (41). Several 3D glioblastoma models have been developed during previous decade. Early 3D *in vitro* models, mainly spheroid cultures embedded in hydrogels, provided important results about the mechanical and microenvironmental regulation of GBM, but they were limited in their ability to mimic the full extent of cellular heterogeneity and native tissue organization (116, 117). In order to overcome these limitations, the field has increasingly moved toward organoid-based platforms, which utilize self-organizing, patient-derived cells in 3D cultures to mimic the cellular heterogeneity and structural complexity of GBM within a more physiologically relevant and integrated tissue context (118-120). Although organoid-based GBM models closely mimic tumor biology, their limited control over structure, mechanics, and consistency makes them less suitable for reproducible and high-throughput testing. In contrast, 3D bioprinting technologies have emerged as powerful tools to reconstruct the glioblastoma microenvironment with precision, enabling the spatial design of tumor and stromal compartments, incorporation of stiffness gradients, and diverse cell types, including immune and vascular elements (71, 121-123). The organ-on-chip technology is also increasingly applied *in vitro* to simulate the complex features of the GBM microenvironment. Such platforms can be employed to model tissue rigidity, vascular interfaces, and immune interactions within compartmentalized 3D models under controlled conditions (11, 124-126). In addition, these models have been successfully integrated with microfluidic systems, offering the ability to precisely

control fluid flow, chemical gradients, and shear stress. These platforms are highly effective at modeling the dynamic features of the TME, including interactions with blood vessels, drug transport, and the physical forces that govern tumor growth and therapeutic outcomes (127-133). Despite substantial progress enabled by advanced *in vitro* models, they remain limited in terms of scalability, reproducibility, and viability over extended periods.

There is an increasing demand for new tumor models that can accurately replicate native tumor biology and elucidate the mechanisms driving malignancy progression. Advanced models can significantly reduce the overall cost of drug discovery through two main mechanisms. First, by reducing the reliance on animal models for preclinical assays, the associated costs can be lowered. Second, their enhanced predictive capacity for drug efficacy and toxicity can decrease the risk of clinical trial failure and subsequent drug withdrawal, thereby preventing financial losses for pharmaceutical companies. In this context, 3D bioengineered tumor models serve as a critical intermediary between conventional preclinical assays and human clinical trials, offering increased translational value for drug response assessment.

This study aimed to develop a physiologically relevant GBM TME model by using dECM based hydrogels and a hypoxia chip to mimic the native TME in terms of biochemical, mechanical, and hypoxic conditions. Decellularization of bovine brain tissue was carried out using two different protocols, and the resulting dECMs were characterized by DNA content, protein, and glycosaminoglycan retention. The dECMs were solubilized and combined with hyaluronic acid methacrylate (HAMA) to fabricate photocrosslinkable composite hydrogels (HAMA/dECM), which were optimized for printability, mechanical strength, and degradation profiles. U87 glioblastoma and HMC3 microglia cells were loaded into the hydrogel solution, and the obtained bioink was bioprinted in a circular structure (glioblastoma cells at the center and microglia cells at the periphery). The printed structure was placed into a PDMS chip, which was covered with a gas diffusion barrier to induce central hypoxia. Cell behavior in the chip was studied using Live/Dead and Alamar Blue assays, and their cytoskeleton organization, proliferation (Ki67), and differentiation (GFAP) were

assessed by immunofluorescence staining. Central hypoxia was confirmed by Image-iT Green staining, necrotic and hypercellular pseudopalisading regions were identified with ethidium homodimer-1 and Ki67 staining. Functional studies were carried out, including invasion assays, a fluorescein-based drug diffusion model, and cytotoxicity assays using temozolomide (TMZ) to calculate IC_{50} values. Real-time PCR was used to study the expression profiles of hypoxia- and tumor-related genes, and quantitative proteomic analysis was performed to investigate cellular adaptation to hypoxia. Overall, this platform mimics the certain pathological characteristics of GBM, including pseudopalisading necrosis, ECM interactions, and therapeutic response, offering promise as a reliable *in vitro* GBM model for research and drug screening.

3 MATERIALS AND METHODS

3.1 Materials

2-Hydroxy-4′-(2-hydroxyethoxy)-2-methylpropiophenone (#410896), Hyaluronic acid sodium salt from Streptococcus equi (#53747), Pepsin from porcine gastric mucosa (#P7012-250MG), Triton X-100 (#T8787) were obtained from Sigma Aldrich (USA). Methacrylic anhydride (#276685), N,N-dimethylformamide (#103053) was obtained from Merck Millipore (Germany). Opti-MEM Reduced Serum Medium (#31985062), Normal Goat Serum (#PCN5000), Fibronectin (#33016015), phosphate buffered saline (PBS) without Ca+2 and Mg+2 (#14190-094), penicillin/streptomycin (#15140-122), DMEM without phenol red (#11054020) were purchased from Gibco (USA). AlexaFluor 488-phalloidin (#A12379), Pierce™ BCA Protein Assay Kit (#A55864), TRIzol reagent (#15596026), RevertAid First Strand cDNA Synthesis Kit (#K1622) were obtained from ThermoScientific (USA). Fetal bovine serum (FBS) (#04-007-1A) and bovine serum albumin (BSA) (#040071A) were purchased from Biological Industries (Israel). PBS with Ca+2, Mg+2 (#PBS-2A) was obtained from Capricorn (Germany). Fluorescein-sodium (0.4 kDa, #J61549) was purchased from Alfa Aesar (Germany). DNase (DENARASE, 5 MU, GMP) was obtained from c-LEcta (Germany). DNeasy Blood & Tissue Kit was purchased from Qiagen (Germany). Tissue-Tek OCT (#4583) was obtained from Sakura Finetek (Japan). Image IT green hypoxia reagent (#I14834), AlamarBlue Cell Viability Reagent (#DAL1025), LIVE/DEAD™ Viability/Cytotoxicity Kit (#L3224), Lipofectamine 2000 Transfection Reagent (#11668019), Chicken anti-human GFAP IgY (#PA1-10004), Goat anti-Chicken IgY (H+L) Secondary Antibody, Alexa Fluor™ 488 (#A-11039), Goat anti-Rabbit IgG (H+L) Cross-Adsorbed Secondary Antibody, Alexa Fluor™ 555 (#A-21428) were purchased from Invitrogen (USA). Rabbit anti-human anti-Ki67 IgG primary antibody (#ab15580) were purchased from Abcam (UK). pcDNA3-EGFP plasmid (#13031) was obtained from Addgene (USA). Direct-zol RNA miniprep (#R2051) was purchased from Zymo Research (USA). SYLGARD™ 184 Silicone Elastomer Kit (#4019862) was obtained from Dow Chemical Company (USA). PowerUp™ SYBR™ Green Master Mix (#A25741) was

purchased from Applied Biosystems (USA). G418 solution (#4727878001) was obtained from Roche (Switzerland). Ultra low attachment microplates (#10023683) were purchased from Corning (USA). Primers (Table 1) were obtained from Sentromer DNA Teknolojileri (Türkiye).

Table 1 Primer list

Gene	**Forward and Reverse Sequence**
Glial Fibrillary Acidic Protein (GFAP)	Forward: 5′-CTGGAGAGGAAGATTGAGTCGC-3′ Reverse: 5′-ACGTCAAGCTCCACATGGACCT-3′
Hypoxia-Inducible Factor 1-Alpha (HIF1A)	Forward: 5′-TATGAGCCAGAAGAACTTTTAGGC-3′ Reverse: 5′-CACCTCTTTTGGCAAGCATCCTG-3′
SRY-Box Transcription Factor 2 (SOX2)	Forward: 5′-GCTACAGCATGATGCAGGACCA-3 Reverse: 5′-TCTGCGAGCTGGTCATGGAGTT-3
Chitinase-3-Like Protein 1 (CHI3L1)	Forward: 5′-CCACAGTCCATAGAATCCTCGG-3 Reverse: 5′-TGCCTGTCCTTCAGGTACTGCA-3
Matrix Metallopeptidase 2 (MMP2)	Forward: 5′-AGCGAGTGGATGCCGCCTTTAA -3 Reverse: 5′-CATTCCAGGCATCTGCGATGAG -3
Matrix Metallopeptidase 9 (MMP9)	Forward: 5′-GCCACTACTGTGCCTTTGAGTC-3 Reverse: 5′-CCCTCAGAGAATCGCCAGTACT-3
Nestin (NES)	Forward: 5′-TCAAGATGTCCCTCAGCCTGGA-3 Reverse: 5′-AAGCTGAGGGAAGTCTTGGAGC-3
Transforming Growth Factor Beta (TGF-β)	Forward: 5′-TACCTGAACCCGTGTTGCTCTC -3 Reverse: 5′-GTTGCTGAGGTATCGCCAGGAA-3
Epidermal Growth Factor Receptor (EGFR)	Forward: 5′-AACACCCTGGTCTGGAAGTACG -3 Reverse: 5′-TCGTTGGACAGCCTTCAAGACC -3
Cluster of Differentiation 44 (CD44)	Forward: 5′-CCAGAAGGAACAGTGGTTTGGC-3 Reverse: 5′-ACTGTCCTCTGGGCTTGGTGTT-3
Ki67 Antigen (Ki67)	Forward: 5′-GAAAGAGTGGCAACCTGCCTTC-3 Reverse: 5′-GCACCAAGTTTTACTACATCTGCC-3
Glyceraldehyde-3-Phosphate Dehydrogenase (GAPDH)	Forward: 5′-GTCTCCTCTGACTTCAACAGCG-3 Reverse: 5′-ACCACCCTGTTGCTGTAGCCAA-3

3.2 Methods

3.2.1 Preparation of composite hydrogels

3.2.1.1 Production of dECM

Fresh bovine brain tissues were sourced from a local slaughterhouse and washed with phosphate buffered saline (PBS, 10 mM, pH 7.4) containing 1% penicillin/streptomycin (100,000 U/mL penicillin and 100,000 μg/mL streptomycin) at 4°C for 2 h, then dissected into small pieces (0.5 x 0.5 x 0.5 cm^3).

Decellularization protocol 1 (dECM1): Freeze/thaw cycles, Triton X-100, and DNase treatment

The minced bovine brain tissues were placed into plastic bottles, and 1X PBS (containing 1% pen/strep) was added. They were frozen at -80 °C overnight, thawed at room temperature (RT), and sieved (using 200 mesh). The tissues were washed with fresh 1X PBS for 10 min at RT and sieved again. The freeze/thaw cycle was performed 3 times. The material was immersed in autoclaved dH_2O containing 1% pen/strep, stirred on a magnetic stirrer (60 rpm, 24 h), and then introduced to Triton X-100 solution (1%, v/v, in 10 mM Tris HCl, 1 mM EDTA, pH 7.4), and stirred (60 rpm, 48 h) with daily solution change. The tissues were washed with dH_2O for 5 h with 5 solution changes and then immersed into DNase solution (40 U/mL in 10 mM Tris-HCl, 10 mM $MgCl_2$, 0.5 mM $CaCl_2$, pH 7.5), and stirred (37 °C, 24 h). The decellularized brain tissues were transferred into falcon tubes and washed with dH_20 for 10 times.

Decellularization protocol 2 (dECM2): SDS and DNase treatment

The minced bovine brain tissues were placed into beakers with sodium dodecylsulfate solution (SDS, 0.1%, w/v, in 1X PBS) containing 1% pen/strep, and stirred on a magnetic stirrer (60 rpm, 5 days). The solutions were sieved and fresh SDS were added daily. The tissues were washed with dH_2O for 5 h with 5 solution changes, then immersed in DNase solution (40 U/mL in 10 mM Tris-HCl, 10 mM $MgCl_2$, 0.5

mM $CaCl_2$, pH 7.5), and stirred (24 h, 37 °C). The decellularized brain tissues were transferred into falcon tubes and washed with dH_20 for 10 times.

3.2.1.2 Characterization of the dECMs

Decellularization efficiency of the dECMs (dECM1 and dECM2) was determined by staining with 4',6-diamidino-2-phenylindole (DAPI) and Hematoxylin Eosin (H&E) to assess the removal of the cellular components. Additionally, DNA was isolated from the dECMs, and efficiency was determined quantitatively in terms of dsDNA removal.

3.2.1.2.1 Determination of dsDNA removal in decellularized samples

In order to determine the effectiveness of decellularization protocols in removing dsDNA, genomic DNA was extracted from tissue samples using the DNeasy Blood & Tissue Kit (Qiagen) according to the manufacturer's protocol. Firstly, tissue samples (25 mg) were homogenized by grinding the sample in liquid nitrogen and incubated overnight at 56°C in a solution containing 20 µL of Proteinase K and 180 µL of ATL buffer to achieve complete tissue lysis. 200 µL Buffer AL and 200 µl ethanol (96-100%) were added to the lysate, vortexed for 15 s, and the mixture was transferred to the DNeasy Mini spin column. DNA binding was achieved via centrifugation at 800 rpm for 1 min, followed by sequential washes with 500 µL of AW1 and AW2 buffers. A final high speed centrifugation at 14,000 rpm for 3 min was performed to dry the membrane. DNA was eluted by applying 200 µL of AE buffer directly to the membrane, incubating at RT for 1 min, and centrifuging at 8000 rpm for 1 min. DNA concentrations were quantified spectrophotometrically at 280 nm using a Nanodrop One instrument (Thermo Scientific).

3.2.1.2.2 Microscopic analysis of cell removal

Small pieces of native and dECM samples were rinsed 3 times with PBS (5 min each), followed by incubation in sucrose solution (30%, w/v in dH_2O) at 4°C for 24 h to prevent ice crystal formation. Tissues were fixed by immersion in 10% neutral buffered formalin at 4°C for 24 h, then washed 3 times with PBS (5 min each). The

fixed samples were embedded in Optimal Cutting Temperature (OCT) compounds in molds of appropriate size and rapidly frozen by exposure to liquid nitrogen vapor. The OCT embedded and frozen tissues were subsequently cryosectioned (5 μm) using a cryomicrotome (Leica Cryomicrotome CM1520) and mounted onto positively charged glass microscope slides.

In order to determine the effectiveness of the decellularization process in terms of removing cellular components, these sections were subjected to H&E and DAPI staining. DAPI, a fluorescent dye that preferentially binds to adenine thymine (AT) rich regions of DNA, was used (134). The slides were rinsed 3 times with PBS (5 min each), and incubated with DAPI solution (0.5 μg/mL) at RT for 15 min. Following staining, slides were washed 3 times with PBS (5 min each) and subsequently with dH_2O. The samples were covered with a mounting medium (Entellan) and dried overnight at RT. Image acquisition was carried out using a fluorescence microscope (Zeiss Axio Imager M2). Image analysis and quantification of stained nuclei were conducted using ImageJ software. The number of nuclei in the dECM samples was compared to native brain tissue. The decellularization efficiency was calculated by determining the percent reduction in nuclear presence, expressed as:

$$\text{Efficiency (\%)} = \frac{\text{Native-dECM}}{\text{Native}} \text{ x } 100$$

H&E staining was performed to examine cellular and extracellular components, including nuclei, cytoplasm, and matrix structures. Hematoxylin, a cationic dye, preferentially interacts with nucleic acids, resulting in a blue to purple staining of nuclear structures. In contrast, eosin is a non specific acidic dye that stains cytoplasmic and extracellular proteins pink (135). The slides were fixed with 10% neutral buffered formalin at 4°C for 15 min, followed by sequential washing with PBS twice, tap water for 1 min and stained with Mayer's Hematoxylin for 1 min. Residual hematoxylin was removed by rinsing the stained slides under running tap water and dH_2O for 1 min. For counterstaining, slides were immersed in Eosin Y solution for 30 s. Subsequently, the samples underwent sequential dehydration in 95% and 100% EtOH (2 times, 1 min

each). For tissue clearing, samples were treated twice with xylene (1 min). Finally, the slides were mounted using Entellan medium and left to air dry overnight at RT. Image acquisition was carried out using a brightfield light microscope (Zeiss Axio Imager M2).

3.2.1.2.3 Fourier transform infrared spectroscopy analysis of dECMs

The presence of protein and lipids in dECMs was determined using a Fourier transform infrared (FTIR) spectroscopy (Shimadzu, IR Tracer 100). Spectral measurements were performed in the 400-4000 cm^{-1} range to detect characteristic functional groups. Amide bands at specific spectral regions, including amide I (1630 cm^{-1}), amide II (1530 cm^{-1}), amide III (1230 cm^{-1}), and amide A (3300 cm^{-1}) were checked (136). Lipid presences were checked through CH_2 and CH_3 stretching vibrations between 2800-3000 cm^{-1}, along with ester carbonyl (C=O) stretching at 1740 cm^{-1} (137).

3.2.1.3 Preparation of soluble dECM

dECMs obtained using both protocols were frozen at -80°C, lyophilized, and then grounded into fine powders through cryomilling (20 Hz, 2 min, 2 cycles). In order to prepare soluble dECMs, the powdered dECM (10 mg/mL) was enzymatically digested in pepsin solution (1 mg/mL in 0.1 M HCl) (Figure 6). The digestion process was carried out on magnetic stirrer at 300 rpm for 48 h at RT. The digested mixture was centrifuged at 13,000 rpm for 10 min at 4°C, and the supernatants containing soluble dECMs were collected. The supernatants were neutralized to physiological pH (7.4) using cold NaOH, then frozen at -80°C overnight and subsequently lyophilized for long term storage (134, 138).

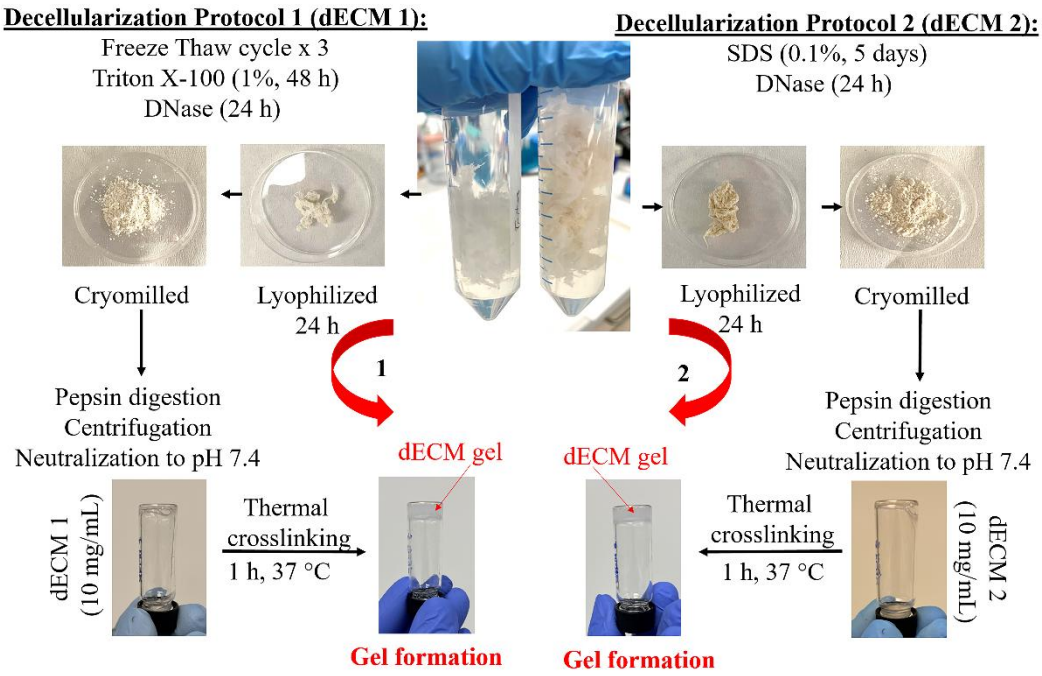

Figure 6 Steps of the decellularization process of brain tissue by different protocols. Protocol 1 (dECM1). Protocol 2 (dECM2).

3.2.1.3.1 Glycosaminoglycan quantification

Quantification of sulfated glycosaminoglycans (GAGs) following decellularization was carried out using 1,9-dimethylmethylene blue (DMMB) assay. The digested dECMs were reconstituted in PBS to a final concentration of 1 mg/mL. The sample solution (100 µL) was mixed with equal volume of 40 µM DMMB reagent. The absorbance was measured immediately at 530 nm using a spectrophotometer (PerkinElmer, 8500FL). A standard curve was generated using chondroitin sulfate concentrations (0-10 µg/mL), and absorbance values obtained from the samples were interpolated using this curve to calculate the corresponding sGAG concentrations.

3.2.1.3.2 Protein quantification

Total protein concentration in the digested dECM samples was determined using the Pierce™ BCA Protein Assay Kit (Thermo Scientific) in accordance with the manufacturer's instructions. The digested dECMs were reconstituted in PBS (1 mg/mL), and 25 µL aliquots of each sample were transferred to a 96 well microplate.

Subsequently, 200 µL of freshly prepared BCA working reagent (Reagent A and B in a 50:1 ratio) was added. The plate was gently agitated and incubated at 37°C for 30 min to allow for the chromogenic reaction between bicinchoninic acid (BCA) and protein-bound Cu^{+} ions, forming a purple complex proportional to protein concentration. Then, Absorbance readings were acquired at 562 nm using a spectrophotometer (PerkinElmer, 8500FL). A calibration curve was generated from serial dilutions of BSA with known concentrations (0-2000 µg/mL). Absorbance values obtained from the samples were interpolated onto this curve to calculate the corresponding protein concentrations. SDS-PAGE analysis was performed to assess the protein profiles of the dECM samples. Protein lysates were loaded onto polyacrylamide gels and subjected to electrophoresis at 150 V for 1 h. Following separation, the gels were stained with Coomassie Brilliant Blue to visualize protein bands, which were subsequently imaged using a Bio-Rad gel documentation system.

3.2.1.3.3 Gelation kinetics of dECMs with turbidimetry

In order to determine the gelation kinetics of dECMs, a turbidity based assay was performed (139). Soluble dECM solutions (100 µL, 10 mg/mL) were transferred into a 96 well plate, and absorbance at 405 nm was monitored at 3 min intervals over a 90 min period at 37°C using a microplate reader. The resulting absorbance values were normalized between 0% (initial timepoint) and 100% (maximum absorbance) using the following formula:

$$A_N = \frac{A_t - A_0}{A_{max} - A_0}$$

where A_N represents the normalized absorbance at a given time point, A_t is the absorbance at that time. A_0 and A_{max} correspond to the initial and peak absorbance values, respectively.

3.2.1.3.4 Single frequency testing of dECM hydrogels

Rheological characterization of the dECM hydrogels was carried out using single frequency measurements on a rotational rheometer to determine their mechanical

behavior (Malvern Kinexus). dECM solutions (10 mg/mL) were loaded onto the rheometer plate and adjusted to 37°C to initiate gelation. Oscillatory measurements were conducted at a constant frequency (1 Hz) and strain (1%) to track gelation kinetics and characterize viscoelastic properties. The elastic (G') and viscous (G") modulus were monitored at regular intervals until the hydrogels reached equilibrium. The gelation point was defined as the time at which G′ surpassed G″, indicating a shift from a predominantly viscous to an elastic behavior.

3.2.1.3.5 Viability of glioblastoma cells in dECM hydrogels

Hydrogel solutions of dECMs were prepared in phenol red free DMEM high glucose medium (1%, w/v). U87 cells were detached from culture flasks and centrifuged (5 min, 1500 rpm). The cell pellets ($2x10^6$ cell/mL) were suspended with hydrogel solutions, then hydrogel formation was thermally induced at 37 °C for 1 h. The cell loaded hydrogels were transferred into the wells of 48 well plate and complete medium (DMEM High glucose containing 10% fetal bovine serum and 1% pen/strep) was added. The cells loaded in the hydrogels were incubated in a CO_2 incubator (5% CO_2, 37 °C). Cell viability on days 1 and 7 was assessed using a Live/Dead Viability assay. Samples were stained with 2 µM calcein AM and 4 µM ethidium homodimer-1 in phenol red free DMEM for 30 min at 37 °C, followed by PBS washing. The stained cells were examined with CSLM for stains of green (live) and red (dead).

3.2.1.4 Synthesis and characterization of hyaluronic acid methacrylate

Hyaluronic acid (1 g) was dissolved in dH_2O (100 mL) at RT (1%, w/v), 66 mL dimethylformamide (DMF) was added (2:3, DMF: H_2O, v:v), and the mixture was incubated at 4 °C for 1 h. Subsequently, 5 mL of methacrylic anhydride (3%, v/v) was added dropwise, while maintaining the pH between 8 and 9 for at least 5 hours. The reaction mixture was then stirred overnight at 4 °C (12). The resulting solution was filtered, transferred into a dialysis membrane (MWCO 10,000 Da) and dialyzed against dH_2O at 4 °C for 72 h. After dialysis, the solution was lyophilized to obtain foam. The degree of methacrylation (DoM) of HAMA was determined using proton nuclear magnetic resonance (^{1}H-NMR) spectroscopy (400 MHz Bruker DPX 400).

The DoM, defined as the number of methacrylate groups per disaccharide unit, was calculated by the ratio of the integral areas of the methacrylate protons (6.1, 5.6, and 1.85 ppm) to that of the methyl protons (1.9 ppm) originating from the HA backbone (140).

3.2.1.5 Preparation of composite hydrogels

In order to mimic the ECM of the glioblastoma microenvironment, a hydrogel was prepared by combining dECM with HAMA to enhance the mechanical properties of the hydrogel (141). Irgacure 2959, a photoinitiator, was dissolved in DMEM (3 mg/mL, 10 mL) at 37°C, followed by cooling to 4 °C. HAMA (0.1 g) was added to this solution and mixed overnight at 4°C. Subsequently, powder dECM (final concentrations of 10, 20, and 30 mg/mL) was added to the HAMA solution (10 mg/mL), and the mixture was stirred at 4 °C for 48 h to obtain a uniform, homogeneous solution. The resulting mixture was UV crosslinked (365 nm, 2 min, 0.160 j/cm^2). In the naming system for formulations, 'H' stands for HAMA and 'D' stands for dECM. The numbers preceding each letter indicate the final concentration of each component in the hydrogel, expressed as percent weight per volume (w/v). For example, '1H3D' indicates a formulation containing 1% (w/v) HAMA and 3% (w/v) dECM.

3.2.1.6 Characterization of composite hydrogels

3.2.1.6.1 FTIR of the hydrogels

The contents of the HAMA/dECM hydrogel were confirmed using FTIR spectroscopy (Shimadzu, IR Tracer 100). Samples were scanned in the 400-4000 cm^{-1} range. The presence of HAMA within the composite hydrogel was confirmed by the characteristic absorption band corresponding to methacrylate ester (C=O) stretching vibrations (1665 cm^{-1}) (142). Additionally, the presence of dECM was verified by the detection of characteristic amide associated absorption bands, including bands at 1600-1800 cm^{-1} (amide I), 1470-1570 cm^{-1} (amide II), 1250-1350 cm^{-1} (amide III), and 3300-3500 cm^{-1} (amide A), which are indicative of peptide bonds (136).

3.2.1.6.2 Determination of equilibrium water content

Swelling behavior of the HAMA/dECM hydrogels was assessed by determining equilibrium water content. Initially, the hydrogels were freeze dried and their dry weights recorded. Subsequently, samples were incubated in PBS at 37 °C until they reached swelling equilibrium. After incubation, the swollen hydrogels were blotted to remove excess surface liquid and weighed again. The equilibrium water content (EWC) and degree of swelling (DS) were calculated using the following equations:

$$EWC\ (\%) = \frac{W_w - W_d}{W_w} \times 100 \qquad (I)$$

$$DS\ (\%) = \frac{W_w - W_d}{W_d} \times 100 \qquad (II)$$

where W_w represents the weight of the swollen hydrogel and W_d corresponds to its dry weight.

3.2.1.6.3 Scanning electron microscopy of the hydrogels

The microstructure of the dried hydrogels was characterized using scanning electron microscopy (SEM). Samples were first lyophilized by freeze drying under vacuum at -80 °C. After, the hydrogels were sputter coated with a thin layer of gold (20 Å for 120 s) under vacuum conditions to enhance conductivity. Imaging was performed using a SEM (Zeiss EVO 10). Quantitative analysis of pore size was conducted using ImageJ software.

3.2.1.6.4 *In situ* degradation of the hydrogels

In order to examine the degradation behavior, the hydrogel samples were initially washed with dH_2O and freeze dried to obtain their initial dry weights. They were then incubated in PBS at 37 °C for a period of 14 days. At predetermined time points (days 1, 2, 3, 7, and 14), the samples were washed with dH_2O, lyophilized, and reweighed. The extent of weight loss was calculated gravimetrically using the following equation:

$$\text{Remaining weight (\%)} = \frac{W_0}{W_t} \times 100$$

where W_0 is the initial dry weight, W_t is the dry weight at time t

3.2.1.6.5 Compression testing of the hydrogels

The mechanical properties of the hydrogels were characterized under compression. Cylindrical hydrogel samples (10 mm diameter, 5 mm height) were incubated in PBS for 24 h at 37 °C to reach swelling equilibrium. Compression testing was conducted using a mechanical testing equipment (Shimadzu AGS-X, Japan) with a crosshead speed of 0.5 mm/min. Stress-strain curves were generated, and the compressive modulus was calculated from the linear region of the initial slope.

3.2.1.6.6 Strain sweep testing of the hydrogels

A strain sweep test was conducted to evaluate the viscoelastic behavior of the hydrogels at a fixed oscillatory frequency of 1.0 Hz (143). The test began at low strain values and gradually increased to identify the point where material structure started to break down, indicated by a deviation from linear viscoelastic behavior. Measurements were recorded across a strain range of 0.01 to 100%, and both elastic (G′) and viscous (G″) modulus were analyzed as functions of strain using a rotational rheometer (Kinetux, Malvern, UK) equipped with a parallel plate geometry.

3.2.1.6.7 Printability analysis using viscosity and thixotropy of hydrogel solutions

Irgacure 2959, a photoinitiator, was dissolved in DMEM (3 mg/mL, 10 mL) at 37°C, followed by cooling to 4 °C. HAMA (0.1 g) was added to this solution and mixed overnight at 4°C. Subsequently, powder dECM (final concentrations of 10, 20, and 30 mg/mL) was then added to the HAMA solution (10 mg/mL), and the mixture was stirred at 4 °C for 48 h to obtain a uniform, homogeneous solution. Flow behavior and thixotropic characteristics of the hydrogel solutions were determined at 10°C using a rotational rheometer (Kinetux, Malvern, United Kingdom) equipped with a cone

plate geometry. In order to study shear thinning behavior, a flow curve was obtained by applying shear rates in a logarithmic sequence ranging from 0.1 to 100 s^{-1} and determining viscosity as a function of shear rate. For thixotropic analysis, a three step shear protocol was used. Initially, a low shear rate of 1 s^{-1} was applied for 30 s to measure the viscosity at rest. This was followed by a high shear rate of 100 s^{-1} for 30 s to simulate extrusion conditions, and finally the shear rate was reduced back to 1 s^{-1} for 60 s to study viscosity recovery.

In order to evaluate the practical printability of the hydrogel solutions, a printing test was performed. The hydrogel solutions were transferred into a syringe with a 25 gauge nozzle and loaded into the cartridge of a printer (EnvisionTec 3D Bioplotter). The inks were printed with different internal patterns (honeycomb and grid) with four layers to determine the printability of the hydrogel solutions. The printing parameters are presented in Table 2. Following printing process, the constructs were crosslinked under UV light (365 nm).

Table 2 Printing parameters for the HAMA/dECM model

Nozzle diameter	Layer height	Print speed	Pressure	Temperature	Crosslinking
25 gauge	0.25 mm	6-10 mm/s	0.2-0.4 bar	10°C	UV (365 nm)

3.2.2 *In vitro* studies

3.2.2.1 U87 glioblastoma and HMC3 microglia cell culture

The U87 and HMC3 cell lines were used as glioblastoma and microglia cell sources, respectively. The cells were cultured in T75 flasks with high glucose Dulbecco's Modified Eagle's Medium (DMEM) supplemented with 10% fetal bovine serum (FBS) and penicillin/streptomycin (100 units/mL and 100 µg/mL, respectively). Cultures were maintained in a humidified incubator (37°C, 5% CO_2), with the medium replaced every 2 days. Upon reaching approximately 80% confluency, cells were washed with PBS (10 mM, pH 7.4), treated with trypsin-EDTA at 37°C for 5 min to enable cell detachment, and centrifuged (5 min, 1500 rpm). The resulting pellets were

resuspended in culture medium or hydrogel solution for subsequent experiments. For 2D co-culture experiments, U87 and HMC3 cells were seeded at a 7:3 ratio, reflecting the approximate microglial proportion within glioblastoma tumors.

3.2.2.2 Cytoskeleton and nuclei staining of U87 and HMC3 cells to assess cell matrix interaction

Phalloidin and DAPI stainings were used to study the cytoskeleton and nuclei of glioblastoma and microglia cells in the hydrogels (1H, 3D, and 1H3D) to assess cell-matrix interaction. Cells were detached via trypsinization, centrifuged, and the resulting pellet was resuspended in the hydrogel solutions ($5x10^6$ cells/mL). Following 7 days of incubation, the cells were fixed with paraformaldehyde (4%, w/v) for 15 min at RT. Permeabilization was achieved by treating the samples with Triton X-100 (1%, v/v, in PBS) for 5 min. Samples were then incubated with BSA (1%, w/v, in PBS) at 37 °C for 30 min to block nonspecific binding sites. Actin cytoskeletons were visualized by staining with Alexa Fluor 488-conjugated phalloidin (1:200, v/v) for 1 h, followed by DAPI staining for 10 min to label cell nuclei. After thorough washing with PBS, samples were imaged using a confocal laser scanning microscope (CLSM; Zeiss LSM 900).

3.2.2.3 Transfection of U87 cells with EGFP gene for live cell imaging

In order to facilitate live cell imaging of glioblastoma cells in the co-culture model, U87 cells were transfected to express Enhanced Green Fluorescent Protein (EGFP) gene using the pcDNA3-EGFP plasmid. Cells were first seeded into 24 well plates in complete medium. After 18 h, a DNA-lipid complex was formed by separately diluting 0.5 µg of plasmid DNA and 2 µL of Lipofectamine 2000 in 50 µL of serum free Opti-MEM, mixing the solutions, and incubating for 20 min. Subsequently, the complex (100 µL) was added to the cells, and the final volume was adjusted to 1 mL with Opti-MEM. The cells were then incubated for 48 h to allow for gene expression. Transfected U87 cells (U87-EGFP) were selected over 21 days with G418 (neomycin) and monitored for EGFP expression through fluorescence microscopy and flow cytometry.

3.2.2.4 Invasion assay under mono and co-culture conditions

For the invasion assay, spheroids composed of U87-EGFP cells alone or in co-culture with HMC3 microglia were generated. Firstly, the cells were seeded into ultra low attachment plates ($5x10^3$ U87 cells/100 µL in monoculture, $3.5x10^3$ U87 cells/100 µL and $1.5x10^3$ HMC3 cells/100 µL in coculture) and incubated for 72 h to form compact spheroids. Then, they were transferred into hydrogel droplets prepared on sterile culture dishes using gentle pipetting to ensure structural integrity. Subsequently, the hydrogel constructs were crosslinked under UV light (for HAMA and composite hydrogels) or incubated at 37 °C for 1 h (for dECM hydrogels) to induce gelation, resulting in complete encapsulation within the hydrogel matrix. Then, spheroid containing hydrogels were maintained in a humidified incubator for 48 h. Imaging was carried out at 0, 24, and 48 h using CLSM. The invasion capacity of U87-EGFP cells was assesed by measuring their migration distance from the spheroid boundary into the hydrogel, indicating their ability to infiltrate the surrounding matrix.

3.2.2.5 3D bioprinting of glioblastoma and microglia cells

HAMA/dECM solution (1H3D) was prepared as described in Section 3.2.1.5, and kept on ice. Cells were harvested from tissue culture flasks, and the resulting pellet was resuspended in the 1H3D solution. This bioink solution was loaded into the syringe of EnvisionTEC printer, equipped with a 25 gauge nozzle. Two bioink solutions were prepared by mixing the cell pellet with 1H3D solution: Bioink 1 contained U87 cells (10^7 cells/mL), Bioink 2 contained HMC3 cells (10^7 cells/mL). Then, samples were printed with parameters as shown in Table 3. First, Bioink 1 was printed as the inner region as 4 layers, then bioink 2 solution was printed as borders around the printed Bioink 1.

Table 3 Printing parameters

Cartridge movement speed	Printing pressure	Cartridge temperature	Crosslinking	Shape+Dimensions
8 mm/s	0.4 bar	10°C	UV exposure (365 nm)	Cylinder (9 mm diameter, 1 mm height)

3.2.2.6 Viability analysis of bioprinted glioblastoma and microglia cells

Viability of U87 and HMC3 cells within the printed constructs was assessed on days 1, 3, 7, and 14 using both Live/Dead and Alamar Blue assays. The bioinks, consisting of 1H3D matrix containing U87 and HMC3 cells were printed as described in Section 3.2.2.5, and subsequently incubated in a humidified incubator (5% CO_2, 37 °C). For Live/Dead viability assay, cells were incubated with 2 μM calcein AM and 4 μM ethidium homodimer-1 in phenol red free DMEM for 30 min at 37 °C. Following staining, samples were washed with PBS and imaged using CLSM. Cell viability was quantified by analyzing live (green) and dead (red) cells using ImageJ software. For the Alamar Blue assay, the reagent was diluted at a 1:10 ratio in complete medium and added to the cell loaded hydrogels, followed by incubation for 3 h at 37 °C. Then, absorbance was measured, and the percent reduction in Alamar Blue was calculated using the following equation:

$\lambda_1 = 570$ nm $\quad\quad$ $\lambda_2 = 595$ nm

$(\varepsilon_{ox})_{\lambda 2} = 117.216$ $\quad\quad$ $(\varepsilon_{red})_{\lambda 1} = 155.677$

$(\varepsilon_{ox})_{\lambda 1} = 80.586$ $\quad\quad$ $(\varepsilon_{red})_{\lambda 2} = 14.652$

$A_{\lambda 1}$= Test sample $\quad\quad$ $A\lambda 2$= Test sample

$A'_{\lambda 1}$= Negative control (blank)

$A'_{\lambda 2}$= Negative control (blank)

$$\text{Reduced \%} = \frac{((\varepsilon_{ox})_{\lambda 2} \times A_{\lambda 1}) - ((\varepsilon_{ox})_{\lambda 1} \times A_{\lambda 2})}{((\varepsilon_{red})_{\lambda 1} \times A'_{\lambda 1}) - ((\varepsilon_{red})_{\lambda 2} \times A'_{\lambda 1})} \times 100$$

3.2.2.7 Immunofluorescent staining for proliferation marker in mono and co-cultures

Proliferation properties of U87 and HMC3 cells with mono and co-culture conditions were determined using immunofluorescence staining with Ki67 antibody. Following 7 days of incubation in the printed structure, the cells were fixed with paraformaldehyde (4%, w/v) for 15 min, washed with PBS, and incubated in glycerol (100 mM in PBS) for 15 min at RT. Permeabilization was achieved by treating the samples with Triton X-100 (0.1%, v/v, in PBS) for 10 min. Samples were then incubated with normal goat serum (5%, v/v, in PBST) for 1 h to block nonspecific binding sites. Samples were washed with 1% goat serum and incubated overnight at 4 °C with primary antibody **(**Rabbit anti-human anti-Ki67 IgG, 1:1000, v/v, in 1% goat serum). After incubation, samples were washed 3 times with 1% goat serum (5 min each), and incubated for 1 h at 37°C with secondary antibody (AlexaFluor 555-conjugated anti-rabbit IgG secondary antibody, 1:500, v/v, in 1% goat serum) (144). Nuclear staining was performed using DAPI (0.5 μg/mL in PBS) for 10 min. Then, samples were washed with PBS and imaged using CLSM.

3.2.3 Production and characterization of the hypoxia chip

The hypoxia chips used in this study were fabricated from polydimethylsiloxane (PDMS) using a negative mold (Figure 7). The negative molds were produced using stereolithography (Formlabs, USA) with a light sensitive resin. Afterward, the molds were cleaned in isopropanol using ultrasonic treatment for 30 min and then cured under 405 nm LED light at 60 °C for 3 h.

PDMS (Sylgard 184) was prepared by combining the elastomer base with the curing agent in a 10:1 (v/v) ratio. The resulting mixture was cast into negative molds and allowed to polymerize in a vacuum oven at 70 °C for 4 h (145). After curing, the PDMS chips were removed from the molds, immersed in 70% ethanol for 30 min for disinfection, and subsequently sterilized under UV light for 30 min per side.

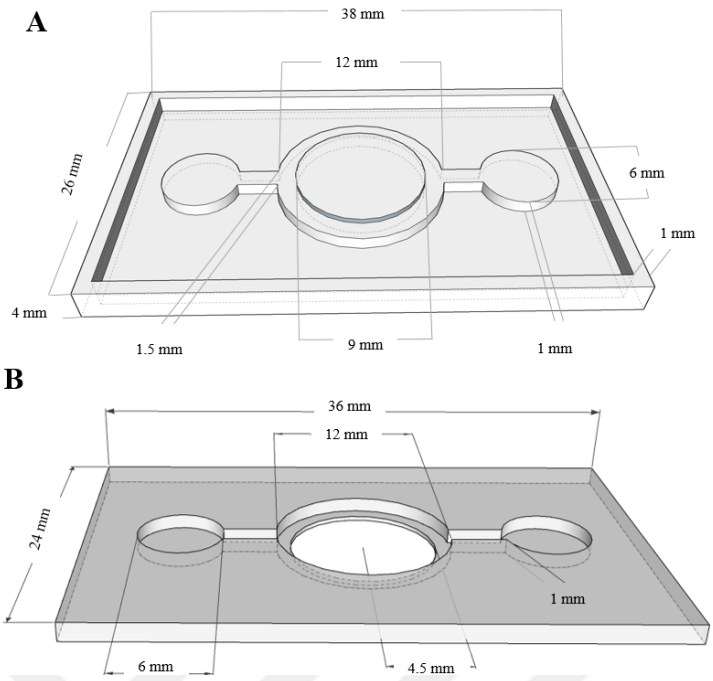

Figure 7 Sketch and dimensions of the (A) negative mold, and (B) PDMS chip.

In this system, PDMS chips were bonded to glass slides by applying a thin layer of uncured PDMS between the chip and the slide, followed by curing at 100 °C for 1 h. The bioprinted, cell loaded hydrogels were placed within the center of the chip. In order to prevent oxygen diffusion from the air and induce hypoxia, a glass slide of the same width was positioned over the hydrogels. The medium was administered from the reservoirs, with flow through the side channels of the chip (Figure 8).

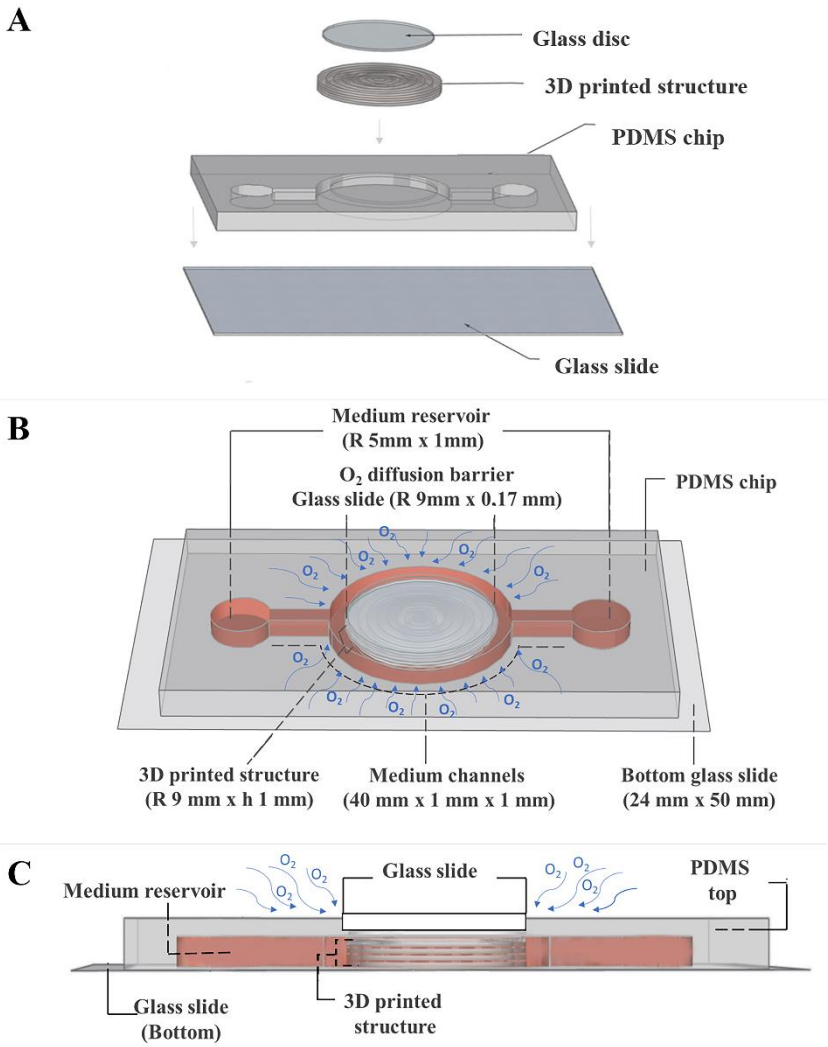

Figure 8 Schematic representation of the hypoxia chip. (A) Components of the *in vitro* hypoxia model, (B) top view, (C) cross-sectional view

3.2.3.1 Fluorescence staining of hypoxic cells

Hypoxic cells were stained using Image-iT Green Hypoxia Reagent (Thermo Scientific), according to the manufacturer's instructions. After 72 h incubation in the hypoxia chip, the medium was replaced with a fresh medium containing 5 µM Image-iT Green Hypoxia Reagent, and the constructs were incubated in a humidified incubator for 3h. Following incubation, the constructs were washed twice with PBS, incubated for an additional 16 h, and imaged using CLSM. Image-iT Green Hypoxia Reagent fluoresces green in hypoxic cells, and its fluorescence intensity increases

proportionally with the degree of hypoxia. The chip without gas diffusion barrier was used as a control.

3.2.3.2 Staining of pseudopalisading and necrotic regions using anti-Ki67 and ethidium homodimer-1

The formation of hypercellular (pseudopalisading) regions in the hypoxia model was shown using anti-Ki67 antibody staining, while necrotic areas were identified using ethidium homodimer-1 (EtHd-1) staining (146). Following 7 days of incubation in the hypoxia chip, the cells were fixed with paraformaldehyde (4%, w/v) for 15 min and washed with PBS. Permeabilization was achieved by treating the samples with Triton X-100 (0.1%, v/v, in PBS) for 10 min. The samples were then incubated with normal goat serum (5%, v/v, in PBST) for 1 h to block nonspecific binding sites. They were washed with 1% goat serum and incubated overnight at 4 °C with primary antibody **(**Rabbit anti-human anti-Ki67 IgG, 1:1000, v/v in 1% goat serum). After incubation, the samples were washed 3 times with 1% goat serum (5 min each), and incubated for 1 h at 37°C with secondary antibody (AlexaFluor 555-conjugated anti-rabbit IgG secondary antibody, 1:500, v/v in 1% goat serum) and AlexaFluor 488-Phalloidin (1:200, v/v) (144). Then, samples were washed with PBS and imaged using CLSM.

In order to identify necrotic areas, the samples were stained with 2 μM calcein AM (living cells, green) and 4 μM ethidium homodimer-1 (necrotic cells, red) in phenol red free DMEM for 30 min at 37 °C. Following staining, samples were washed with PBS and imaged using CLSM.

3.2.3.3 Gene expression analysis using real-time polymerase chain reaction

Gene expression analysis related to GBM was performed using real-time PCR (RT-PCR) (147, 148). Cells were cultured within the hypoxia chip for 7 days prior to RNA extraction. Total RNA was isolated using the Direct-zol RNA Miniprep Kit (Zymo Research), following the manufacturer's protocol. As controls, co-cultured cells grown on 2D monolayers, as well as those loaded in hydrogels under normoxic

conditions, were used. Initially, samples were homogenized in 1 mL of TRIzol reagent using a sonicator (90 s total: 10 s on, 10 s off cycles). Subsequently, 200 µL chloroform was added to each homogenate, followed by 15 min incubation on ice and centrifugation at 16,000 rpm for 15 min at 4 °C to achieve phase separation. The aqueous phase was transferred to a new tube, mixed with an equal volume of absolute ethanol, and loaded onto Zymo-Spin IICR columns for purification. After centrifugation (16,000 rpm, 30 s), columns were washed with 400 µL RNA Wash Buffer. DNase I was applied directly to the column membrane and incubated for 15 min at RT. Further washes were performed using Direct-zol RNA PreWash (twice) and RNA Wash Buffer. RNA was eluted by adding 50 µL of DNase/RNase-free water directly to the column and centrifuging. The concentration and purity of the isolated RNA were determined using a Nanodrop spectrophotometer.

cDNA was synthesized from the isolated RNA using the RevertAid First Strand cDNA Synthesis Kit (Thermo Scientific), following the manufacturer's instructions. The reverse transcription reaction was prepared in a total volume of 20 µL, containing 1 µg of total RNA, 1× reverse transcriptase buffer, 0.5 mM dNTP mix, 50 ng random primers, and 200 U of reverse transcriptase enzyme. The reaction mixture was incubated at 42 °C for 60 min, followed by enzyme inactivation at 70 °C for 5 min. Subsequently, quantitative real time PCR was performed using the PowerUp SYBR Green Master Mix (Applied Biosystems) for amplification and detection. Each PCR reaction was carried out in a total volume of 20 µL, comprising 1× SYBR Green Master Mix, 0.7 µM of each gene specific primer, and 50 ng of cDNA template. The thermal cycling protocol included an initial uracil-DNA glycosylase (UDG) activation step at 50 °C for 2 min, followed by Dual-Lock DNA polymerase activation at 95 °C for 2 min. RT-PCR was performed by 40 amplification cycles, each consisting of denaturation at 95 °C for 15 s and annealing/extension at 60 °C for 1 min. Following amplification, melting curve analysis was conducted between 60-95 °C to verify amplification specificity. GAPDH served as the housekeeping gene for normalization. Relative gene expression was quantified using the comparative cycle threshold (Ct) method ($2^{-\Delta\Delta Ct}$), whereby Ct values of target genes were normalized to GAPDH.

3.2.3.4 Proteomic analysis using liquid chromatography-tandem mass spectrometry

Proteomic profiling was performed using liquid chromatography tandem mass spectrometry (LC-MS/MS), with experimental procedures outsourced to LABMED, Acibadem Healthcare Group (Istanbul, Turkey). Lyophilized tissue samples were first mechanically homogenized using magnetic beads. Protein isolation was achieved using the Universal Protein Extraction Kit (UPX), which includes 4% SDS, 0.1 M dithiothreitol (DTT), and 0.1 M Tris buffer at pH 7.6, along with a protease inhibitor cocktail. Samples underwent thermal denaturation at 95 °C for 5 min, followed by cooling at RT and incubation at 4 °C for 1 h. After centrifugation (10 min, 15,000 × g), the supernatants were collected and stored at -80 °C for downstream processing.

For LC-MS/MS compatibility, proteins were processed via the filter-aided sample preparation (FASP) technique to eliminate interfering substances and improve enzymatic digestion. Specifically, 50 µg of protein from each sample was applied to Microcon 30 filters (30 kDa cut-off, Merck Millipore) and washed with 8 M urea in Tris-HCl (pH 8.5). Proteins were then alkylated in 400 mM iodoacetamide for 20 min under light protected conditions. Remaining reagents were removed by repeated centrifugation and rinsing with urea and 50 mM ammonium bicarbonate. Subsequently, digestion was performed overnight at 37 °C using MS-grade trypsin at a 1:50 enzyme-to-protein ratio. Resulting peptides were eluted via centrifugation, desalted, and subjected to LC-MS/MS analysis. Peptide samples (400 ng) was injected into a nano-liquid chromatography system for separation, and mass analysis was performed using a Xevo G2-XS QTof instrument (Waters). Resulting spectra were processed and matched to protein entries in the UniProt database using Progenesis software. Label-free quantification (LFQ) was employed to assess protein abundance, and proteins showing significant differential expression were further analyzed for functional annotation and pathway enrichment using the Metascape and STRING databases (149).

3.2.3.5 Immunofluorescence staining for differentiation marker under normoxic and hypoxic conditions

In order to determine the astrocytic differentiation properties of U87 cells in both mono- and co-culture, and under normoxic and hypoxic conditions, immunofluorescence staining was conducted using GFAP antibody. Following 7 days of incubation in the PDMS chip (with or without glass diffusion barrier), the cells were fixed with paraformaldehyde (4%, w/v) for 15 min, washed with PBS, and incubated in glycerol (100 mM in PBS) for 15 min at RT. Permeabilization was achieved by treating the samples with Triton X-100 (0.1%, v/v, in PBS) for 10 min. Samples were then incubated with normal goat serum (5%, v/v, in PBST) for 1 h to block nonspecific binding sites. Samples were washed with 1% goat serum and incubated overnight at 4 °C with primary antibody (Chicken anti-human GFAP IgY, 1:3000, v/v in 1% goat serum). After incubation, samples were washed 3 times with 1% goat serum (5 min each), and incubated for 1 h at 37°C with secondary antibody (AlexaFluor 488 anti-chicken IgY, 1:500, v/v in 1% goat serum) (144). Nuclear staining was performed using DAPI (0.5 µg/mL in PBS) for 10 min. Then, samples were washed with PBS and imaged using CLSM.

3.2.3.6 Invasion assay under normoxic and hypoxic conditions

For invasion assay, spheroids composed of U87-EGFP cells in co-culture with HMC3 microglia were generated. Firstly, the cells were seeded into ultra low attachment plates ($3.5x10^3$ U87 cells/100 µL and $1.5x10^3$ HMC3 cells/100 µL) and incubated for 72 h to form compact spheroids. Then, they were transferred into printed hydrogels and crosslinked using UV light (365 nm, 2 min). Spheroid containing hydrogels were placed at the center of the PDMS chips, either with or without a glass diffusion barrier, to establish normoxic and hypoxic conditions, respectively. The samples were then incubated in a CO_2 incubator for 5 days and imaged every 24 h using CLSM. Invasion capacity under normoxic and hypoxic conditions was assessed by measuring the distance migrated by U87-EGFP cells from the spheroid boundary into the hydrogel, reflecting their ability to infiltrate the surrounding matrix.

3.2.3.7 Visualization of nutrients and drug flow

Nutrient and drug transport to the cells within the 3D structure in the chip was achieved by diffusion. In order to model nutrient and drug diffusion, a fluorescein molecule (5 μM) was mixed with culture medium and introduced into the chip through medium channels. The distribution of fluorescein was then monitored using CLSM (122). The fluorescence intensity correlated with the concentration of diffused fluorescein to confirm a transport pattern decreasing from the periphery toward the center, consistent with diffusion based delivery.

3.2.3.8 Testing of the model with temozolomide drug treatment

The GBM model was tested by assessing the response of the cells to temozolomide (TMZ) treatment and determining the half-maximal inhibitory concentration (IC_{50}). The cell loaded hydrogels were maintained within the hypoxia chips for 7 days. Following incubation, the culture medium was replaced with fresh medium containing TMZ at varying concentrations (0-5000 μM), and incubated in a CO_2 incubator. Following 72 h of drug exposure, cell viability was assessed using the Alamar Blue assay, as described in Section 3.2.2.6 (150, 151). The IC_{50} values were calculated from a dose-response curve generated by plotting cell viability against the logarithm of TMZ concentration. As a control, cells grown on 2D monolayers, as well as those loaded in hydrogels under normoxic conditions, were used.

3.2.4 Statistical analysis

Statistical comparisons among groups were performed using two-way analysis of variance (ANOVA), followed by Bonferroni's post hoc test using GraphPad Prism software (152). Data were presented as mean ± standard deviation (SD), and p-value < 0.05 was considered statistically significant. For proteomic data, differential protein expression was assessed using an unpaired, two-tailed Student’s t-test with Benjamini-Hochberg correction for false discovery rate (FDR < 0.05). Proteins exhibiting a fold change ≥ 1.2 along with an adjusted p-value below 0.05 were considered significantly altered.

4 RESULTS

4.1 Preparation of Composite Hydrogels

4.1.1 Production of dECMs

Two distinct methods were employed for brain tissue decellularization. The first method combined a physical disruption technique (freeze-thaw cycling) with the application of a nonionic detergent, Triton X-100, to effectively eliminate cellular components. The freeze-thaw process facilitates membrane disruption through intracellular ice crystal formation, thereby promoting cell lysis; however, it does not completely remove nuclear material (153). Triton X-100 treatment was used to enhance decellularization. Also, the decellularized tissues were subjected to DNase treatment to effectively clear DNA content. For comparison, brain tissue was also decellularized with sodium dodecyl sulfate (SDS) combined with DNase. Decellularized ECMs (dECM1 and dECM2) were characterized in terms of the efficiency of decellularization with DAPI and Hematoxylin Eosin stainings to evaluate the removal of cellular components in dECMs. Additionally, DNA was isolated from dECMs, and decellularization efficiency was determined quantitatively in terms of the removal of DNA content. dECMs obtained were to be used as bioinks for 3D printing, therefore, they were solubilized enzymatically with pepsin and neutralized to pH 7.4. Both dECMs (10 mg/mL) were viscous at room temperature and able to form hydrogels after 1h incubation at 37 °C.

4.1.2 Characterization of dECMs

4.1.2.1 Determination of dsDNA in decellularized samples

According to the established criterion, efficient decellularization is defined by a residual dsDNA content below 50 ng per mg of tissue (154). The residual DNA contents in dECM1 and dECM2 were 39 ± 10 and 72 ± 20 ng/mg tissue, respectively (Figure 9). Both decelularization protocols were effective in removing DNA content; however, dECM1 achieved better elimination of dsDNA and met the criterion.

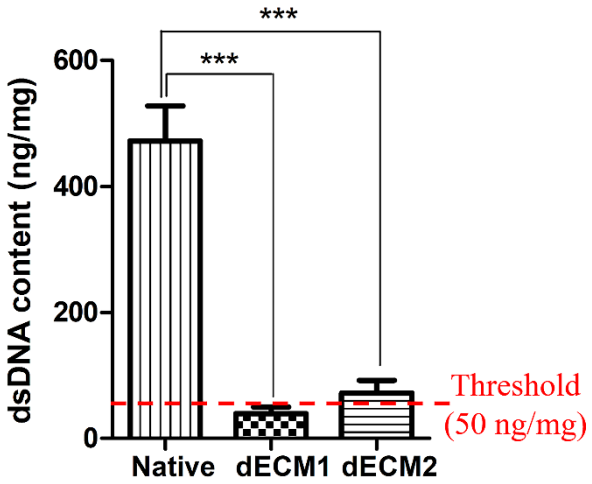

Figure 9 dsDNA content per mg sample.

4.1.2.2 Microscopic analysis for cellular components in dECMs

Cellular components of native brain tissue and dECMs were examined microscopically after staining the nuclei with DAPI. The DAPI stained images (Figure 10) confirmed the efficacy of the decellularization protocols as there were no nuclei in dECM1 or dECM2. H&E staining was employed to visualize cellular nuclei and extracellular matrix components. Hematoxylin selectively binds to nucleic acids, staining cell nuclei in purple, while eosin nonspecifically stains cytoplasmic and extracellular components in varying shades of pink. The images confirmed the efficacy of the decellularization protocols showing no cell nuclei in the H&E image of the dECMs while preserving the extracellular matrix.

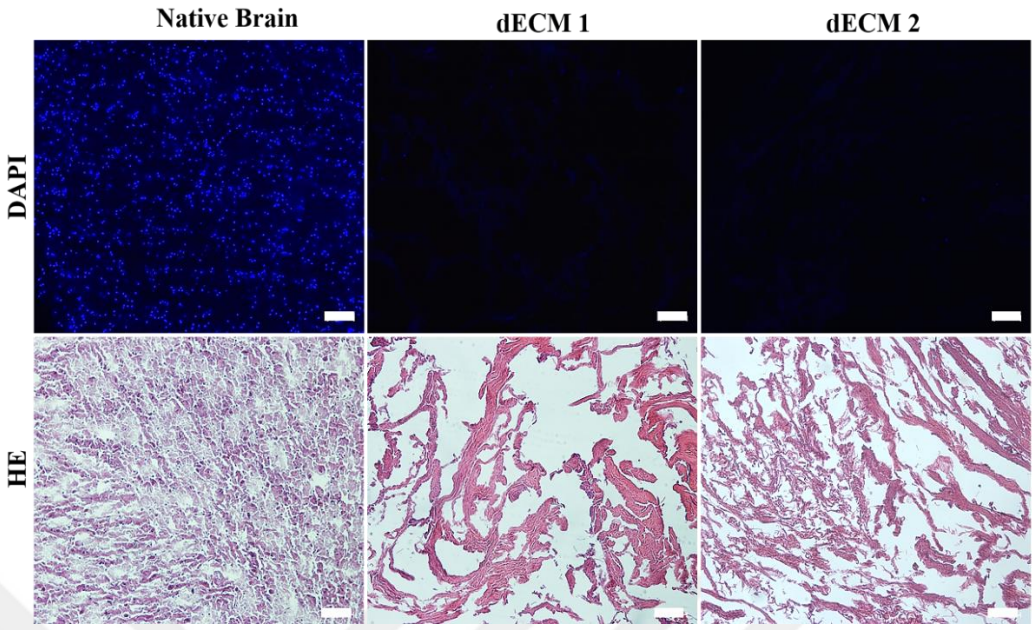

Figure 10 DAPI and H&E images of the unprocessed brain tissue and the dECMs. Scale bar: 100 μm.

4.1.2.3 Sulfated glycosaminoglycan quantification

Following decellularization, the dECMs obtained from the two protocols were analyzed for their sGAG retention using a colorimetric 1,9-dimethylmethylene blue (DBBM) assay. A calibration curve was prepared using chondroitin sulfate standards (Appendix 1). The analysis revealed that dECM1 (5.08 ± 0.35 μg/mg) retained more sGAG compared to dECM2 (4.07 ± 0.03 μg/mg) (Figure 11).

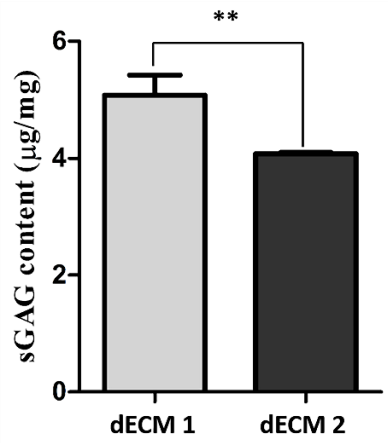

Figure 11 sGAG contents of dECMs.

4.1.2.4 Protein profiles before and after decellularization

Total protein contents of dECMs were determined by BCA assay. A standard curve was prepared using BSA concentrations (Appendix 2). Protein amounts were found to be 200.5 ± 1.1, 252.1 ± 2.4 and 186.7 ± 8.8 µg/mg for native tissue, dECM1 and dECM2, respectively (Figure 12A). The protein profiles of the dECM samples were analyzed by SDS-PAGE (Figure 12B). The samples were run at 100 V for 10 min and 120 V for 1 h and then stained with Coomassie Blue for 30 min. Both dECMs had protein bands at various molecular weight regions (155). Notably, the protein bands in dECM1 appeared more intense compared to dECM2, suggesting a higher degree of protein preservation. In terms of protein amount and profile, dECM1 was better compared to dECM2**.** This finding is consistent with previous studies reporting that Triton X-100 based decellularization better preserves extracellular matrix proteins, whereas SDS treatment often leads to the depletion of essential structural molecules (156). In order to support these findings, dECM1 subjected to proteomic analysis using LC-MS/MS. This revealed a wide range of ECM related proteins, including type VI collagen chains and laminin subunits, key components of both brain tissue and glioblastoma. Gene ontology enrichment analysis showed that the identified proteins are primarily involved in extracellular matrix specific functions, such as matrix organization and collagen interaction (Appendix 3), reinforcing the biochemical relevance of dECM1 to the native ECM.

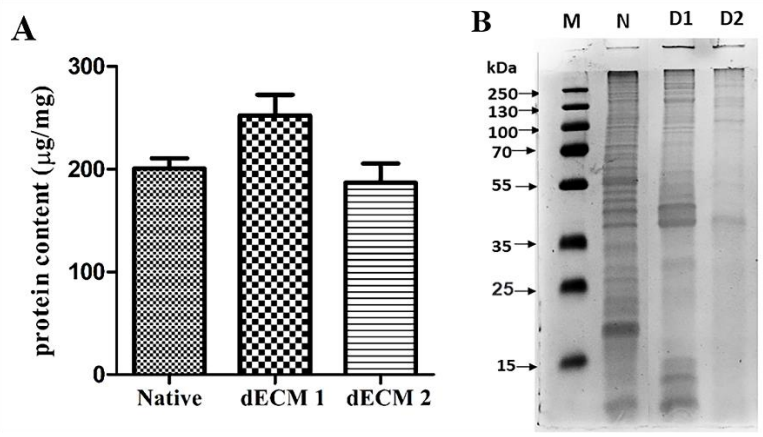

Figure 12 (A) Total protein content, and (B) SDS-PAGE of dECMs. N= native brain, D1= dECM1; D2= dECM2; Marker = PageRuler Plus, 10-250 kDa.

4.1.2.5 FTIR of the dECMs

FTIR was employed to examine the dECM samples and native brain tissue. The samples were scanned in the 400-4000 cm^{-1} range. Retention of extracellular matrix components is a critical parameter for assessing the efficacy of decellularization. FTIR spectra for dECMs and native tissue showed similar spectral profiles, particularly at characteristic amide bands indicative of protein content (Figure 13). Amide I band (1700-1600 cm^{-1}) corresponds to C=O stretching vibrations, while Amide II band (1575-1480 cm^{-1}) originates from N-H bending and C-N stretching of peptide bonds. Amide III band (1350-1220 cm^{-1}) includes signals from N-H and C-H bending as well as C-N stretching. Additionally, Amide A band (3500-3300 cm^{-1}) is associated with N-H stretching vibrations, reflecting the structural features of peptide linkages (136, 157). The identified bands indicated that proteins were retained throughout the decellularization process with each protocol. Additionally, considering the lipid-rich nature of the brain tissue, lipid-related bands were examined to assess the decellularization efficiency in terms of the removal of the lipid components. Unlike the native brain tissue, the characteristic lipid associated absorption peaks, specifically the CH_2 and CH_3 stretching vibrations (2800-3000 cm^{-1}) and the ester carbonyl (C=O) stretching at 1740 cm^{-1}, were not detected in either dECM samples, indicating the efficient elimination of lipid content during the decellularization processes.

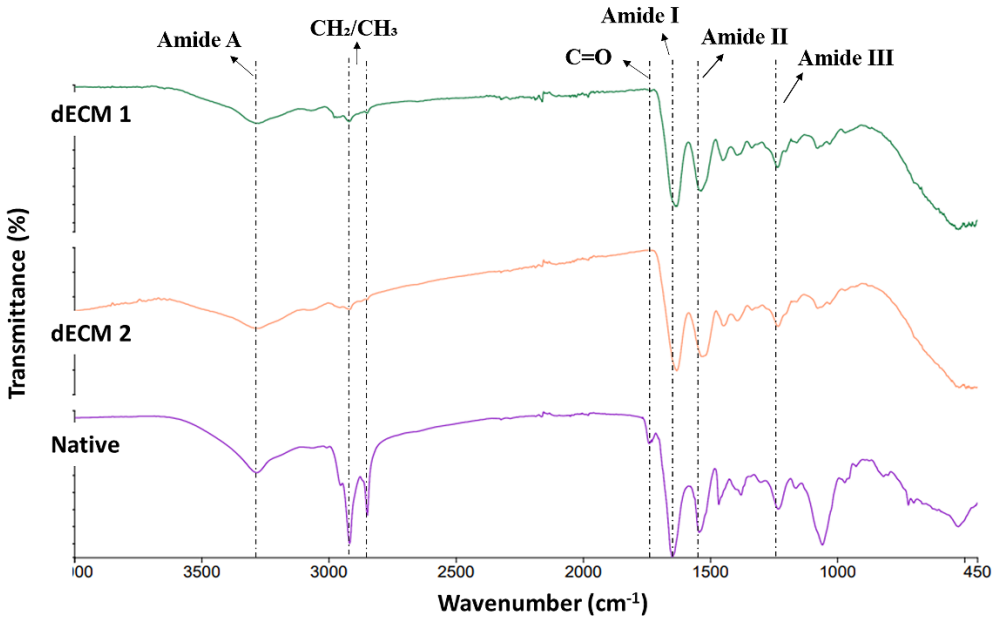

Figure 13 FTIR spectra of the native and decellularized brain tissues.

4.1.2.6 Gelation behavior of dECMs with turbidimetry

Gelation behavior of dECMs was examined using turbidimetry analysis. Temporal changes in normalized absorbance were recorded and plotted (Figure 14), enabling quantitative assessment of gelation dynamics. Key parameters derived from the curves included the time to reach 50% of maximum gelation ($T_{1/2}$), the time to achieve near complete gelation (t_{95}), and the gelation rate (S), which was determined from the slope at $T_{1/2}$ under the assumption of linear behavior during the early phase of gelation (Table 4). In the gelation kinetics plotted as time vs absorbance, the slope indicates the rate of gelation. The results indicated that dECM1 (slope 0.0770) underwent gelation almost 2 fold faster than dECM2 (slope 0.0391). The time to 95% gelation (t_{95}) was 44 min for dECM1 compared to 51 min for dECM2.

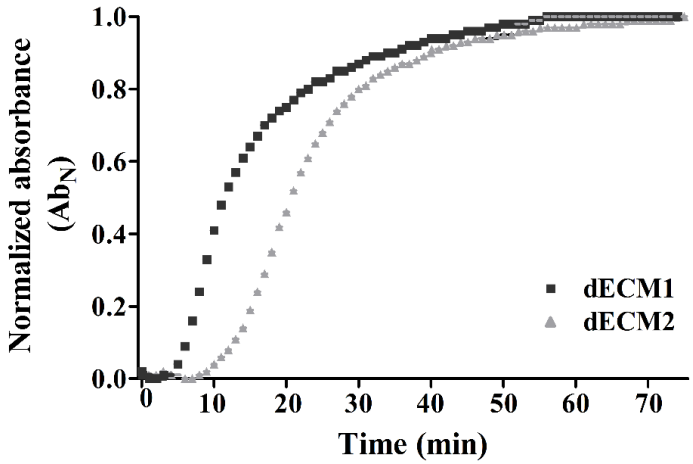

Figure 14 Turbidimetric gelation behavior of dECM hydrogels

Table 4 Gelation behavior parameters of dECM hydrogels

	Gelation rate (S)	**t1/2 (min)**	**t95% (min)**
D1	0.0770	13	44
D2	0.0391	22	51

4.1.2.7 Mechanical properties of dECM hydrogels by single frequency testing

Gelation kinetics and mechanical characteristics of dECMs were assessed using single frequency rheological analysis (Figure 15). The gelation was defined by the crossover point at which the elastic modulus (G′) exceeded the viscous modulus (G″), occurring markedly earlier for dECM1 (30 s) than for dECM2 (600 s). At equilibrium, dECM1 exhibited higher mechanical stiffness, with an elastic modulus of 4.17 ± 0.06 Pa and a viscous modulus of 1.95 ± 0.04 Pa. In contrast, dECM2 presented a lower elastic modulus (3.39 ± 0.05 Pa), while its viscous modulus (1.97 ± 0.04 Pa) remained comparable. These findings suggest that dECM1 forms a more rapidly and mechanically robust network, highlighting its suitability for applications requiring accelerated gelation and enhanced structural integrity.

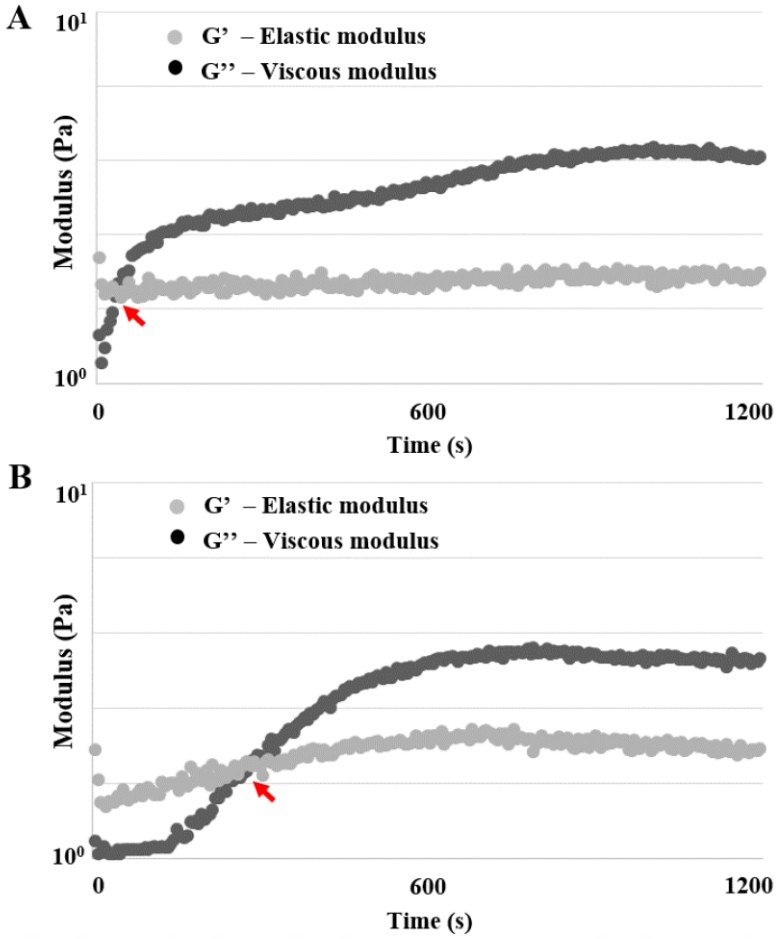

Figure 15 Single frequency sweeps of (A) dECM1 and (B) dECM2 at 37 °C. The red arrow indicates the cross over point at which gelation is initiated.

4.1.2.8 Viability of glioblastoma cells in dECM hydrogels

Cell viability within the dECM hydrogels was assessed using Live/Dead analysis. On Day 1, over 90% of glioblastoma cells remained viable in both dECM1 and dECM2 hydrogels (Figure 16). Notably, a greater number of elongated and branched cells (indicated by red arrows) were observed in dECM1 (Figure 16A) compared to the dECM2 hydrogel (Figure 16B). Additionally, cell clusters were observed in both dECM hydrogels.

On Day 7, the percentage of dead cells did not increase in any of the hydrogels, and cell viability remained above 90% (95.4 and 90.7% for dECM1 and dECM2, respectively), suggesting that the hydrogels effectively supported cell survival over an

extended culture period. dECM hydrogels provide a variety of ECM molecules that support integrin mediated cell adhesion. The elongated and branched cell morphology observed in the hydrogels demonstrates cell adhesion to the dECM matrix (158). By Day 7, the cells in the dECM hydrogels exhibited extensive spreading and network formation. In the dECM1 hydrogel (Figure 16C), cellular organization was predominantly centered around clusters (highlighted with white arrows), with intercellular interactions and branched extensions. Similar morphology and network were noted in the dECM2 hydrogel (Figure 16D), although cluster centered organization appeared more prominent in dECM1.

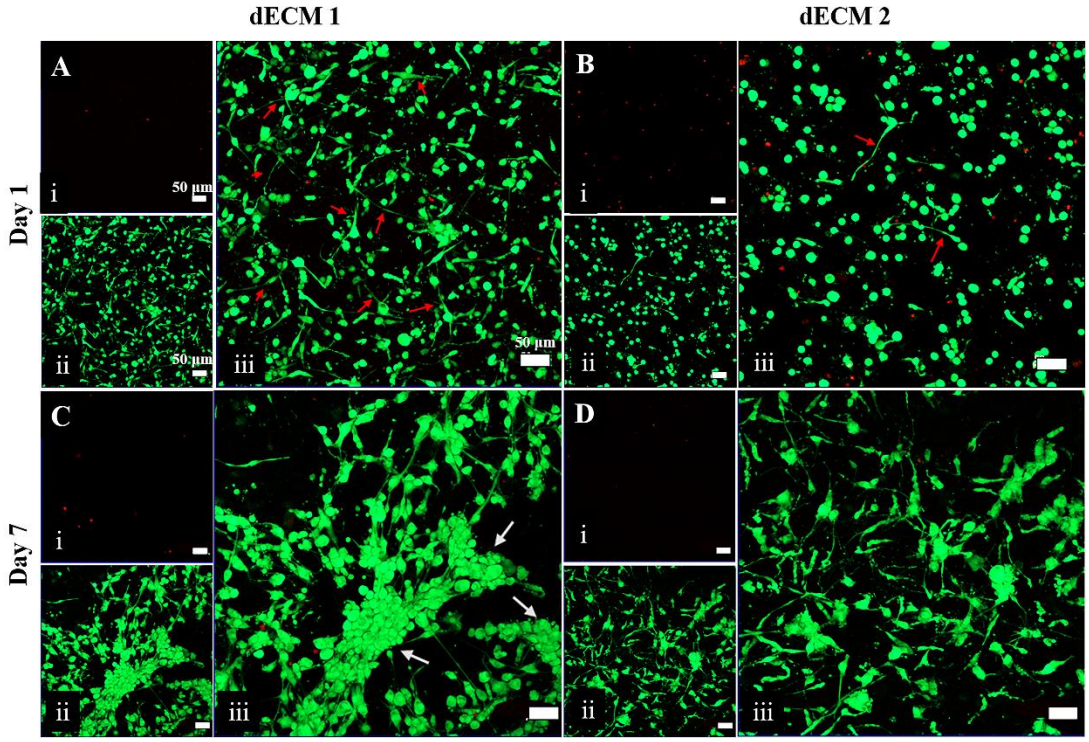

Figure 16 Live/Dead analysis of U87 cells loaded in (A, C) dECM1, and (B, D) dECM2 hydrogels. (A, B) 1 day, (C, D) 7 days after cell seeding. (i) Dead cells were stained with ethidium homodimer-1 (red), (ii) live cells were stained with calcein AM (green), and (iii) merged images. Scale bar: 50 µm. Red arrow: elongated cells. White arrow: cell clusters.

4.1.3 Characterization of hyaluronic acid methacrylate

The degree of methacrylation (DoM) was assessed through ^{1}H-NMR analysis of both HA and its methacrylated derivative (HAMA). DoM, defined as the proportion of methacrylate groups substitutions per disaccharide unit of HA, was calculated based on the integral ratios of characteristic methacrylate peaks (~6.1, 5.6, and 1.85 ppm) to the inherent methyl peak of HA (~1.9 ppm) (140). ^{1}H NMR spectroscopy confirmed the methacrylation reaction of hyaluronic acid, showing the methacrylate peaks at ~6.1, 5.6, and 1.85 ppm (Figure 17), and the degree of methacrylation was determined to be approximately 54%.

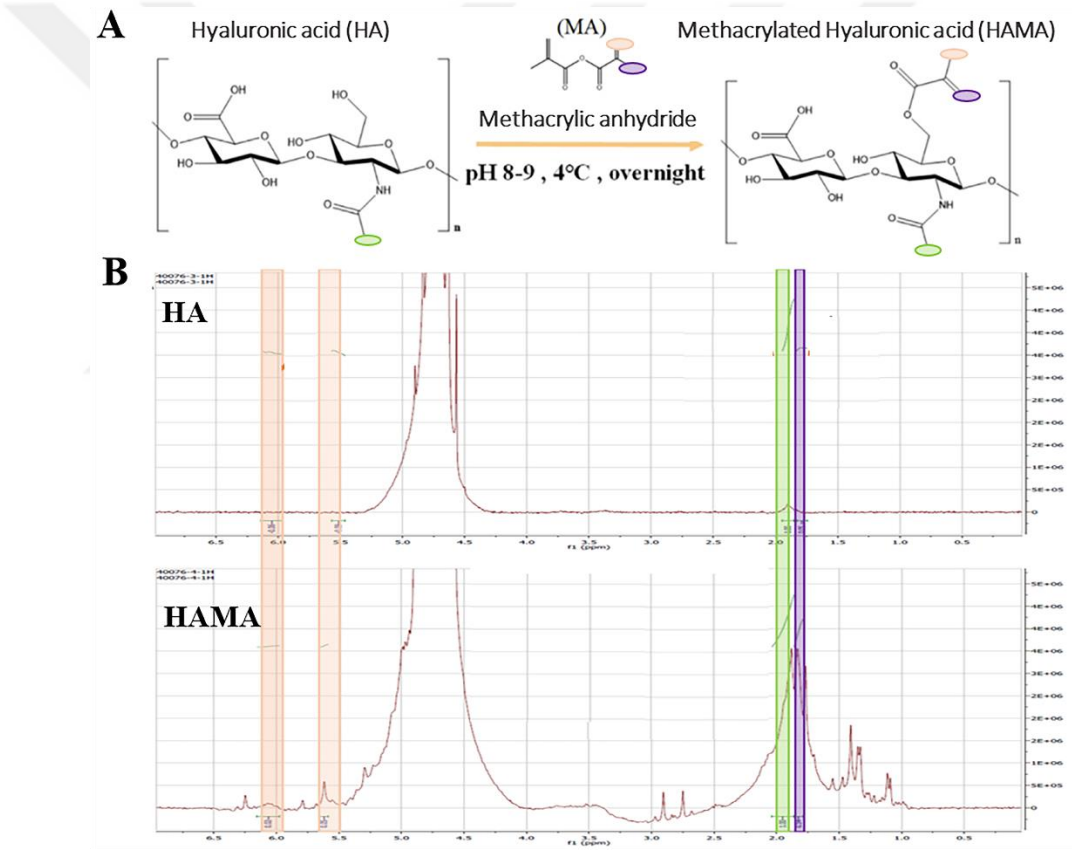

Figure 17 Synthesis of HAMA. (A) Methacrylation reaction of hyaluronic acid. (B) ^{1}H-NMR spectra of hyaluronic acid and hyaluronic acid methacrylate (two protons of the methylene carbon on the methacrylate group: 6.1 and 5.6 ppm; ten protons of the carbohydrate backbone between: 4.2 to 3 ppm; three protons on the methyl groups of the N-acetylglucosamine subunit: 1.9 ppm; three protons on the methyl groups of methacrylate: 1.85 ppm).

FTIR analysis further confirmed the methacrylation of hyaluronic acid (Figure 18). The appearance of a distinct absorption band in the 1720-1740 cm^{-1} range was attributed to C=O stretching vibrations, indicating ester bond formation between hyaluronic acid and methacrylic anhydride. Additionally, a peak observed around 1630-1650 cm^{-1} corresponded to C=C stretching vibrations, confirming the incorporation of methacrylate groups (142). A band between 3200-3600 cm^{-1} was also detected, representing O-H stretching vibrations present in both hyaluronic acid and the methacrylated derivative.

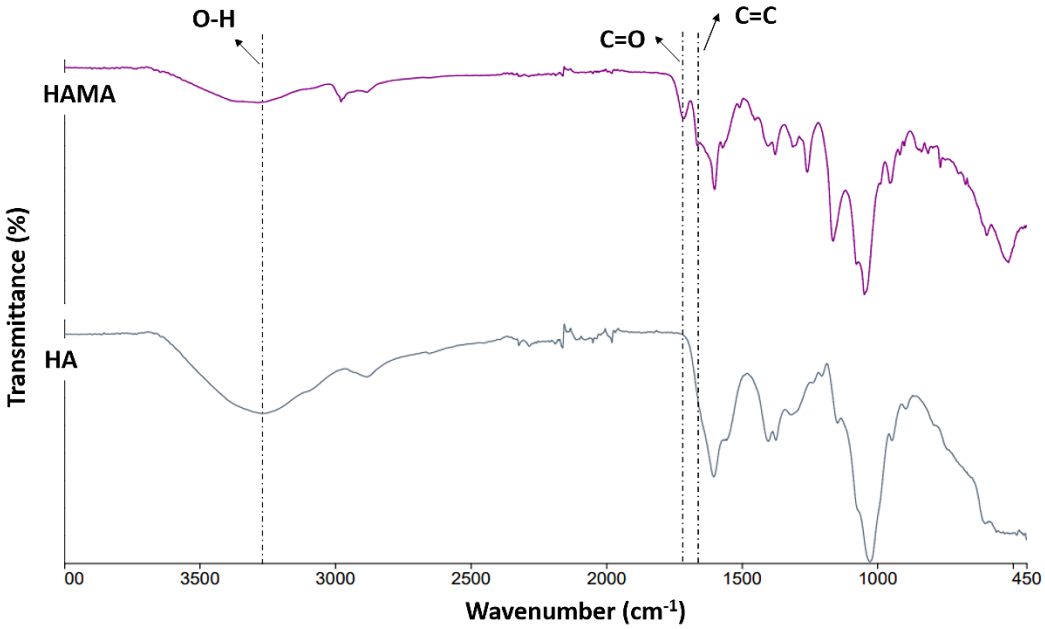

Figure 18 FTIR spectra of the HA and HAMA.

4.1.4 Characterization of composite hydrogels

HAMA/dECM solutions were subjected to UV light (365 nm, 1.6 J/cm^2) for different durations (1, 2, 3, and 4 min) to examine crosslinking efficiency. The hydrogel slabs were imaged using camera (Figure 19). Visual assessment revealed that 1 min of UV exposure was insufficient to achieve complete crosslinking of the hydrogel solution; however, 2 min or more UV exposure time resulted in crosslinked hydrogel.

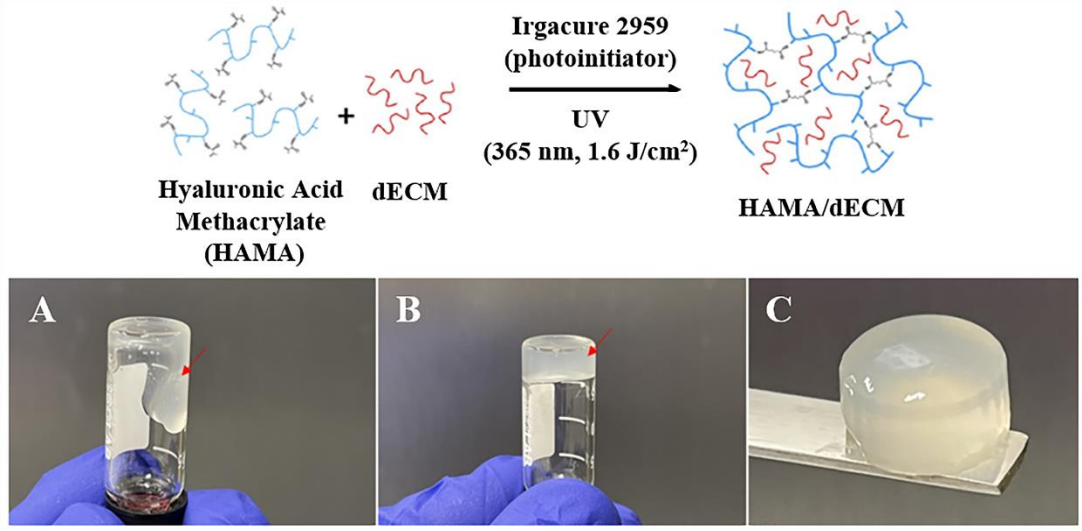

Figure 19 HAMA/dECM composite hydrogel formation by exposure to UV (365 nm, 1.6 joule/cm^2). The hydrogel solution was (A) free flowing before UV exposure and (B) underwent a sol-gel transition and formed a stable hydrogel network following UV crosslinking. (C) Side view.

4.1.4.1 FTIR of the composite hydrogels

The presence of HAMA and dECM in the structure of the composite hydrogels (HAMA/dECM) was determined by FTIR (Figure 20). The presence of HAMA was determined from methacrylate-related ester bands (1730 cm^{-1} and 1665 cm^{-1}) which also showed in the HAMA spectra (Figure 18). The presence of dECM was confirmed by characteristic protein associated amide bands observed in the FTIR spectra. As a control, HAMA and dECM hydrogels were used. FTIR spectra demonstrated the presence of HAMA and dECM in the composite hydrogels. The composite hydrogel exhibited distinct peaks around 1730 cm^{-1} and 1665 cm^{-1}, corresponding to methacrylate associated functional groups and confirmed the presence of HAMA. Further, different from HAMA hydrogel, composite hydrogel showed peaks at regions of amide I (1700-1600 cm^{-1}), amide II (1575-1480 cm^{-1}), and amide A (3300-3500 cm^{-1}), confirming the incorporation of dECM within the composite matrix.

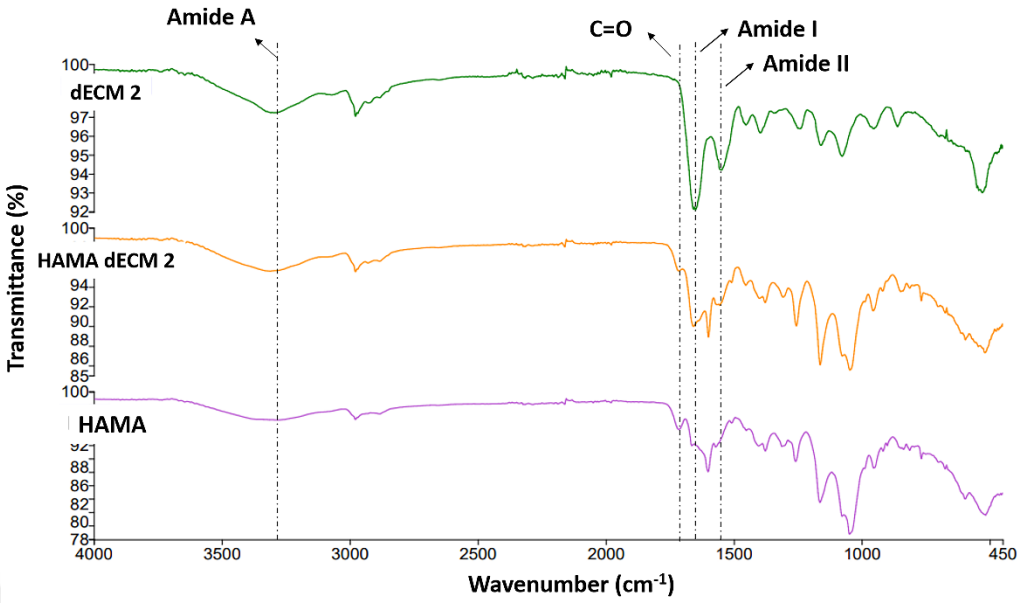

Figure 20 FTIR spectra of HAMA, HAMA/dECM, and dECM hydrogels.

4.1.4.2 Equilibrium water contents of the hydrogels

Hydrogels are 3D hydrophilic polymeric networks capable of swelling in an aqueous environment without dissolution. All hydrogel formulations reached equilibrium swelling within 24 h. The equilibrium water content was determined as 95.5 ± 0.3, 93.3 ± 0.3, and 90.2 ± 0.5% for 1H, 1H3D, and 3D hydrogels, respectively. The corresponding degrees of swelling (DS) values were calculated to be 2152 ± 140, 1394 ± 60, and 1394 ± 241%, respectively, indicating their high water retention capacities (Table 5).

Table 5 Equilibrium water content and degree of swelling of the hydrogels

	1H	1H3D	3D
EWC	95.5 ± 0.3%	93.3 ± 0.3%	90.2 ± 0.5%
DS	2152 ± 140%	1394 ± 60%	1394 ± 241%

4.1.4.3 Scanning electron microscopy of the hydrogels

The microstructure of the dry hydrogels was examined using SEM. All hydrogel formulations exhibited a highly porous, sponge-like structures (Figure 21). Among

them, the dECM hydrogel (3D) displayed the smallest average pore diameter (98 ± 37 µm), which was notably lower than the HAMA containing composites. No significant differences in average pore size were observed among 1H, 1H1D, 1H2D, and 1H3D hydrogels, with average pore sizes of 171 ± 24, 227 ± 42, 236 ± 33 and 270 ± 37 µm, respectively. The porous and interconnected network structures present in all hydrogel formulations suggest their suitability for survival and expansion of encapsulated cells. These structures facilitate efficient diffusion of nutrients and oxygen, enable waste removal, and provide sufficient space for cellular proliferation and migration.

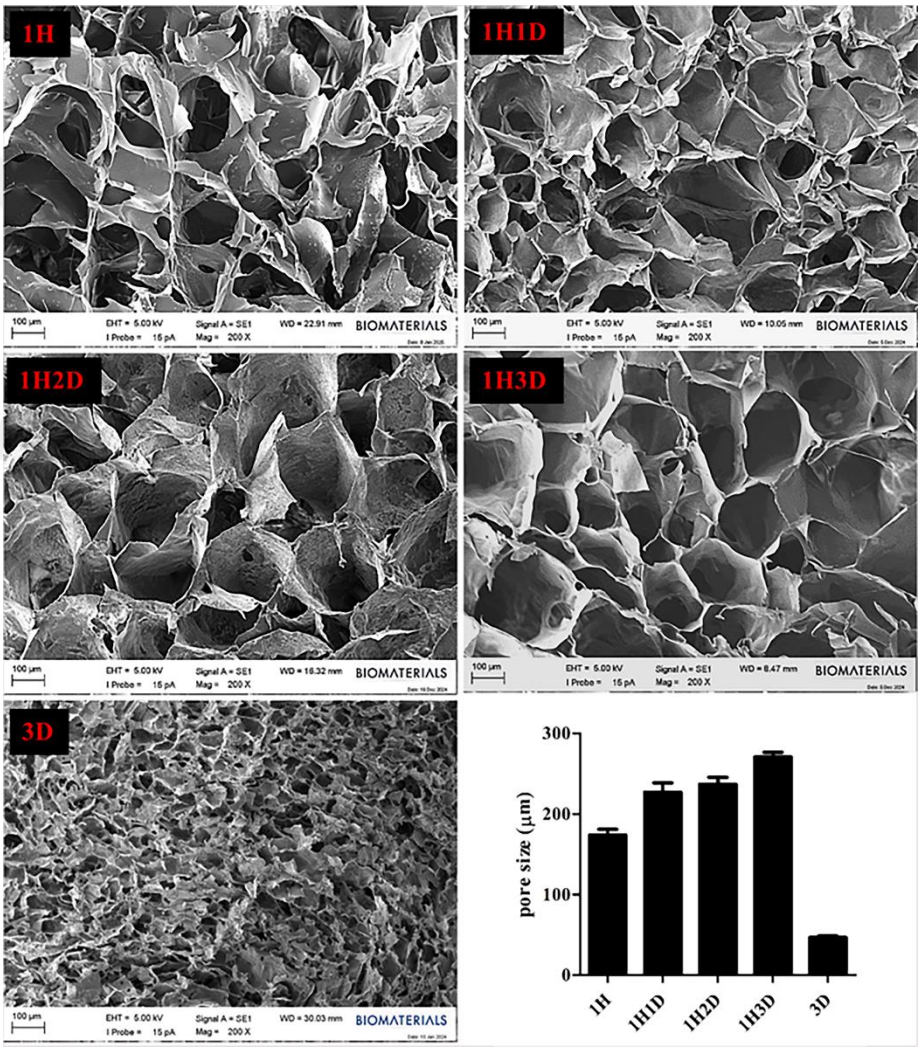

Figure 21 Scanning electron micrographs of HAMA, dECM, and HAMA/dECM hydrogels. Scale: 100 µm. The graph shows the average pore size of the hydrogels.

4.1.4.4 *In situ* degradation of the hydrogels

The degradation behavior of the hydrogels was assessed via gravimetric analysis over a 14 day period (Figure 22). Among the groups, the 3D (dECM) hydrogel exhibited the most pronounced degradation, particularly during first two days, showing up to 35% weight loss. In contrast, the 1H (HAMA) hydrogel displayed the highest structural stability, demonstrating the least degradation over time. HAMA/dECM composite hydrogels exhibited a degradation profile closely resembling that of HAMA hydrogels, with a slight increase in degradation attributed to the presence of dECM.

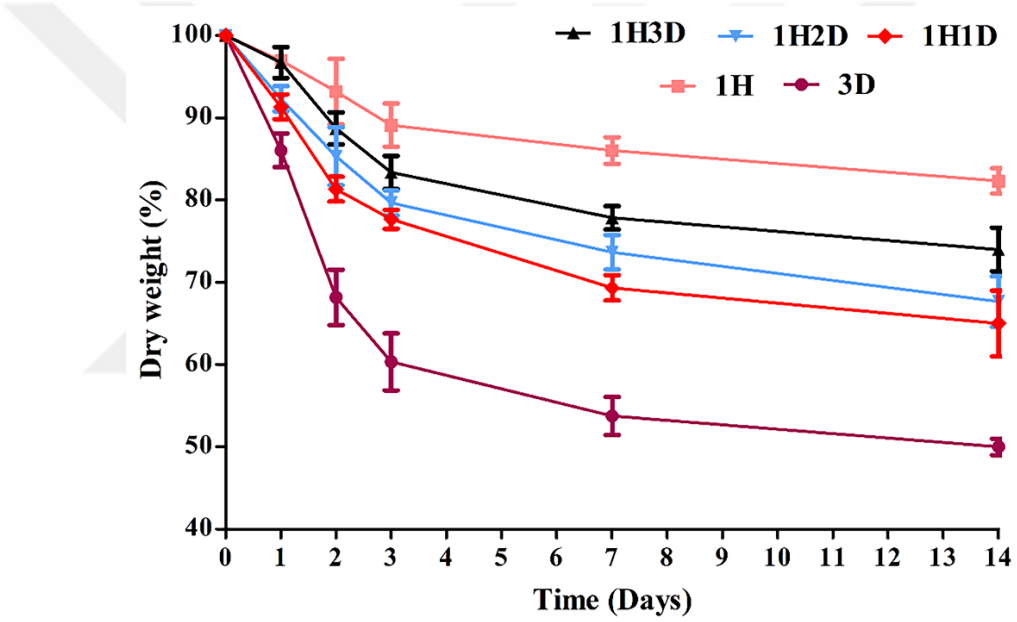

Figure 22 Degradation profiles of the hydrogels.

4.1.4.5 Compression testing of the hydrogels

Compressive mechanical tests were conducted to determine the stiffness and load bearing capacity of the hydrogels, using a crosshead speed of 0.5 mm/min. The compressive modulus was determined from the slope of the stress-strain curve (Figure 23A). The calculated moduli for 3D1, 1H, 1H1D, 1H2D, and 1H3D hydrogels were 6.11 ± 0.94, 9.91 ± 1.06, 8.15 ± 0.95, 8.33 ± 1.02, and 9.44 ± 0.73 kPa, respectively. These findings demonstrate that the presence of HAMA in the matrix increased the

stiffness of the hydrogels (Figure 23B). Although no significant differences were found between 1H1D and 1H2D groups, and increasing the dECM component to 3% (w/v) in 1H3D resulted in a statistically higher compressive modulus. Regarding compressive strength, 3D and 1H hydrogels exhibited values of 19.28 ± 1.77 kPa and 14.34 ± 0.81 kPa, respectively, with no significant difference. However, their composite form achieved a considerably higher maximum stress value of 47.42 ± 7.51 kPa. After the compression test, cracking in the 1H group and fluid leakage in 3D1 was observed. In contrast, the composite hydrogels exhibited no detectable deformation and maintained its structural integrity even after the test. This indicated that, in the composite form, the molecular structure demonstrated strong integration, while the incorporation of dECM enhanced the flexibility of the hydrogel.

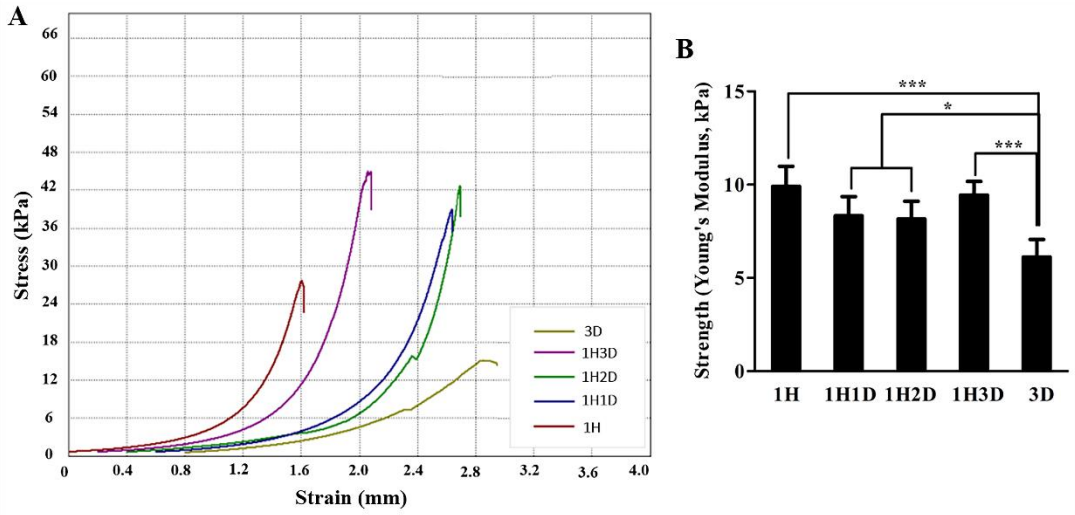

Figure 23 Compression test of the hydrogels. (A) Stress-strain curve obtained from compression test. (B) Graph showing compressive moduli of hydrogels.

4.1.4.6 Strain sweep testing of the hydrogels

The viscoelastic behavior of the hydrogels was studied by plotting the elastic modulus (G′) and viscous modulus (G″) with respect to the applied strain (γ*) (Figure 24). All hydrogel formulations exhibited a linear viscoelastic region (LVER), within which both G′ and G″ remained stable as strain increased, indicating the capacity to resist deformation (Figure 24A). The dominance of G′ over G″ confirmed the elastic-

dominant nature of the materials. Among the tested formulations, the 1H3D hydrogels showed superior viscoelastic performance, with the highest elastic modulus (458.30 ± 13.39 Pa) and viscous modulus (65.17 ± 6.46 Pa) (Figure 24B). In comparison, hydrogels with lower dECM content or dECM alone exhibited reduced stiffness, highlighting the reinforcing effect of compositional optimization.

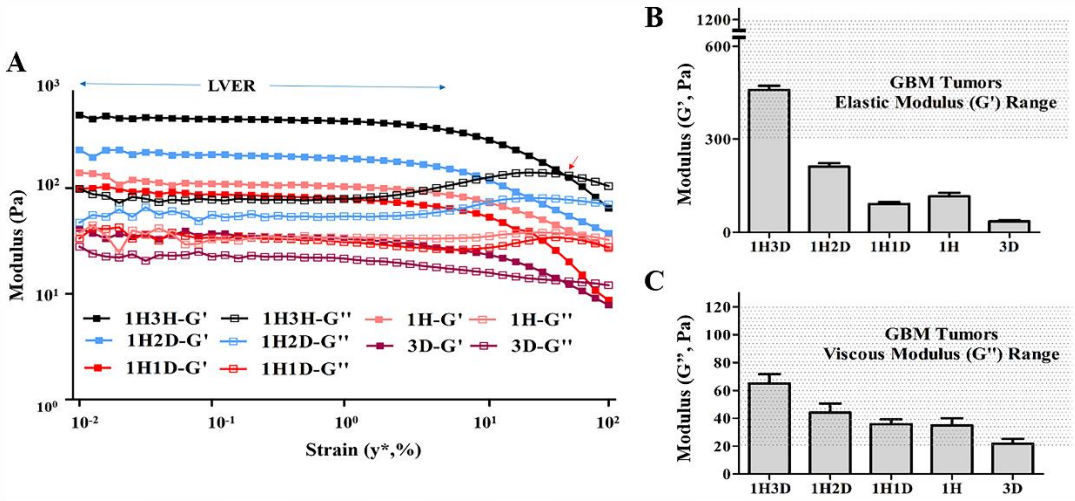

Figure 24 Rheological analysis of the hydrogels. (A) Strain sweep measurements showing elastic modulus (G′) and viscous modulus (G″) plotted against applied strain (γ*) under a constant frequency and controlled oscillatory shear. Blue bidirectional arrow: Linear viscoelastic region (LVER). Red arrow: Crossover point (G″ = G′). Graphs showing (B) elastic and (C) viscous moduli of hydrogels at LVER.

4.1.4.7 Printability analysis of the hydrogel solutions

Shear thinning and thixotropic properties of the hydrogel solutions were evaluated for their potential in extrusion based printing applications. Rheological measurements were performed at 10°C using a rotational rheometer. Shear thinning behavior was examined by a flow curve, where shear rates were increased on a logarithmic scale from 0.1 to 100 s^{-1}, while monitoring the viscosity. For the thixotropic behavior, a three step shear protocol was followed: the test started at a low shear rate (1 s^{-1}) for 30 s to establish its baseline viscosity, then was immediately followed by a high shear rate at 100 s^{-1} for 30 s to simulate extrusion conditions, and finally was back to 1 s^{-1} for 60 s to monitor the recovery in viscosity. The flow profiles (Figure 25A) showed shear thinning behaviors of all hydrogel formulations, as evidenced by the reduction in

viscosity with increased shear rate, enabling smooth extrusion from the nozzle. The composite hydrogel solutions exhibited higher viscosities compared to HAMA or dECM only formulations. Among these, the viscosity was significantly increased with increasing dECM content, and the 1H3D formulation exhibited the highest values for all shear rates tested. Thixotropic recovery was then analyzed (Figure 25B) to assess the potential of the hydrogel solutions to recover their structure after being subjected to shear stresses, simulating post printing recovery. When shear rates were returned to low values, hydrogel solutions showed a rapid viscosity increase indicative of a strong recovery in structural integrity. However, the 3D formulation without HAMA recovered more slowly than HAMA containing hydrogels. Composite matrix, specifically the 1H3D, resulted in better recovery properties due to increased molecular interaction within the matrix. Yield stress and viscosity values of the 1H3D hydrogel were also measured at different temperatures (4, 10, 18, and 24°C) (Figure 25C). The increase in yield stress with temperature indicated that higher temperatures result in greater resistance of the material against deformation. The shear thinning and thixotropic behavior of the hydrogel solution favored efficient extrusion while maintaining shape fidelity after deposition. Stable performance in the wide temperature range used also supports the applicability of 1H3D as a bioink for extrusion printing, a balance of printability with structural integrity.

The HAMA/dECM solutions with varying dECM concentrations were prepared and printed with different cartridge movement speeds and printing pressures (Table 6). The structures were printed with different internal patterns (honeycomb and grid) with four layers to determine the printability of the hydrogel solutions (Figure 25D). Although the slabs of all solutions formed a solid gel after UV exposure (365 nm, 2 min), the solutions of 1H1D and 1H2D were not viscous enough for exturion printing. Even at lower printing pressures, these solutions flowed from the nozzle. In contrast, the 1H3D solution exhibited continuous extrusion from the nozzle and was successfully printed across a range of printing pressures, speeds, and temperatures. The printed structure maintained its integrity after printing. The optimal printing parameters were determined to be a printing pressure of 0.4 bar, a cartridge movement speed of 10 mm/s, and a cartridge temperature of 10°C.

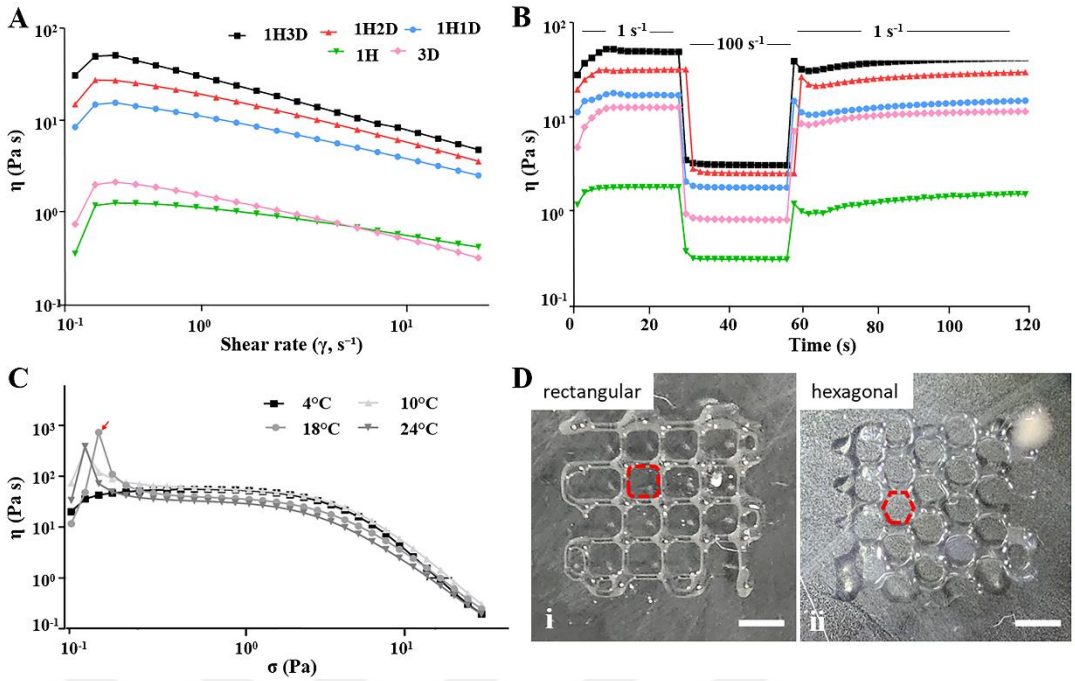

Figure 25 Printability of hydrogel solutions. (A) Steady-shear viscosity of hydrogel formulations as a function of shear rate (γ, s^{-1}). (B) Thixotropic recovery of the hydrogel formulations under varying shear rates (1 s^{-1}, 100 s^{-1}, and 1 s^{-1}). (C) Yield stress and viscosity of the 1H3D hydrogel solution, where the viscosity (η) as a function of stress (σ) at varying temperatures (4, 10, 18, and 24°C). The red arrow indicates yield stress, representing the minimum force required to initiate flow in materials that remain static under lower stress. (D) Stereomicrographs of the printed structures of 1H3D hydrogel solution, with a printing speed of 10 mm/s, printing pressure of 0.4 bar, 3 layers with (i) grid, (ii) honeycomb structure. Scale bar: 1 mm.

Table 6 Printability of HAMA/dECM solutions

Sample	Printing pressure (bar)	Nozzle movement speed (mm/s)	Temperature (°C)	Comment
1H1D	X	X	X	Fluid
1H2D	X	X	X	Fluid
1H3D	✓ (0.4 bar)	✓ (10 mm/s)	✓ 10 °C	Enough viscosity-printable

4.2 *In Vitro* Studies

4.2.1 Cytoskeleton and nuclei staining of U87 and HMC3 cells in the hydrogels

Cytoskeletal and nuclear structures of U87, HMC3, and U87/HMC3 co-cultured cells loaded within 1H, 3D, and 1H3D hydrogel slabs were examined after 7 days using Phalloidin and DAPI staining. Cells displayed limited spreading with actin filaments concentrated near the nuclei in the 1H hydrogel. The rounded morphology and absence of spreading demonstrated weak cell-matrix interactions (Figure 26A-C). In contrast, U87 cells within 3D and 1H3D matrices exhibited extensive actin filament organization, forming pronounced cytoskeletal networks, suggesting enhanced motility and structural integrity (Figure 26D, G). On the other hand, HMC3 cells showed more dispersed and less structured actin arrangements in both hydrogels (Figure 26E, H). Co-cultures presented a mixed actin pattern characteristic of both U87 and HMC3 cells (Figure 26F, I).

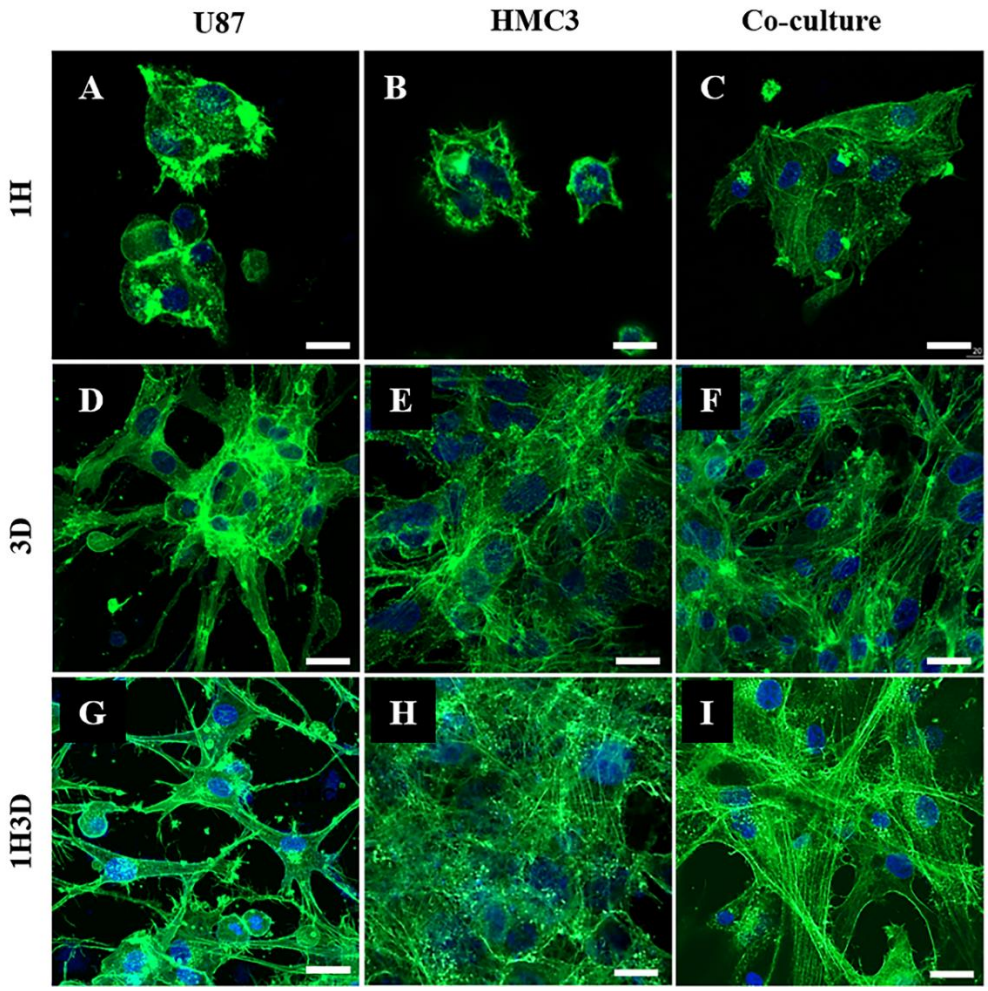

Figure 26 CLSM images of (A, D, G) U87, (B, E, H) HMC3, and (C, F, I) U87/HMC3 co-culture cells loaded in (A-C) 1H, (E-F) 3D, and (G-I) 1H3D hydrogel slabs on day 7. F-actin filaments (phalloidin; green), nucleus (DAPI: blue). Scale bar: 20 µm

4.2.2 Transfection of U87 cells with EGFP gene for live cell imaging

U87 cells were transfected with pcDNA3-EGFP plasmid which contains a gene that encodes antibiotic resistance to neomycin. G418 is an analog of neomycin sulfate and has similar mechanisms as neomycin. Therefore, stable clones of transfected U87 cells were selected by G418 treatment. The concentration of G418 which kills all non-transfected cells was determined as 550 µg/mL (Appendix 4). After 72 h of transfection, stably transfected cells were selected by G418 treatment for 3 weeks. pcDNA3-EGFP plasmid also encodes EGFP as a reporter system. EGFP expression allows cells to be distinguished using fluorescence microscopy, confocal microscopy,

and flow cytometer, and it is an important feature in determining the cell specific response.

EGFP expression in U87 cells was detected by fluorescence microscopy, and flow cytometer was used for the quantitative determination of stably transfected cells. Fluorescence microscope images (Figure 27) and flow cytometry histogram (Figure 28) of U87-EGFP cells revealed that the EGFP-labeled cells expressed a high level of EGFP. Two days after transfection, only a small fraction of cells exhibited EGFP expression. However, following 14 days of stable selection with 550 µg/mL G418, nearly all cells showed strong EGFP expression (Figure 27). Flow cytometry analysis revealed that 94% of U87-EGFP cells (Figure 28B) exhibited fluorescence signals higher than those of non-transfected U87 cells (Figure 28A), confirming the transfection and EGFP expression of U87 cells.

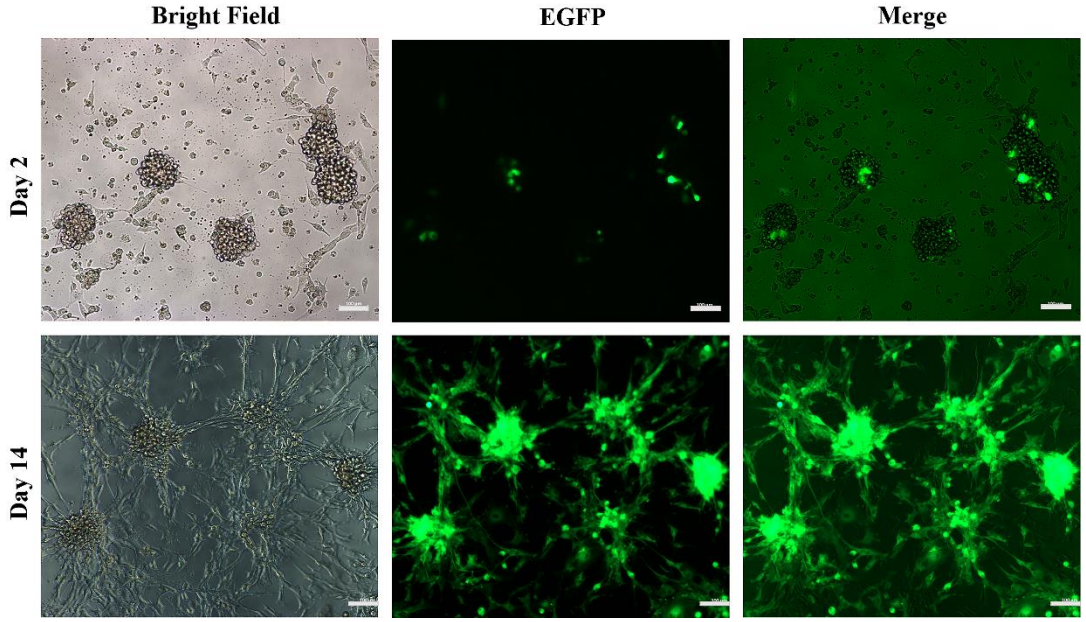

Figure 27 EGFP expression by the U87-EGFP cells were examined under light and fluorescence microscopes 2 days after transfection (upper), 14 days after antibiotic selection (below). Scale bar: 100 µm.

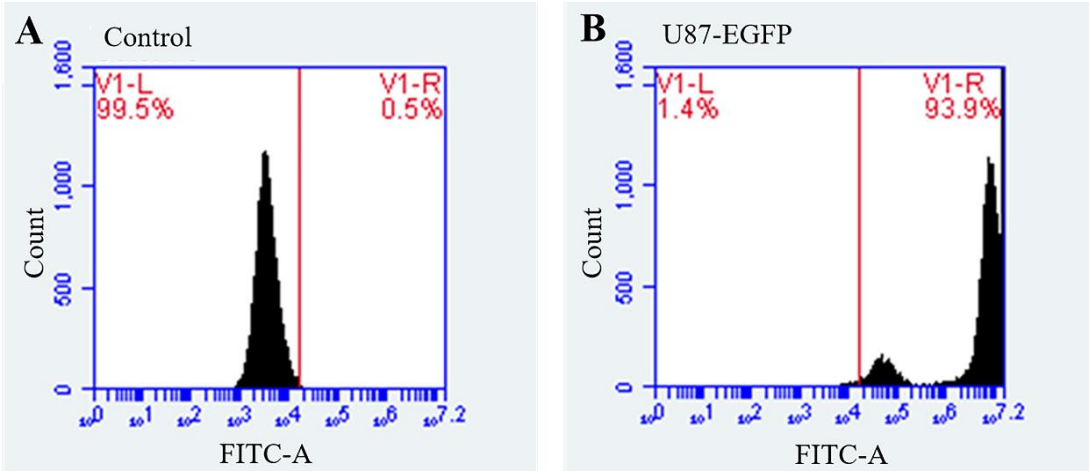

Figure 28 EGFP expression in the U87 and U87-EGFP cells were examined by flow cytometer 14 days after antibiotic selection with G418. Flow cytometry histograms, displaying fluorescence intensity (log scale) along the x-axis and cell count along the y-axis. (A) Untransfected control U87 cells, and (B) transfected U87-EGFP cells after 14 days of selection. The threshold was determined at background fluorescence with FI>10^4 units.

4.2.3 Invasion of glioblastoma cells under mono and co-culture conditions

In order to examine the invasive behavior of glioblastoma cells, an invasion assay was performed using EGFP-expressing U87 spheroids. These spheroids were embedded in hydrogel formulations under both mono and co-culture conditions. Confocal images were captured at 0, 24, and 48 h, and the the extent of invasion was quantified by measuring the distance migrated by U87-EGFP cells from the edges of the spheroids, providing a comparative assessment of their invasive potential (Figure 29). The assay was performed in 1H and 1H3D hydrogels. U87 cells showed no detectable invasion in the 1H hydrogel (Figure 29A). On the other hand, U87 cells exhibited markedly increased invasion within the composite hydrogel, indicating that this matrix provided a promigratory environment. Notably, when U87 cells were co-cultured with microglia in the composite hydrogel, the invasion distance increased by approximately 41% compared to monoculture conditions (Figure 29B), highlighting the potential influence of microglia on glioblastoma invasiveness. Additionally, quantitative gene expression analysis confirmed this finding at the molecular level (Figure 29C), showing that co-culturing U87 cells with microglia in the hydrogel led to elevated expression of genes involved in extracellular matrix remodeling and tumor

invasion, with MMP2 and MMP9 levels significantly higher than in U87 monocultures.

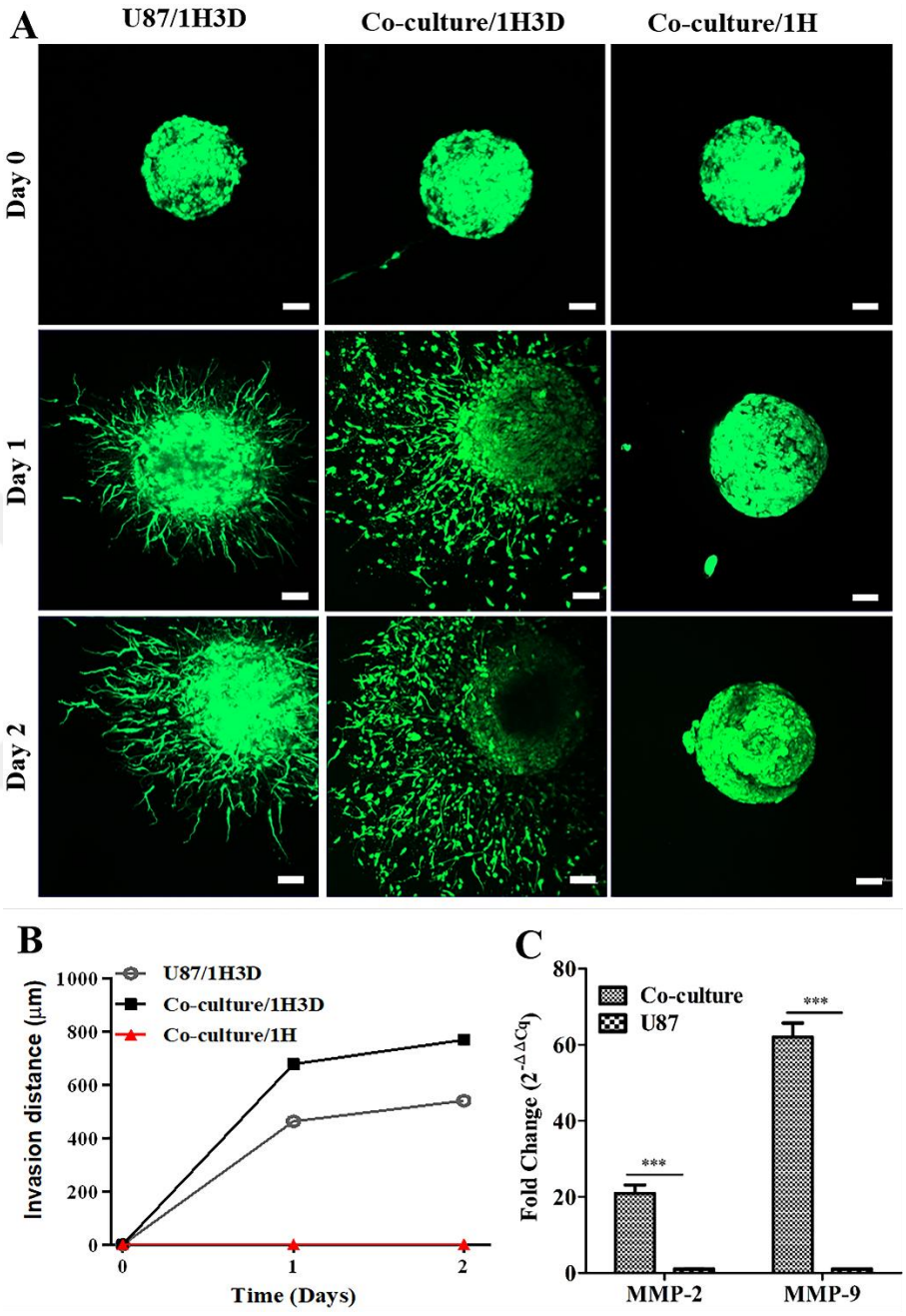

Figure 29 Glioblastoma cell invasion within hydrogel matrices. (A) CLSM images showing the migration of EGFP-labeled glioblastoma cells in the hydrogels at 0, 24, and 48 h. Scale bar: 1 mm. (B) Quantitative measurement of cell migration distances from the spheroid edges over a 2 days period. (C) Gene expression analysis of the cells cultured in 1H3D hydrogels. Data are presented as fold change ($2^{-\Delta\Delta Cq}$) relative to U87 monoculture.

4.2.4 Viability of the bioprinted glioblastoma and microglia cells

Bioink 1 containing U87 cells (10^7 cells/mL) and 1H3D, and Bioink 2 containing HMC3 cells (10^7 cells/mL) and 1H3D were printed using the optimized parameters. Bioink 1 was initially printed as a four layer inner structure, with Bioink 2 subsequently printed around it to form a border (Figure 30).

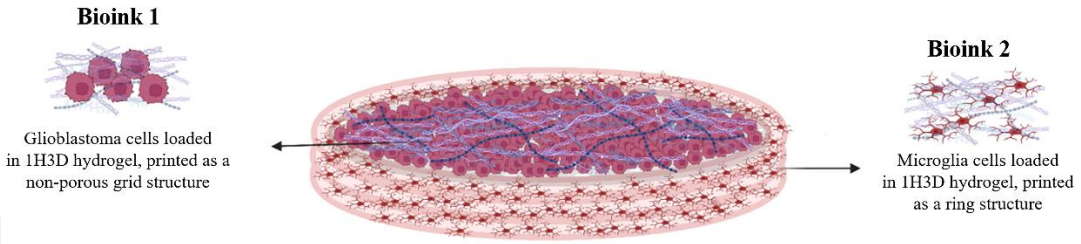

Figure 30 Schematic representation of 3D bioprinted model. Inner structure composed of Bioink 1 (U87 cells in 1H3D) was printed as 4 layers, then Bioink 2 (HMC3 cells in 1H3D) solution was printed as the border for the printed Bioink 1.

Viability of the cells in the printed structure was examined using Live/Dead and Alamar Blue assays. The viability of U87 cells (Figure 31) were determined on days 1, 3, 7, and 14 as 93.7, 93.2, 97.4 and 98.2%, respectively, whereas the viability of HMC3 cells (Figure 32) were determined as 92.5, 94.4, 98.4, and 99.1%, respectively. The high viability of the cells demonstrated that the hydrogel matrix and printing process provided a supportive and biocompatible environment conducive to cell survival, for at least 14 days. Furthermore, the co-culture condition also maintained over 90% cell viability (Figure 33), indicating a favorable interactions between the two cell types.

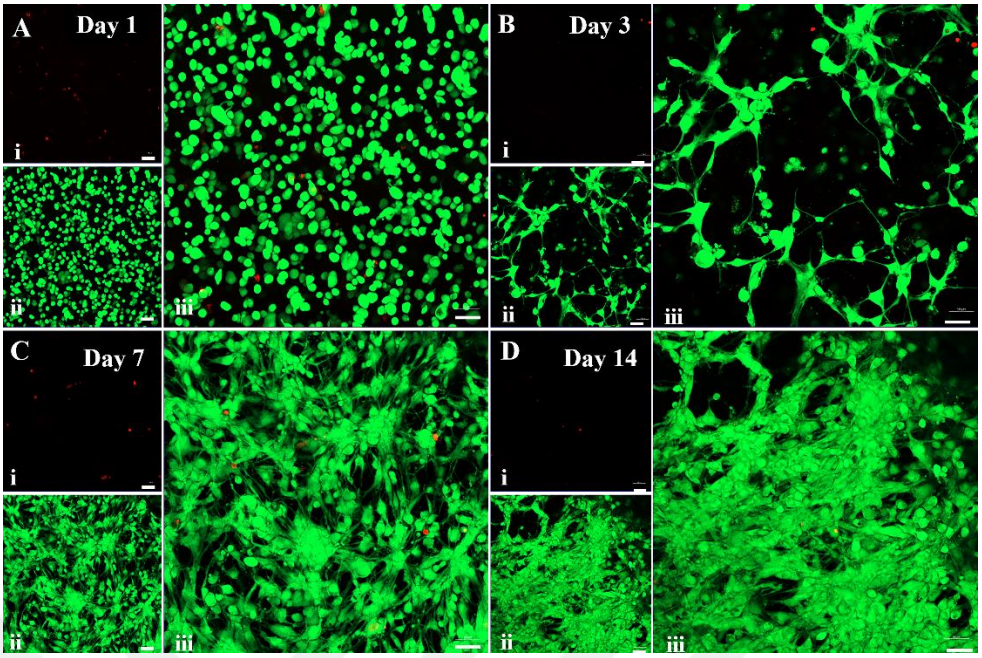

Figure 31 Live/Dead analysis of U87 cells entrapped in the hydrogel of 1H3D. (A) Day 1, (B) Day 3, (C) Day 7, and (D) Day 14. (i) The dead cells (stained with ethidium homodimer-1, red), (ii) the live cells (stained with calcein AM, green) and (iii) merged. Scale bar: 50 μm.

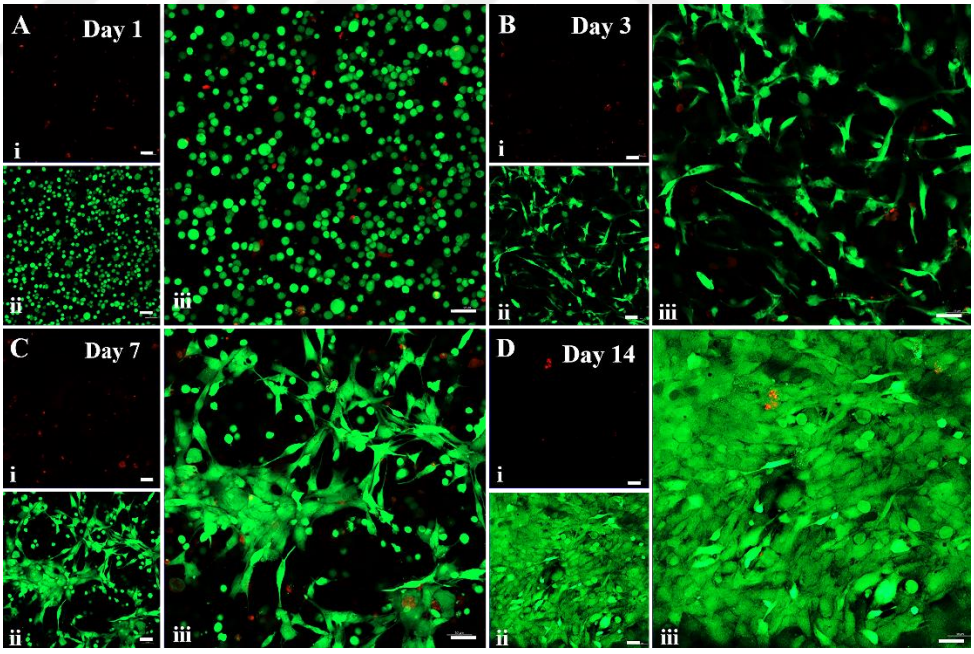

Figure 32 Live/Dead analysis of HMC3 cells entrapped in the hydrogel of 1H3D. (A) Day 1, (B) Day 3, (C) Day 7, and (D) Day 14. (i) The dead cells (stained with ethidium homodimer-1, red), (ii) the live cells (stained with calcein AM, green) and (iii) merged. Scale bar: 50 μm

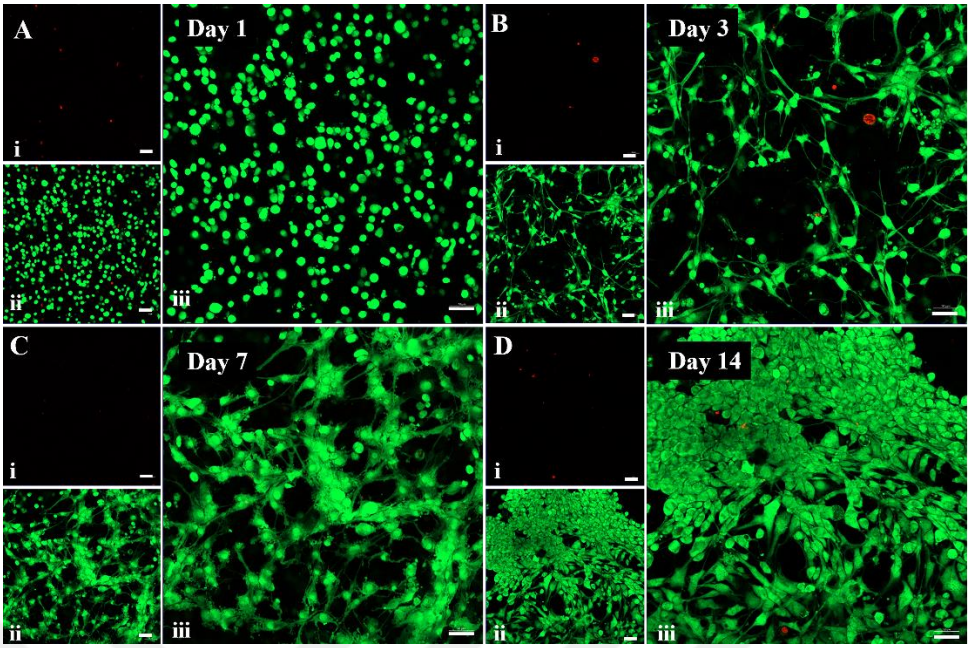

Figure 33 Live/Dead analysis of U87/HMC3 co-culture cells entrapped in the hydrogel of 1H3D. (A) Day 1, (B) Day 3, (C) Day 7, and (D) Day 14. (i) The dead cells (stained with ethidium homodimer-1, red), (ii) the live cells (stained with calcein AM, green) and (iii) merged. Scale bar: 50 μm

Additionally, time dependent increases in metabolic activity were observed across all groups, reflecting cell proliferation (Figure 34). While U87 and HMC3 cells exhibited similar growth patterns, the co-culture condition showed a significantly higher metabolic activity than the single cell cultures, suggesting synergistic interactions between glioblastoma and microglia cells that enhance cellular proliferation.

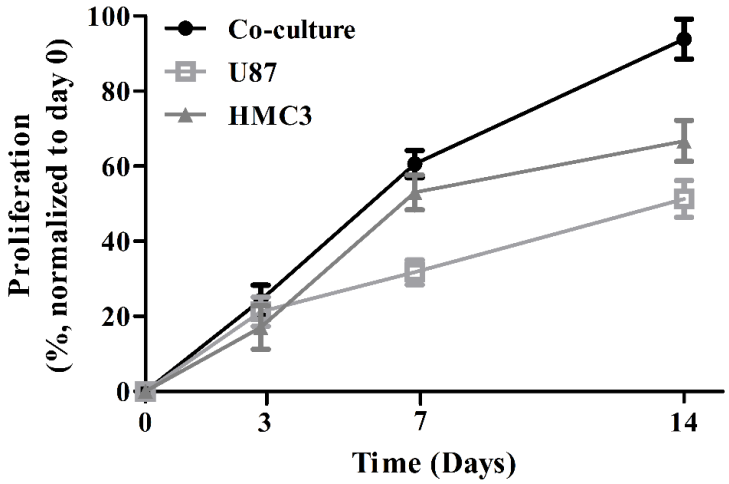

Figure 34 Cell proliferation within the printed constructs was assessed using the Alamar Blue assay, which indicated increasing metabolic activity over time.

4.2.5 Immunofluorescence staining for proliferation marker in mono- and co-cultures

In order to examine the cell proliferation within the 1H3D hydrogel system, U87, HMC3, and their co-cultures were analyzed via immunofluorescence staining for proliferation marker Ki67 (Figure 35). The expresion of Ki67 in both U87 and HMC3 cells confirmed the proliferative capacity of the cells in the hydrogel (Figure 35A). Notably, the co-cultured cells displayed significantly greater Ki67 expression compared to single-cell cultures (Figure 35B), suggesting that the interaction between glioblastoma and microglial cells fosters a more proliferative microenvironment.

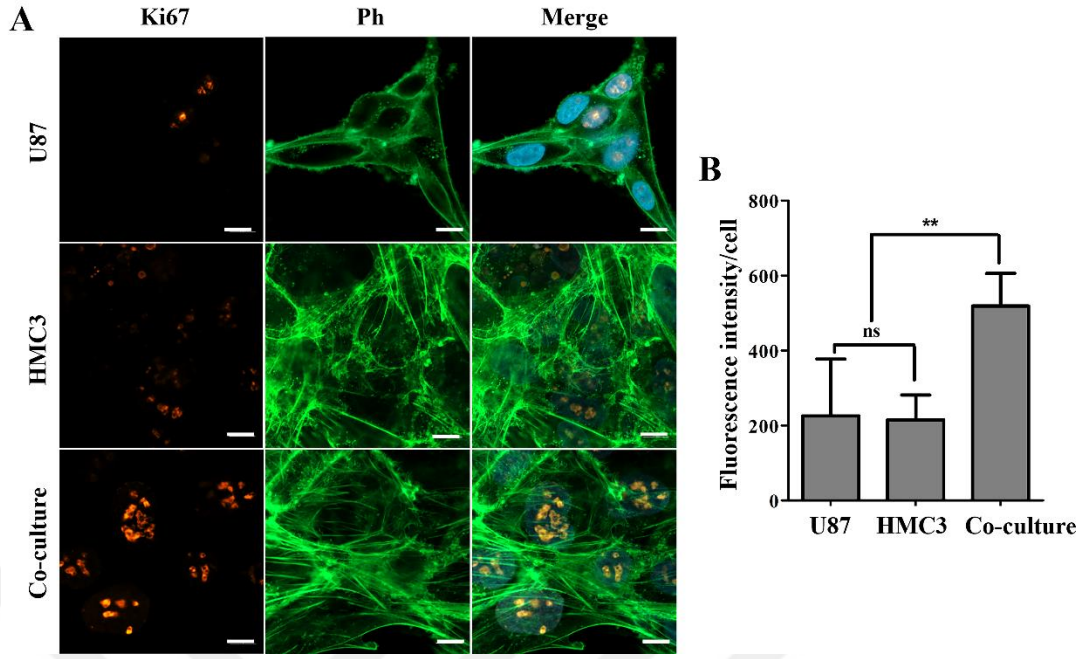

Figure 35 Ki67 expression of the cells. (A) CLSM images of immunofluorescence staining of U87, HMC3, and co-culture cells for the expression of proliferation marker Ki67. (Green: F-actin, phalloidin, red: Ki67, blue: nucleus, DAPI). Scale bar: 20 µm. (B) The graph of fluorescence intensities per cell.

4.3 Production and Characterization of the Hypoxia Chip

The PDMS chips were fabricated using negative mold, cleaned, and bonded to glass slides by applying a thin layer of uncured PDMS around the chip periphery, followed by incubation at 100°C to achieve complete bonding (Figure 36). The medium was administered from the reservoirs, and no leakage was observed, with flow efficiently maintained through the side channels of the chip.

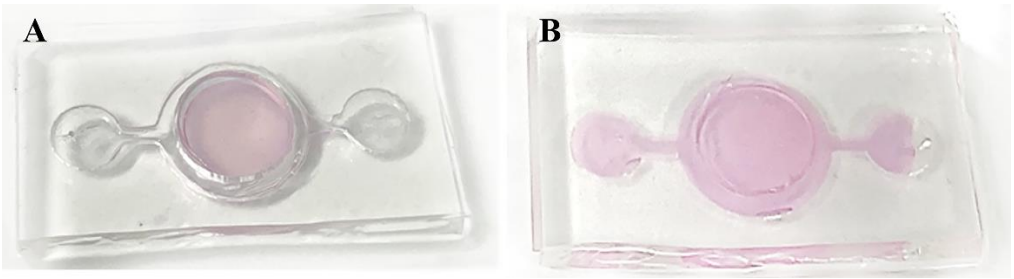

Figure 36 The hypoxia chip. (A) 3D printed structure was placed at the center of the chip, then covered by a top glass slide. (B) Medium was added via the reservoirs, allowing it to flow through the channels of the chip.

4.3.1 Testing of the hypoxia model via fluorescence staining of hypoxic cells

Image-iT Hypoxia Reagent stains hypoxic cells green, with fluorescence intensity increasing proportionally to the level of hypoxia. In the hypoxia chip, a glass slide was placed onto the cell loaded hydrogels, serving as an O_2 diffusion barrier that blocked the gas exchange from the atmosphere. O_2 diffusion was facilitated only from the lateral side of the gas permeable PDMS chip. This configuration was designed to create an oxygen gradient from the periphery toward the core, thereby increasing hypoxia at the central region. The results indicated that when cell loaded hydrogels were placed inside the PDMS chip containing a glass barrier, cells located at the core exhibited strong hypoxic conditions, as evidenced by intense green fluorescence staining (Figure 37F, H). In contrast, cells positioned at the hydrogel periphery displayed significantly reduced fluorescence intensity, which gradually increased toward the core, clearly establishing a hypoxic gradient (Figure 37B, G). Additionally, when cell loaded hydrogels were placed in the chip under similar conditions but without the glass barrier, the fluorescence intensity of the cells was significantly reduced (Figure 37C-E), resembling the intensity levels observed in peripheral cells of the hypoxia chip. These findings indicate that the glass barrier placed on top of the hydrogel effectively prevented atmospheric O_2 diffusion, creating a hypoxic environment that increased from the periphery to the center due to lateral gas diffusion (Figure 37B). The consistent observation of lower fluorescence intensity in the x-z direction at both the periphery and in control samples further confirmed that the hypoxic environment was primarily due to the glass barrier, rather than the thickness of the hydrogel itself.

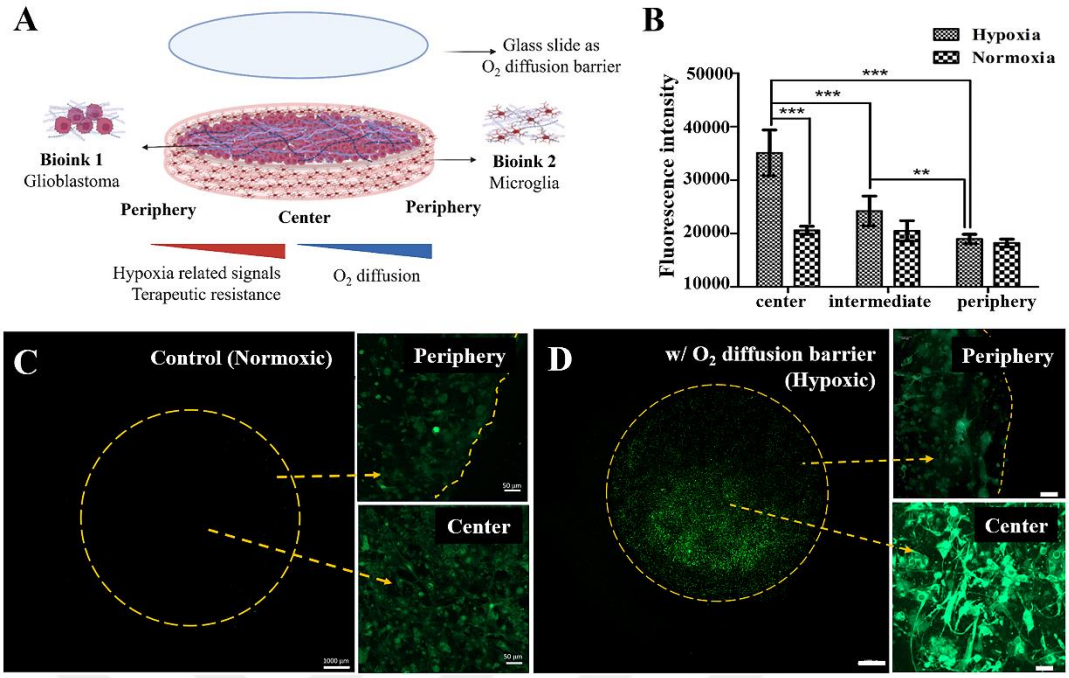

Figure 37 The cells in the PDMS chip. (A) Schematic illustration of hypoxia induction. (B) Mean fluorescence intensity of the cells located at the periphery, intermediate, and center regions of the PDMS chip under hypoxic and normoxic conditions. Fluorescence images of the cells in the chip (C) without the top glass slide, serving as the control (normoxia), and (D) with the top glass slide, serving as an O_2 diffusion barrier to induce hypoxia, stained with Image-iT Green Hypoxia Reagent. Green: hypoxic cells. Orange lines indicate hydrogel borders. Scale bars: (C, D) 1 mm.

4.3.2 SEM of cells in the hydrogel

The SEM images provided a comparison of the morphological features of the acellular 1H3D hydrogel, and the same hydrogel containing cells (U87/HMC3 co-culture) cultured in the hypoxia chip for 7 days (Figure 38). The acellular matrix showed a well organized, porous architecture with smooth internal surfaces and interconnected pores, which indicates a favorable matrix for potential cell infiltration and nutrient diffusion. In contrast, the cell loaded hydrogel exhibited distinct morphological changes, with cells visibly adhering to and spreading across the matrix. These cells formed dense networks of cellular extensions and deposited ECM-like structures, bridging across pores and interacting with the surrounding matrix. This indicates active cell-matrix interactions and suggests that cells were not only surviving but also remodeling their environment.

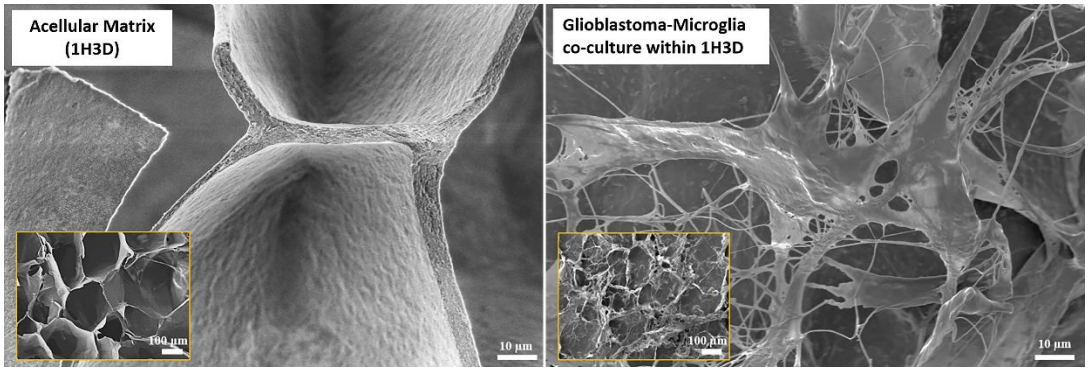

Figure 38 SEM images of the acellular 1H3D matrix (left) and the same matrix after co-culture of U87/HMC3 cells (right).

4.3.3 Staining of pseudopalisading and necrotic regions using anti-Ki67 and ethidium homodimer-1

The viability of U87/HMC3 co-culture cells in the hypoxia chip was determined on day 7 using the Live/Dead assay (Figure 39). The results showed a clear pattern of necrotic core formation in U87/HMC3 co-cultures (Figure 39A, C). At the center of the chip, most cells were dead, indicating severe hypoxia and nutrient deprivation leading to the development of a necrotic environment. This finding closely replicates the necrotic cores commonly observed in GBM tumors, where oxygen and nutrient deficiency result in extensive cell death. In contrast, the intermediate and peripheral regions of the chip predominantly contained live cells (Figure 39B, D, E). These regions likely experienced less hypoxia and better nutrient availability, supporting cell survival. This pattern aligns with a characteristic feature of GBM tumors, where viable, proliferating cells surround the necrotic core.

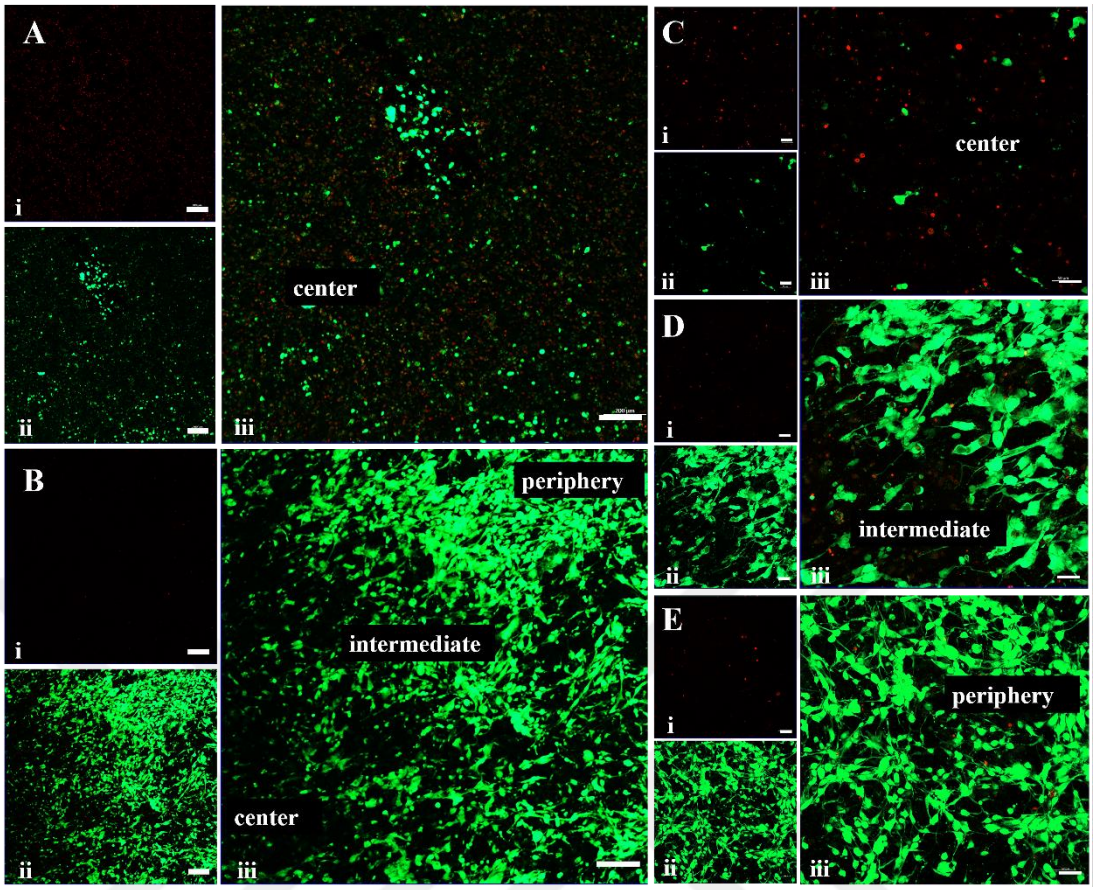

Figure 39 Live/Dead analysis of U87/HMC3 co-culture in the hypoxia chip, at (A, C) the center, (B, D) the intermediate, and (E) the periphery of the chip. (i) The dead cells (stained with ethidium homodimer-1, red), (ii) the live cells (stained with calcein AM, green) and (iii) merged. Scale bar: (A, B) 200 μm, (C-E) 50 μm.

Additionally, immunofluorescence staining for the proliferation marker Ki67 was conducted to identify hypercellular pseudopalisading regions. The results showed no detectable Ki67 expression in cells at the center of the chip (Figure 40A), where hypoxia and nutrient deprivation created a necrotic core. In contrast, Ki67 expression was strongly evident in cells located in the intermediate (Figure 40D) and peripheral (Figure 40G) regions of the chip, indicating active proliferation in these areas. These results, together with the observed viability pattern, reflect a key histopathological feature of GBM tumors, pseudopalisading necrosis.

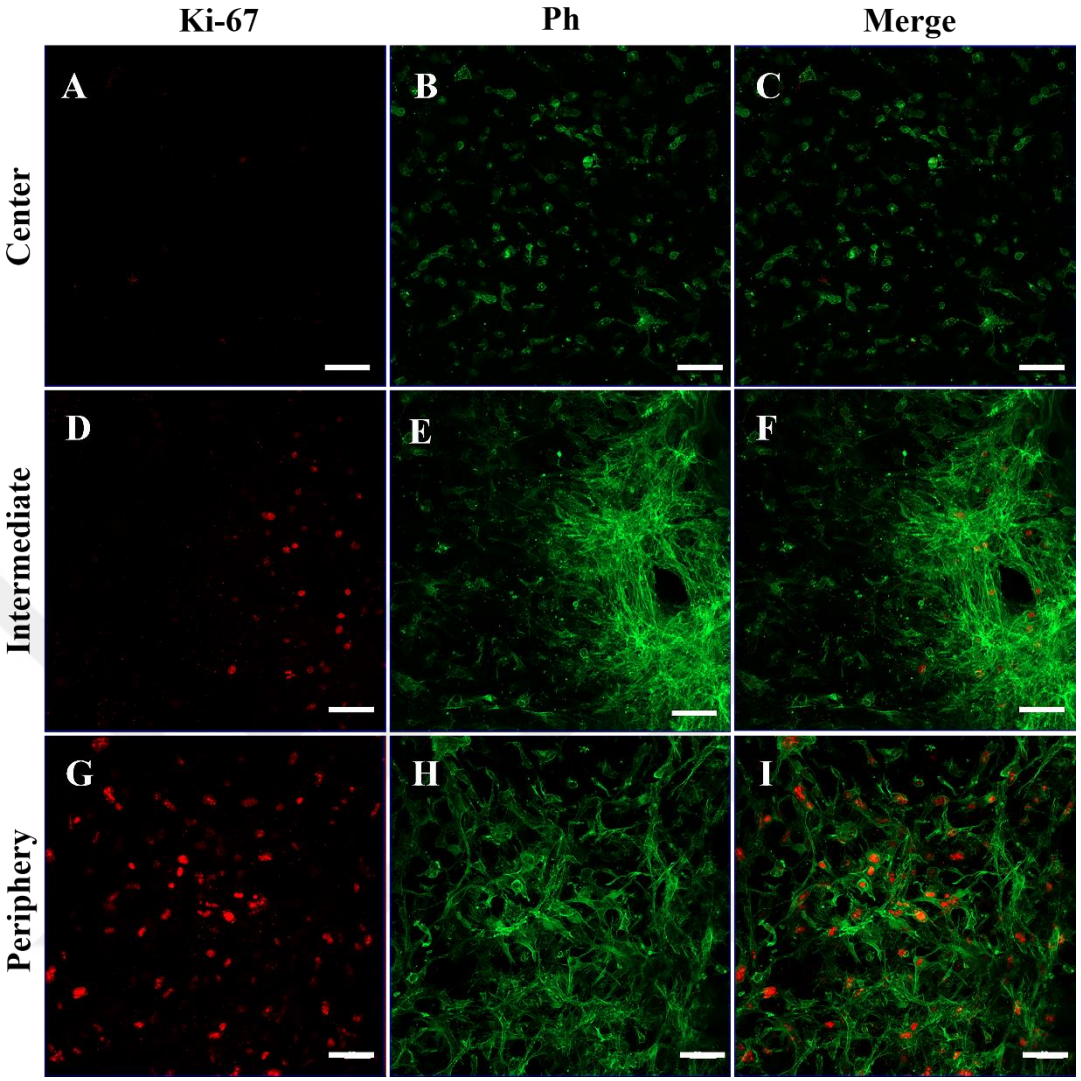

Figure 40 CLSM image of immunofluorescence staining of the cells for Ki67 in the hypoxia chip, at (A-C) the center, (D-F) the intermediate, and (G-I) the periphery of the chip. (Green: F-actin, phalloidin, red: Ki67). Scale bar: 50 μm.

4.3.4 Gene expression analysis using real-time polymerase chain reaction

Gene expression analysis was conducted to investigate how the ECM mimicking hydrogel and hypoxic conditions influence cellular adaptation and enhance the resemblance of the model to *in vivo* tumors. After 7 days of culture in the PDMS chips, RNA was extracted from cells in 3D hydrogel under both normoxic and hypoxic conditions, and from 2D monolayer cultures. Gene expression levels were normalized to GAPDH, and fold change analysis was conducted relative to monolayer cultures to quantify differences in molecular responses. At the end of the RT-PCR assay, melting

curve analysis was carried out to examine the specificity of the reactions, and they produced single peaks, indicating the amplification of specific target sequences without nonspecific products or primer dimer formation (Appendix 5). The results indicated that Ki67 and EGFR, which are critical regulators of cell growth and survival, showed significantly higher expression in the PDMS chips under normoxic conditions compared to monolayer culture, which was further upregulated in hypoxia (Figure 41B). CHI3L1 showed significantly higher expression in PDMS chip under normoxic conditions compared to monolayer culture, which was also upregulated in hypoxia. HIF1A, SOX2, and NES, which regulate stemness and therapy resistance, showed only minor changes in 3D cultures under normoxic conditions, but their expression increased significantly under hypoxia (Figure 41C). Additionally, GFAP expression decreased in both normoxia and hypoxia compared to monolayer culture, indicating a shift from astrocytic differentiation towards a more mesenchymal-like state, characteristic of high grade gliomas (159).

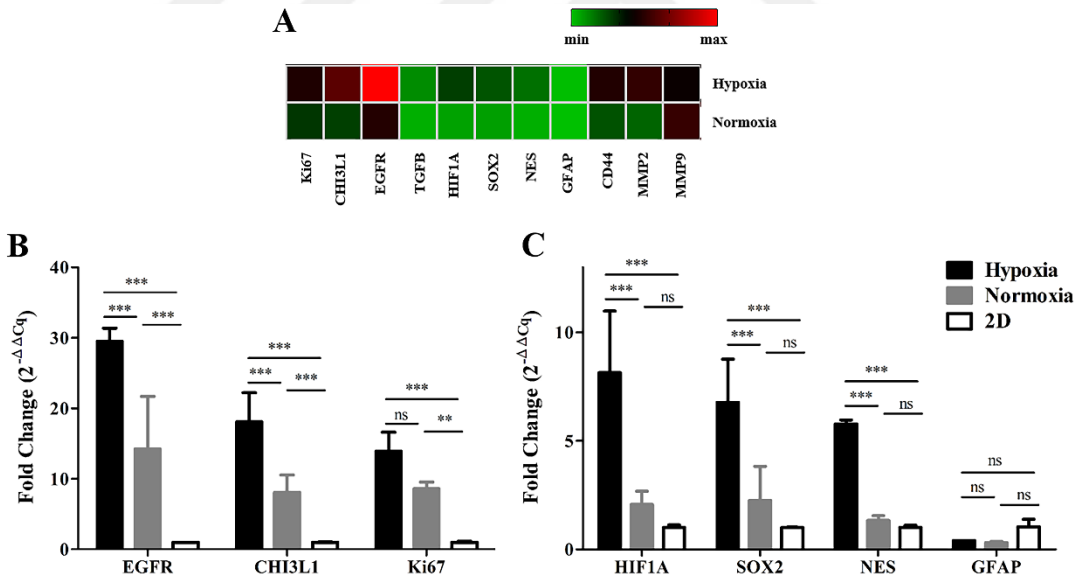

Figure 41 Gene expression analysis of the cells cultured in PDMS chips under normoxic and hypoxic conditions. (A) Heatmap representation of gene expression changes. Quantification of (B) growth, proliferation, and tumor development-related genes: EGFR, CHI3L1, and Ki67, (C) hypoxia, stemness, and therapy resistance-related genes: HIF1A, SOX2, NES, and GFAP. Gene expression levels were shown as fold change ($2^{-\Delta\Delta Cq}$) normalized to 2D monolayer cultures.

4.3.5 Proteomic profiling under normoxic and hypoxic conditions

In order to investigate pathways involved in hypoxia induced adaptations, label-free quantitative proteomic profiling was conducted to compare normoxic and hypoxic conditions. Heatmap clustering (Figure 42A) demonstrated clear separation between normoxic and hypoxic samples, indicating consistent proteomic changes in response to hypoxia. Volcano plot analysis (Figure 42B) identified a subset of proteins significantly upregulated under hypoxia. KEGG pathway enrichment (Figure 42D) revealed activation of glycolysis/gluconeogenesis, carbon metabolism, amino acid biosynthesis, mineral absorption, HIF-1 signaling, actin cytoskeleton regulation, and tight junction pathways. Protein-protein interaction (PPI) analysis of significantly upregulated proteins (Figure 42C) showed a highly connected glycolysis module, including LDHAL6B, TPI1, PKLR, PGK1, GPI, and ENO1, which are associated with metabolic reprogramming in glioblastoma, supporting anaerobic glycolysis and adaptation to hypoxic environment (160-162). These proteomic findings are consistent with observed phenotypic and transcriptional changes in the model. Enrichment of the HIF-1 signaling pathway suggests activation of hypoxia responsive transcriptional programs driving metabolic and structural remodeling (163, 164). Upregulation of cytoskeletal regulation and tight junction pathways may facilitate enhanced invasion and altered cell-cell interactions (165), while activation of biosynthetic processes reflects metabolic flexibility under low oxygen conditions (166). Collectively, the data indicates that the hypoxia chip platform captures key features of metabolic and microenvironmental adaptation relevant to glioblastoma biology.

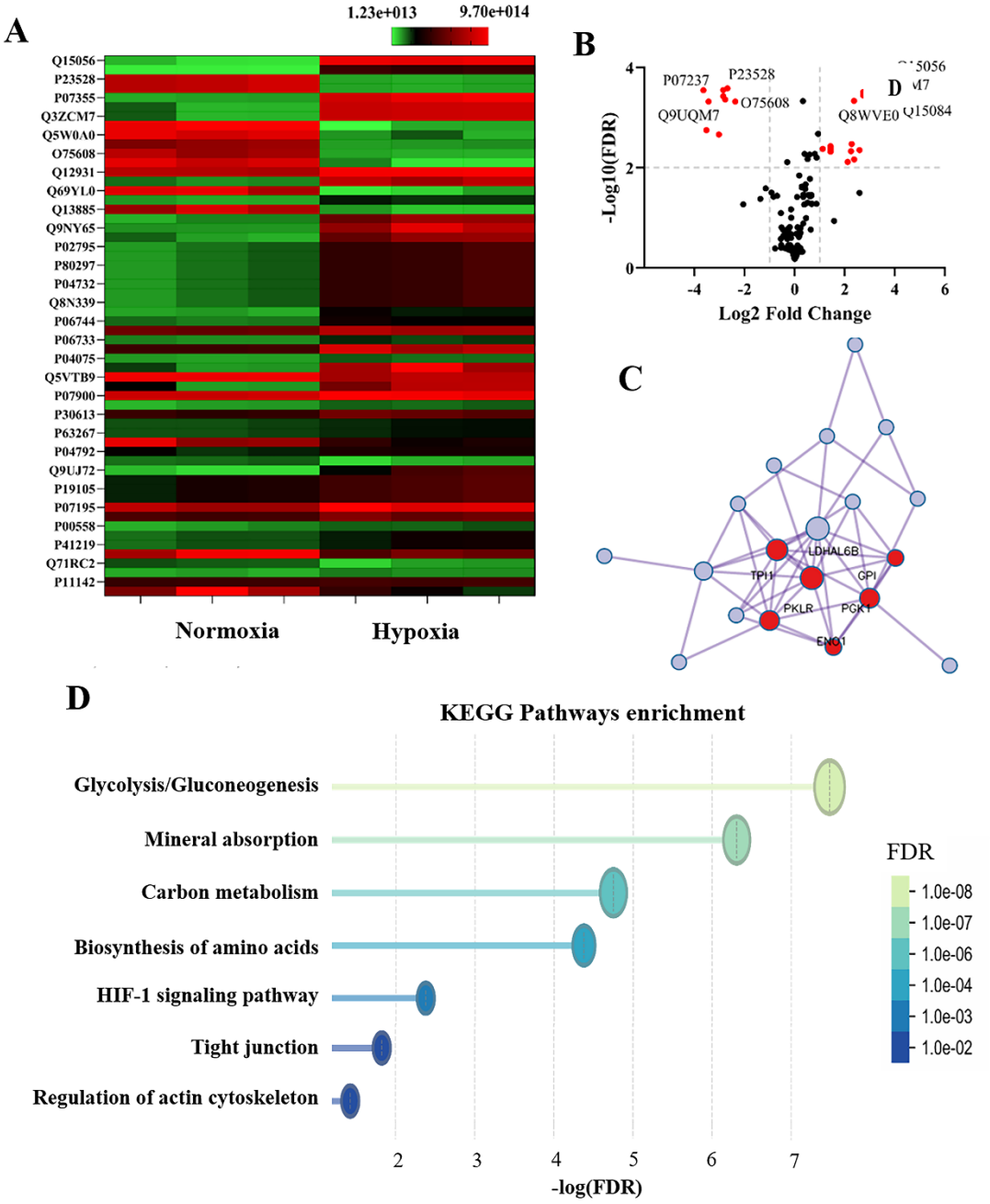

Figure 42 Proteomic characterization of the hypoxia chip model. (A) Heatmap illustrating the relative abundance of proteins that exhibited significant differences between normoxic and hypoxic conditions. (B) Volcano plot representing proteins with statistically significant expression changes (red: fold change ≥ 1.5 and $p < 0.05$). (C) Protein-protein interaction (PPI) network of significantly upregulated proteins generated using Metascape; a glycolysis-related cluster is highlighted in red. (D) KEGG pathway enrichment of upregulated proteins, performed using the STRING database.

4.3.6 Immunofluorescence staining of differentiation marker under normoxic and hypoxic conditions

In order to determine the differentiation status of U87 cells in both mono- and co-culture, and under normoxic and hypoxic conditions, immunofluorescence staining was conducted with the glial marker GFAP (Figure 43). In co-culture with microglia, GFAP expression was significantly reduced compared to monoculture, suggesting that the presence of microglia inhibits differentiation in glioblastoma cells. This effect was even stronger under hypoxic conditions, where GFAP levels decreased further. The combined impact of microglia interaction and hypoxia promotes a less differentiated, potentially more stem-like, and aggressive tumor phenotype.

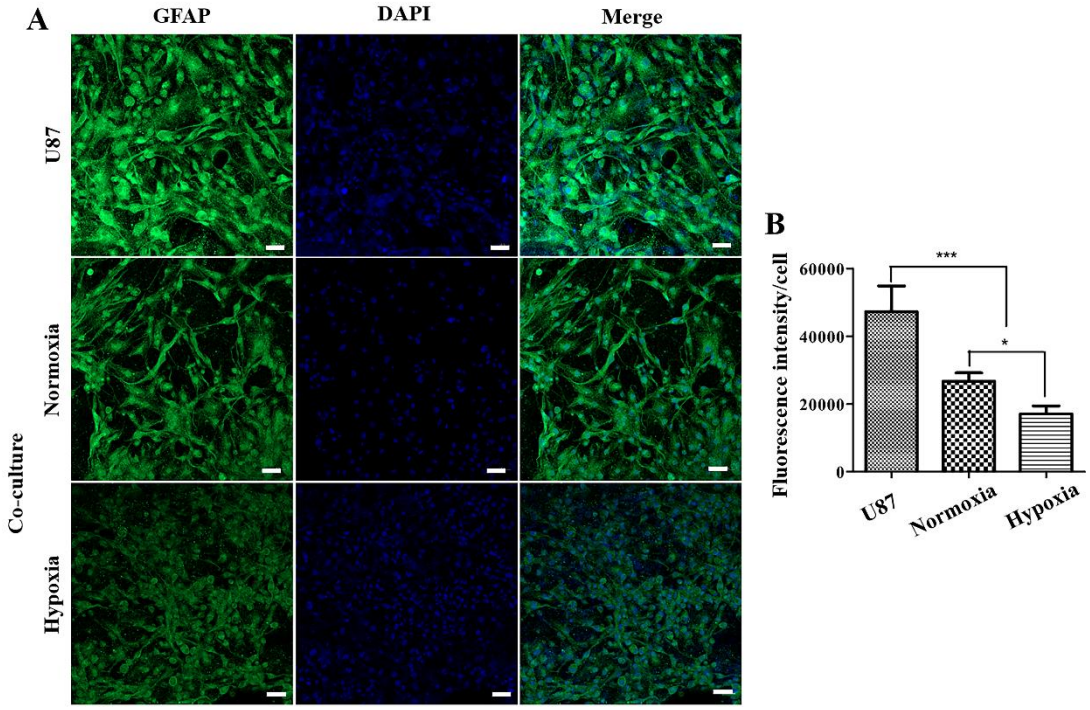

Figure 43 Immunofluorescence staining for GFAP. (A) CLSM images of the cells under normoxic and hypoxic conditions. Scale bar: 50 µm. (B) Graph shows relative fluorescence intensities.

4.3.7 Invasion of glioblastoma cells under normoxic and hypoxic conditions

Invasive behavior of glioblastoma cells under normoxic and hypoxic conditions was examined by invasion assay with spheroids of EGFP-U87/HMC3 cells. The

spheroids were embedded in 1H3D hydrogel solutions fabricated using 3D printing and subsequently crosslinked under UV light (365 nm). After crosslinking, the constructs were placed into PDMS chips. Images were obtained on days 0, 1, 2, 3, and 5 using CLSM, the migration distances of glioblastoma cells invading from the spheroid periphery were quantified to analyze their invasion capacity in both hypoxic and normoxic conditions (Figure 44). The results revealed distinct differences in glioblastoma cell behavior under normoxic and hypoxic conditions, with invasion progressively increasing over time (Figure 44A, B). In the early phases, spheroids in both conditions were compact, with minimal outward cell movement. However, spheroids under hypoxia exhibited early signs of cell migration, with cellular extensions invading the surrounding matrix. Over time, the differences between the two conditions became more pronounced. Spheroids exposed to hypoxia showed significantly greater cell migration compared to those under normoxia. These observations were further supported by molecular analyses, which showed a marked upregulation of MMP2, CD44, and TGF-β expression under hypoxic conditions (Figure 44C). These findings suggest that hypoxia promotes GBM invasion by enhancing cell migration and extracellular matrix degradation (148, 167).

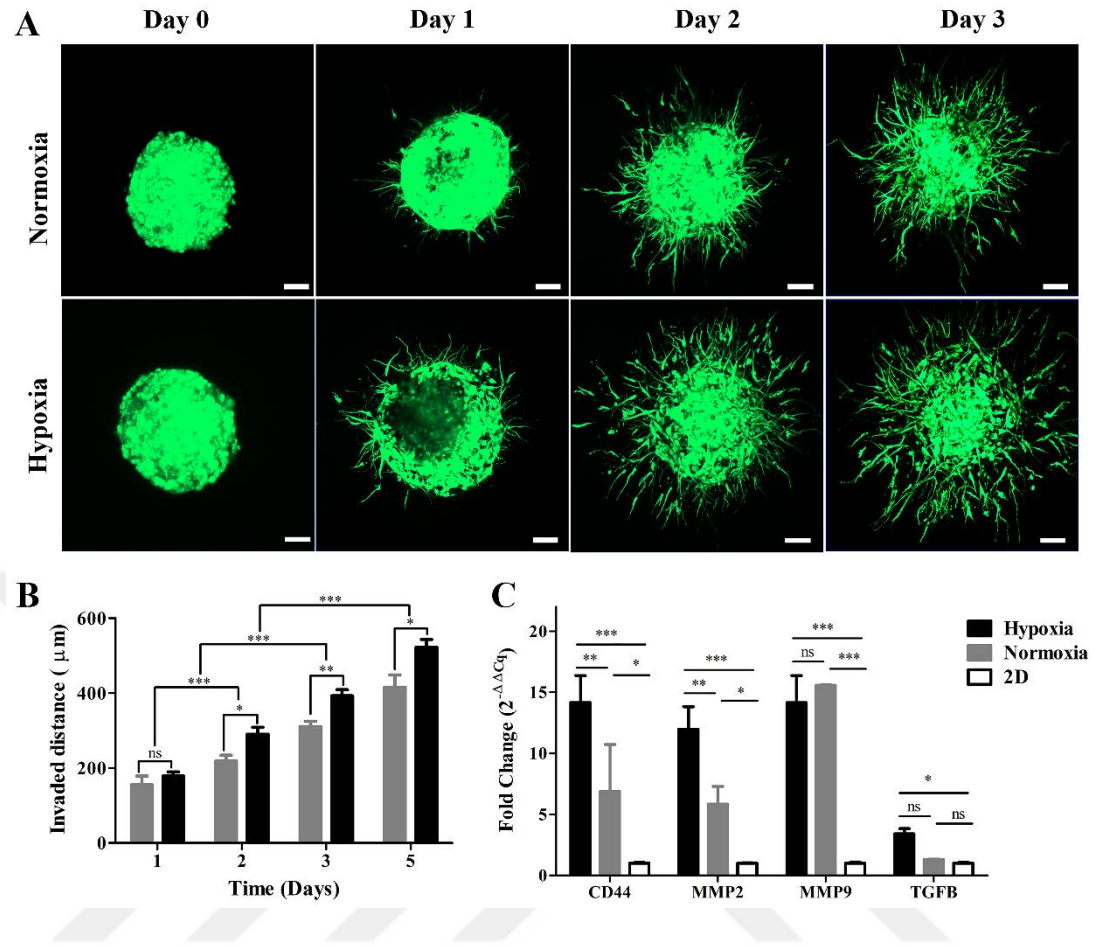

Figure 44 Glioblastoma invasion in the PDMS chip. (A) CLSM images showing the invasion of glioblastoma cells over time. Scale bar: 100 µm (B) Quantitative analysis of invasion distances measured over a 5 day period. (C) Relative expression levels of invasion associated genes, expressed as fold changes ($2^{-\Delta\Delta Cq}$) compared to 2D monolayer cultures.

4.3.8 Visualization of nutrients and drug flow

The diffusion of fluorescein molecules (Mw ~0.4 kDa) through the 3D hydrogel within the PDMS chip was examined over time to simulate the transport behavior of low molecular weight drugs such as temozolomide (TMZ) (Figure 45). The analysis through imaging and fluorescence intensity quantification showed a clear time dependent diffusion pattern. At the initial time point (0 h), no fluorescence signal was observed within the hydrogel. However, by 1 h, the fluorescein signal became visible at the periphery of the hydrogel (Figure 45A), indicating that diffusion occurs in an outward-to-inward direction, with molecules migrating from the edges toward the

core. By 24 h, the fluorescence signal was uniformly distributed throughout the hydrogel, suggesting that the diffusion process had reached equilibrium.

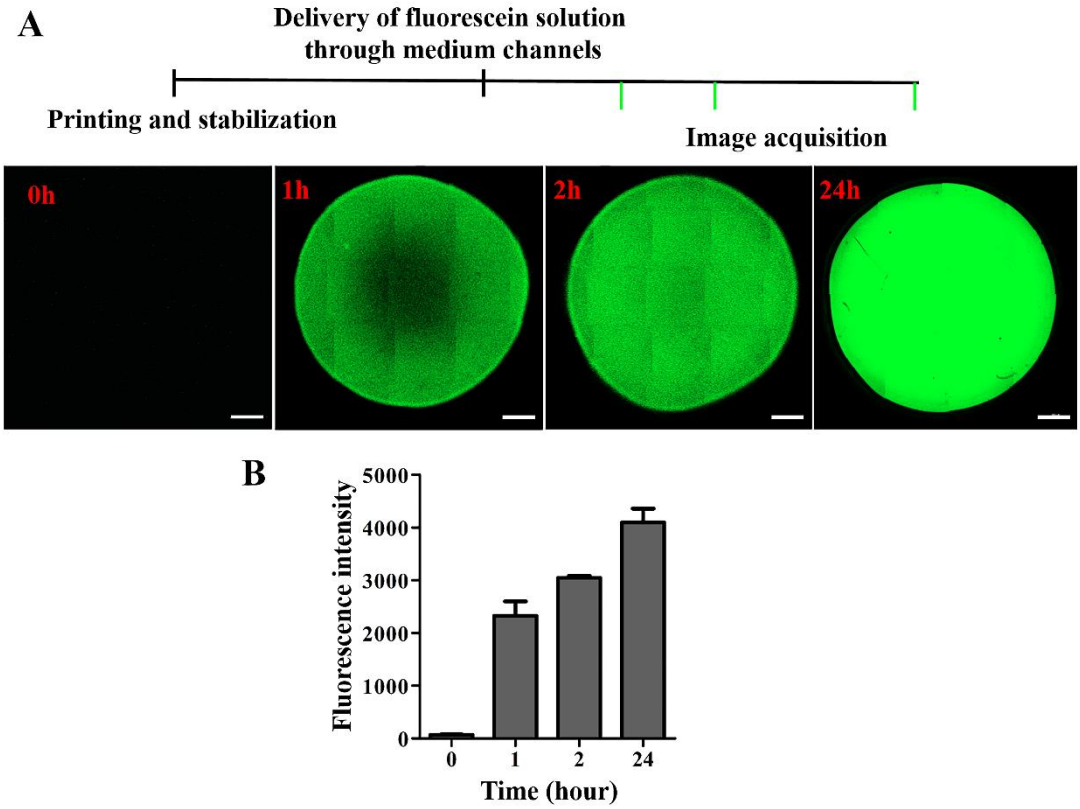

Figure 45 Visualization of nutrient flow. (A) Fluorescence images showing the progressive diffusion of fluorescein dye throughout the hydrogel matrix. Scale bar: 1 mm. (B) Quantitative analysis of fluorescein diffusion, presented as average fluorescence intensity over time within the hydrogel construct.

4.3.9 Testing of the model with temozolomide drug treatment

The concentration range of TMZ was determined by applying increasing concentrations of TMZ and examining the cellular response using the Live/Dead assay. The results indicated that while most cells remained viable (green, Calcein AM) in the control group (Figure 46A), whereas TMZ treatment resulted in a dose dependent reduction in cell viability (Figure 46B–D). At a concentration of 5 mM TMZ, no viable cells were detected. Due to the low magnification used, dead cells (red, EtHd-1) were not visible.

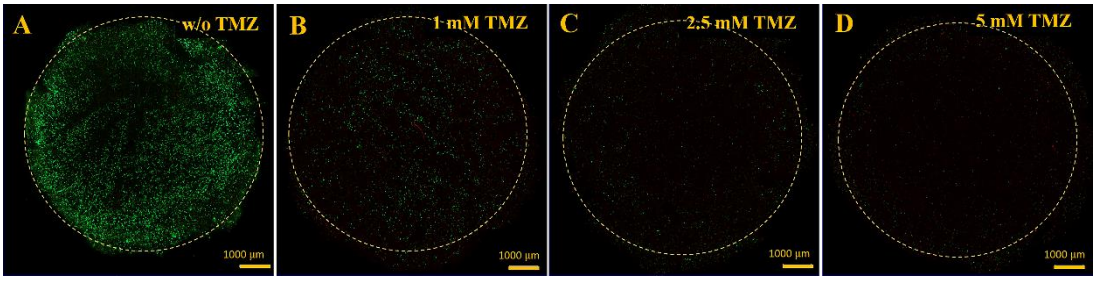

Figure 46 Live/Dead analysis of U87/HMC3 cells in the PDMS chip with O_2 diffusion barrier (hypoxia), following drug treatment with temozolomide (1, 2.5, 5 mM). (A) without, (B) 1 mM, (C) 2.5 mM, and (D) 5 mM TMZ. The dead cells (stained with ethidium homodimer-1, red), and the live cells (stained with calcein AM, green). Scale bar: 1000 µm.

The *in vitro* model was validated by determining the response of the cells to TMZ and obtaining the IC_{50} value. Cells were maintained in the hypoxia chips for 7 days, after which the medium was replaced with fresh medium containing TMZ at varying concentrations (0–5000 µM). Cellular responses to TMZ were determined using the Alamar Blue viability assay. Based on the cytotoxic response to TMZ concentrations, a graph was plotted to calculate the IC_{50} (Figure 47). As controls, IC_{50} calculations were also performed for cells in 2D monolayer cultures and in the hydrogel under normoxic conditions. In 2D monolayer cultures, the IC_{50} value for the U87/HMC3 co-culture was calculated as 509 ± 58 µM. The IC_{50} values were calculated as 1120 ± 71 µM for normoxic conditions and 1699 ± 134 µM for hypoxic conditions in the chip (Table 7). The higher IC_{50} values observed in hydrogels compared to monolayer cultures, and in the hypoxia chip compared to normoxia, indicate reduced TMZ sensitivity in 3D and hypoxic microenvironments.

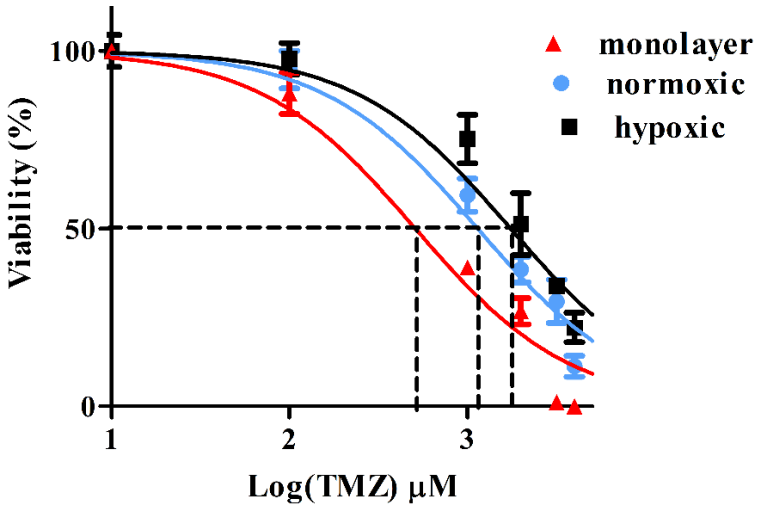

Figure 47 Dose-response curve of cells treated with TMZ under different culture conditions.

Table 7 The IC_{50} values for TMZ

Conditions	**IC_{50} (µM)**
monolayer	509
normoxic	1120
hypoxic	1699

5 DISCUSSION

GBM is the most aggressive primary brain tumor in adults, characterized by rapid proliferation, infiltrating the surrounding healthy brain tissue, and resistance to conventional treatment approaches. One of the main contributors to this resistance is the complex and heterogeneous TME, consisting of a dense extracellular matrix, diverse cellular populations, and hypoxic regions. In order to gain deeper insight into the pathophysiology of GBM and to support the development of more effective therapeutic approaches, there is a growing need for advanced *in vitro* models. This study addresses this by providing a biologically relevant platform that mimic certain features of the GBM microenvironment. The development and integration of a hydrogel based ECM mimic with a PDMS based hypoxia chip enabled the study of the biochemical, mechanical, and pathological characteristics of the glioblastoma TME. The platform is designed as a physiologically relevant tool for understanding tumor behavior and assessing the therapeutic response of potential drug candidates.

dECM1 was selected over dECM2 as the preferred brain tissue decellularization method based on its greater decellularization efficiency, more effective removal of cellular material, and better preservation of native biochemical content. The residual DNA content in dECM1 was 39.0 ± 10 ng/mg, below the accepted threshold of 50 ng/mg, while dECM2 did not achieved this criterion. Furthermore, dECM1 retained higher levels of sGAGs and proteins, enhancing the biochemical relevance of the resultant matrix. In terms of cellular compatibility, dECM1 demonstrated superior performance, supporting over 90% viability of glioblastoma cells. Cells attached to the dECM matrix exhibited elongated, branched morphologies and formed organized clusters and cellular networks, supporting the suitability of the material.

In order to provide biochemical relevance with mechanical strength and mimic the stiffness of glioblastoma tissue, decellularized brain ECM was combined with hyaluronic acid methacrylate. The HAMA/dECM composite hydrogel provided a mechanically stable, yet flexible matrix, matching the biomechanical properties of high grade gliomas (168, 169). Previous studies have shown that glioblastoma tissues

are significantly stiffer than healthy brain tissues (170-172). While the compressive modulus of healthy brain tissues is approximately 1 kPa (63, 64), high grade gliomas exhibit values around 11.4 ± 4.9 kPa (65). This increased stiffness is attributed to both tumor cells themselves and the surrounding ECM, which together contribute to the physical remodeling of the glioblastoma microenvironment. Changes in tissue mechanics have been linked to impaired vascular and lymphatic function, induction of hypoxia, and promotion of immune evasion, underscoring the significant role of ECM stiffness during glioblastoma progression. In this study, the 1H3D hydrogel achieved a compressive modulus of 9.44 ± 0.73 kPa, closely matching the glioblastoma stiffness. Moreover, glioblastoma tumors exhibit viscoelastic properties, a combination of solid-like and fluid-like behaviors (173). The elastic (G′) and viscous (G″) moduli of GBM tissue have been reported within the ranges of 300-1200 and 20-120 Pa, respectively (174, 175). Notably, the 1H3D hydrogel had an elastic modulus of 458.30 ± 13.39 Pa and a viscous modulus of 65.17 ± 6.46 Pa, falling within the range of glioblastoma tissue and indicating its suitability as a biomimetic platform. Unlike traditional 2D monolayer cultures, which fail to replicate the 3D architecture, ECM stiffness, or spatial heterogeneity of the *in vivo* tumor microenvironment (176), the composite hydrogel offers a more physiologically relevant *in vitro* platform. In contrast to standard synthetic or single component hydrogels, the composite system is both mechanically tunable and biochemically complex, closely resembling native GBM stroma. This is especially important since both biochemical and biomechanical signals influence tumor progression, therapeutic response, and resistance mechanisms (177, 178). Though several hydrogel based systems, including those based on collagen, Matrigel, or hyaluronic acid alone, have been utilized in GBM modeling, they often lack important native ECM proteins, glycosaminoglycans, and degradation products known to regulate invasion, drug resistance, and stem like cell behavior. In contrast, the composite model combines HAMA with decellularized brain ECM, providing both biochemical complexity and tissue specificity. Despite the interspecies origin of bovine derived dECM, the composite hydrogel maintains key biochemical features and thus offers greater physiological relevance compared to simplified matrices used in prior models.

Brain tissue contains one of the highest water content in the body, approximately 80%, and glioblastoma tissue has been reported to contain even higher water content, reaching up to 84.5% (179, 180). The highly hydrated microenvironment is mainly caused by the increased permeability of the blood-brain barrier, contributing to vasogenic edema, abnormal vascular development, and the upregulation of water transport channels such as aquaporin-4 (AQP4) (181). The composite hydrogels demonstrated water contents up to 95.5%, closely mimicking water retention characteristics of GBM tissue, therefore representing a suitable matrix for tumor modeling applications. In addition to water content, the degradation profile is also another important functional property of hydrogels. Hydrogels that degrade more quickly can release cytokines, growth factors, and other signaling cues more rapidly, however, they often lack sufficient structural integrity (182, 183). In this study, the results demonstrated that different formulations exhibited differences in degradation behavior, as HAMA based hydrogels degraded more slowly than dECM based hydrogels. This is consistent with earlier findings suggesting that dECM hydrogels tend to degrade more rapidly because their noncovalent crosslinks limit their structural stability compared to covalently crosslinked systems (184). Upon decellularization and enzymatic digestion, dECM form a hydrogel at physiological temperature (37°C) and neutral pH (7.4), where hydrogen bonding, hydrophobic interactions, and electrostatic forces maintain its structure. Even though these interactions enable the gelation process, they are not enough for providing long term structural strength (185). Conversely, upon polymerization, HAMA forms covalent crosslinks between methacrylate groups, resulting in a more robust and stable network, where covalent bonds provide superior stability to the noncovalent interactions present in dECM hydrogels (186). While dECM improves the biocompatibility and imposes the biochemical complexity of native ECM, HAMA provides structural stability and mechanical strength to the composite hydrogel.

The interaction between stroma and GBM was simulated using co-culture with microglia. Co-cultures of glioblastoma and microglia presented significantly increased Ki67 expression and cellular invasion compared to monocultures, indicating the tumor promoting effect of microglia. The effects likely result from a complex synergistic

interaction between glioblastoma and microglia. Microglia are considered one of the key modulators of glioblastoma progression, and this role is largely mediated by the release of various protumorigenic cytokines, growth factors and other signaling molecules that contribute to proliferation, invasion, and survival of the tumor cells (187). They also undergo phenotypic reprogramming within the GBM microenvironment, adopting a protumorigenic phenotype (188). These observations are consistent with previous studies and emphasize the importance of bidirectional communication with stromal components in driving tumor progression (189, 190). Furthermore, application of 3D bioprinting to create compartmentalized co-cultures enabled controlled organization of glioblastoma and microglia cells, facilitating a more precise imitation of the immunosuppressive tumor microenvironment. This approach enables various cell populations to be arranged within specified areas, supporting targeted analysis of interactions between tumor and stroma. Though organoid models have gained interest for their ability to mimic tumor heterogeneity and self-organization (191, 192), they are usually constrained by batch-to-batch inconsistency and limited control over cell positioning and ECM composition. These limitations restrict their use in high throughput screens for drugs and mechanistic studies. On the other hand, the application of the bioprinting technique enabled greater structural control and reproducibility, offering a more controllable platform for the study of intercellular communication in the glioblastoma microenvironment.

PDMS based hypoxia chip designed in this study successfully replicated key characteristics of glioblastoma microenvironment and allowed for the investigation of hypoxia induced cellular behaviors. A glass diffusion barrier was employed to create a steady gradient of oxygen across the construct, yielding hypoxic areas. Image-iT hypoxia staining confirmed these gradients, demonstrating increased fluorescence intensity toward the center of the chip compared to the periphery, typical of the oxygen distribution found in GBM tumors. Notably, this platform created physiologically relevant hypoxia without the need for complex equipment or chemical agents, offering both practical and biological benefits over existing hypoxia generating systems. Conventional hypoxia chambers or incubators, while widely employed, subject all cells to uniform oxygen levels, without capturing the inherent oxygen heterogeneity

of the GBM tumors (13). Enzymatic systems, including glucose oxidase or catalase based ones, are able to create localized hypoxia but are limited by toxicity resulting from the byproduct accumulation (16). In contrast, the system in this study avoids these limitations by restricting oxygen diffusion passively via a glass slide on top of the hydrogel. Compared to microfluidic based hypoxia models, which allow accurate temporal control of oxygen levels and integration of vessel like flows (14, 15), the presented system is simpler, more accessible, easily scalable, and requires no external pumps or gas controls. The passive hypoxia chip presented balances physiological relevance with operationally simple handling, facilitating the integration of bioprinted, multicellular, multilayered construct within a controlled environment. Earlier studies that employed diffusion barriers, such as PMMA (17), glass slide (193), and PC (18), have successfully established hypoxic conditions; however, they present certain limitations. Oh et al. (2022) developed a passive hypoxia model using a closed system in which oxygen diffused laterally from channels into a central region (18). While this design generated oxygen gradients, it structurally confined cells within enclosed compartments, limiting direct accessibility, sampling, and integration with advanced biofabrication techniques. In contrast, the model presented in this study employs an open configuration, where a simple glass slide is placed over the hydrogel to prevent vertical gas diffusion, enabling the integration with bioprinting, supports cell patterning, and offers flexibility for advanced experimental designs. Yi et al. (2019) also employed a glass diffusion barrier to form a hypoxic core with a proliferative periphery (193). However, one critical limitation of this model is the use of decellularized ECM lacking biochemical characterization or tunable mechanical properties. In contrast, in this study, brain derived dECM was combined with hyaluronic acid methacrylate to achieve biomimetic stiffness and ECM composition, which are crucial for controlling glioblastoma cell behavior. Additionally, while the previous model lacked immune components, our platform includes microglia within a compartmentalized system, enabling the investigation of tumor-immune interactions under hypoxic conditions. Hypoxia is known to drive microglial polarization toward an M2-like state, which supports immune evasion and resistance to immunotherapy. The inclusion of microglia into a hypoxic GBM model permits studies on how hypoxia

affects immune cell behavior and shapes the development of immunosuppressive niches that drive T cell dysfunction and resistance to immune checkpoint inhibitors.

GBM exhibits high proliferative capacity and therapeutic resistance. In order to investigate the potential of the *in vitro* model to replicate GBM characteristics, key markers related to proliferation, invasion, stemness, and therapeutic resistance were studied. The results showed upregulation of Ki67, EGFR, and CHI3L1 genes under 3D normoxic conditions compared to 2D monolayers, with further upregulation under hypoxic conditions, suggesting enhanced tumor like behaviors. EGFR signaling is central to glioblastoma progression, especially under hypoxic conditions, promoting cell survival and therapeutic resistance (147, 194). The upregulation of Ki67 and EGFR under 3D normoxia and hypoxia also reflects the hyperproliferative nature of high grade glioblastomas, with EGFR amplification recognized as a driver of aggressive growth (195). CHI3L1 has been shown to facilitate GBM progression, invasive behavior, and immune escape mechanisms. It also contributes to extracellular matrix remodeling, proliferation, and therapeutic resistance (196-198). The observed gene expression profiles indicate that the model, especially under hypoxic conditions, more accurately represents key features of high grade gliomas compared to typical 2D models. Furthermore, HIF1α, SOX2, and NES genes, key regulators of stemness and therapeutic resistance, were minimally expressed under normoxia but significantly upregulated under hypoxic conditions, suggesting that hypoxia is the key factor driving stem like mechanisms (199-201). On the other hand, GFAP expression was suppressed under both normoxic and hypoxic conditions compared to the monolayer culture, indicating a transition from astrocytic differentiation to a mesenchymal-like cell state, characteristic of high grade gliomas (159). Immunofluorescence staining also confirmed this observation, revealing reduced GFAP levels under hypoxic conditions, suggesting a less differentiated, more stem-like, and potentially more aggressive cancer cell phenotype. These results indicate that the hydrogel model more accurately replicates aspects of high grade glioblastoma than 2D cultures, particularly in terms of tumor proliferation and invasion. Nevertheless, hypoxia plays a critical role in inducing plasticity, highlighting the necessity of both ECM mimicking hydrogels and hypoxic conditions for effective glioblastoma modeling.

In glioblastoma, the central regions of tumors often become necrotic as a result of severe hypoxia and restricted nutrient supply, leading to extensive cell death. Surrounding these necrotic areas are hypercellular pseudopalisading zones, which are marked by intense cellular proliferation and directed migration. This organization is facilitated by cellular signaling driven by hypoxia and nutrient gradients, promoting proliferative behavior and directional migration towards areas with higher oxygen and nutrient availability. The hypoxia chip used in this study mimicked structural and spatial heterogeneity of GBM, recreating a necrotic core surrounded by a rim of densely proliferating cells. Ki67 expression patterns observed in the hypoxia chip resembled the pseudopalisading zones characteristic of GBM. Together with the observed viability patterns, the findings showed that the hypoxia chip successfully reproduced the pathological feature of GBM, pseudopalisading necrosis.

Glioblastoma tumors are characterized by their highly invasive nature, where tumor cells infiltrate the surrounding healthy brain parenchyma. This aggressive infiltration limits the effectiveness of surgical resection and contributes to inevitable recurrence. The invasive behavior of GBM is regulated by both the intrinsic cellular properties and TME, including ECM and supporting stromal cells such as microglia (202). The viscoelastic characteristics and biochemical composition of hydrogels are critical for mimicking the invasive behavior of GBM cells (174). In this study, U87 glioblastoma cells exhibited limited invasion within HAMA only hydrogels. In contrast, the incorporation of dECM into the composite matrix provided biochemical cues that enhanced cell-matrix interactions and invasive capacity. These biochemical signals promoted cytoskeletal remodeling and initiated ECM degradation through activity of matrix metalloproteinase, thereby promoting the invasion of GBM cells. Moreover, the invasion distance of U87 glioblastoma cells increased substantially (41%) under co-culture with microglia within the composite hydrogel system, compared to monoculture conditions. These findings highlight the critical role of microglia in facilitating glioblastoma cell invasion, likely through the paracrine release of invasion related signals or contact dependent mechanisms that trigger glioblastoma cell migration. Furthermore, under hypoxic conditions, glioblastoma cells showed profoundly higher invasion compared to normoxia. Matrix metalloproteinases MMP2

and MMP9 play a central role in extracellular matrix remodeling, facilitating glioblastoma cell invasion. Their upregulation under hypoxic conditions suggests an adaptive response that enhances the invasive potential of tumor cells (203). CD44, a transmembrane glycoprotein, regulates cell adhesion and migration, and its expression has been correlated with poor patient outcomes in GBM. It has been shown to associate with MMP9, initiating a regulatory pathway that supports the remodeling process of the extracellular matrix, hence promoting glioblastoma cell invasion (204). The upregulation of CD44 under both 3D normoxic and hypoxic conditions is consistent with previous findings that associate elevated CD44 expression with increased glioblastoma invasiveness (205, 206). On the other hand, TGF-β, a cytokine facilitating glioblastoma progression, also showed significant upregulation under hypoxic conditions. TGF-β signaling induces epithelial-to-mesenchymal transition and reorganization of the cytoskeleton, facilitating the migration process of the tumor cells (207). The correlation between these molecular changes and the observed increase in invasion suggests that hypoxia plays a critical role in driving glioblastoma aggressiveness through the activation of signaling pathways. These findings are consistent with previous reports indicating that hypoxia induced HIF1α activation leads to increased expression of CD44, MMPs, and TGF-β, contributing to mesenchymal-like transition, enhanced invasiveness, and resistance to therapy (208-210).

The *in vitro* model system developed was also examined for the efficacy of temozolomide under both normoxia and hypoxia. Temozolomide is the first line chemotherapeutic agent used in glioblastoma treatment. However, its efficacy is highly variable across different *in vitro* models and culture conditions. In this study, 2D monolayer culture exhibited reduced IC_{50} value for TMZ (509 ± 58 μM) compared to 3D hydrogel cultures under both normoxic (1120 μM) and hypoxic (1699 ± 134 μM) conditions. These findings are consistent with existing literature, suggesting that drug penetration is limited within 3D matrices due to the denser extracellular matrix, which reduces drug diffusion and access to cells (211). Furthermore, it is known that hypoxic environments can foster a more chemoresistant glioma cell phenotype, influenced by alterations in gene expression, induction of cell quiescence, and

activation of survival pathways, further explaining the higher IC_{50} levels observed in the hypoxia group (212). Previous studies have reported considerable variability in the sensitivity of the U87 cell line to TMZ, with IC_{50} values ranging from 34.1 μM to 650.0 μM (213). These discrepancies underscore critical concerns regarding the reproducibility and clinical translatability of drug response datasets derived from standard 2D culture systems or immortalized cell lines. A significant limitation of this study is its reliance on the immortalized U87 glioblastoma and HMC3 microglia cell lines. Although widely used, these cell lines fail to accurately reflect the cellular heterogeneity and complexity of patient derived tumors, as they lack the genetic instability, phenotypic plasticity, and epigenetic diversity that characterize primary glioblastoma and tumor associated microglia.

Furthermore, while the interactions between tumors and their microenvironments are critical, they do not fully capture the systemic complexities that influence glioblastoma progression and therapeutic response. Future studies should focus on developing platforms that not only replicate the GBM TME but also model its interactions with key physiological systems, such as the immune and lymphatic compartments, vascular networks, and hepatic metabolism. Integrating system level complexity with real time biosensing and computational modeling will provide a more comprehensive understanding of GBM biology within a physiologically relevant context.

6 CONCLUSION

In this study, a bioprinted GBM model was developed to replicate the complex nature of the tumor microenvironment. By combining decellularized brain extracellular matrix with hyaluronic acid methacrylate, a bioink was formulated that closely resembled the mechanical and biochemical characteristics of the native tissue. The resulting hydrogel supported essential cellular behaviors, including adhesion, proliferation, invasion, and matrix remodeling, critical features for mimicking the aggressive and adaptive nature of glioblastoma. Co-culturing glioblastoma cells with microglia revealed a distinct protumorigenic effect, leading to a significant increase in both cell proliferation and invasive capacity. Furthermore, introducing a hypoxia gradient allowed the model to reflect hallmark pathological features of GBM such as pseudopalisading necrosis, altered gene expression profiles, and reduced sensitivity to temozolomide under hypoxic conditions. Taken together, the model demonstrated strong potential for drug screening applications by demonstrating the impact of the tumor microenvironment on therapeutic outcomes. Overall, this study represents an important step toward the development of more physiologically relevant *in vitro* GBM models, supporting the advancement of personalized treatment approaches and reducing the reliance on *in vivo* studies.

7 REFERENCES

1. Grochans S, Cybulska AM, Simińska D, Korbecki J, Kojder K, Chlubek D, et al. Epidemiology of glioblastoma multiforme–literature review. Cancers. 2022;14(10):2412.
2. Pouyan A, Ghorbanlo M, Eslami M, Jahanshahi M, Ziaei E, Salami A, et al. Glioblastoma multiforme: insights into pathogenesis, key signaling pathways, and therapeutic strategies. Molecular Cancer. 2025;24(1):58.
3. Angom RS, Nakka NMR, Bhattacharya S. Advances in glioblastoma therapy: an update on current approaches. Brain sciences. 2023;13(11):1536.
4. Stupp R, Mason WP, Van Den Bent MJ, Weller M, Fisher B, Taphoorn MJ, et al. Radiotherapy plus concomitant and adjuvant temozolomide for glioblastoma. New England journal of medicine. 2005;352(10):987-96.
5. Sharma P, Aaroe A, Liang J, Puduvalli VK. Tumor microenvironment in glioblastoma: Current and emerging concepts. Neuro-Oncology Advances. 2023;5(1):vdad009.
6. Janjua TI, Rewatkar P, Ahmed-Cox A, Saeed I, Mansfeld FM, Kulshreshtha R, et al. Frontiers in the treatment of glioblastoma: Past, present and emerging. Advanced drug delivery reviews. 2021;171:108-38.
7. Xiao W, Ehsanipour A, Sohrabi A, Seidlits SK. Hyaluronic-acid based hydrogels for 3-dimensional culture of patient-derived glioblastoma cells. Journal of Visualized Experiments: JoVE. 2018(138):58176.
8. Ananthanarayanan B, Kim Y, Kumar S. Elucidating the mechanobiology of malignant brain tumors using a brain matrix-mimetic hyaluronic acid hydrogel platform. Biomaterials. 2011;32(31):7913-23.
9. Koh I, Cha J, Park J, Choi J, Kang S-G, Kim P. The mode and dynamics of glioblastoma cell invasion into a decellularized tissue-derived extracellular matrix-based three-dimensional tumor model. Scientific reports. 2018;8(1):4608.
10. Gentilin E, D'angelo E, Agostini M, Astolfi L. Decellularized normal and cancer tissues as tools for cancer research. Cancer Gene Therapy. 2022;29(7):879-88.
11. Yi H-G, Jeong YH, Kim Y, Choi Y-J, Moon HE, Park SH, et al. A bioprinted human-glioblastoma-on-a-chip for the identification of patient-specific responses to chemoradiotherapy. Nature biomedical engineering. 2019;3(7):509-19.
12. Eke G, Mangir N, Hasirci N, MacNeil S, Hasirci V. Development of a UV crosslinked biodegradable hydrogel containing adipose derived stem cells to promote vascularization for skin wounds and tissue engineering. Biomaterials. 2017;129:188-98.
13. Mathupala SP, Kiousis S, Szerlip NJ. A lab assembled microcontroller-based sensor module for continuous oxygen measurement in portable hypoxia chambers. PLoS One. 2016;11(2):e0148923.

14. Rexius-Hall ML, Rehman J, Eddington DT. A microfluidic oxygen gradient demonstrates differential activation of the hypoxia-regulated transcription factors HIF-1α and HIF-2α. Integrative Biology. 2017;9(9):742-50.
15. Boyce MW, Simke WC, Kenney RM, Lockett MR. Generating linear oxygen gradients across 3D cell cultures with block-layered oxygen controlled chips (BLOCCs). Analytical Methods. 2020;12(1):18-24.
16. Dawes CS, Konig H, Lin C-C. Enzyme-immobilized hydrogels to create hypoxia for in vitro cancer cell culture. Journal of biotechnology. 2017;248:25-34.
17. Palacio-Castañeda V, Kooijman L, Venzac B, Verdurmen WP, Le Gac S. Metabolic switching of tumor cells under hypoxic conditions in a tumor-on-a-chip model. Micromachines. 2020;11(4):382.
18. Oh JM, Begum HM, Liu YL, Ren Y, Shen K. Recapitulating tumor hypoxia in a cleanroom-free, liquid-pinning-based microfluidic tumor model. ACS biomaterials science & engineering. 2022;8(7):3107-21.
19. Louis DN, Perry A, Reifenberger G, Von Deimling A, Figarella-Branger D, Cavenee WK, et al. The 2016 World Health Organization classification of tumors of the central nervous system: a summary. Acta neuropathologica. 2016;131:803-20.
20. Paolillo M, Comincini S, Schinelli S. In vitro glioblastoma models: A journey into the third dimension. Cancers. 2021;13(10):2449.
21. Brat DJ, Castellano-Sanchez AA, Hunter SB, Pecot M, Cohen C, Hammond EH, et al. Pseudopalisades in glioblastoma are hypoxic, express extracellular matrix proteases, and are formed by an actively migrating cell population. Cancer research. 2004;64(3):920-7.
22. Jain RK. Normalization of tumor vasculature: an emerging concept in antiangiogenic therapy. Science. 2005;307(5706):58-62.
23. Kim K-H, Migliozzi S, Koo H, Hong J-H, Park SM, Kim S, et al. Integrated proteogenomic characterization of glioblastoma evolution. Cancer cell. 2024;42(3):358-77. e8.
24. Lee Y, Park C-K, Park S-H. Prognostic Impact of TERT Promoter Mutations in Adult-Type Diffuse Gliomas Based on WHO2021 Criteria. Cancers. 2024;16(11):2032.
25. Verhaak RG, Hoadley KA, Purdom E, Wang V, Qi Y, Wilkerson MD, et al. Integrated genomic analysis identifies clinically relevant subtypes of glioblastoma characterized by abnormalities in PDGFRA, IDH1, EGFR, and NF1. Cancer cell. 2010;17(1):98-110.
26. Ohgaki H, Kleihues P. Genetic pathways to primary and secondary glioblastoma. The American journal of pathology. 2007;170(5):1445-53.
27. Yan H, Parsons DW, Jin G, McLendon R, Rasheed BA, Yuan W, et al. IDH1 and IDH2 mutations in gliomas. New England journal of medicine. 2009;360(8):765-73.
28. Higa N, Akahane T, Yokoyama S, Makino R, Yonezawa H, Uchida H, et al. Favorable prognostic impact of phosphatase and tensin homolog alterations in wild-type isocitrate dehydrogenase and telomerase reverse transcriptase promoter glioblastoma. Neuro-Oncology Advances. 2023;5(1):vdad078.

29. Suwala AK, Stichel D, Schrimpf D, Maas SL, Sill M, Dohmen H, et al. Glioblastomas with primitive neuronal component harbor a distinct methylation and copy-number profile with inactivation of TP53, PTEN, and RB1. Acta neuropathologica. 2021;142:179-89.
30. Chow LM, Endersby R, Zhu X, Rankin S, Qu C, Zhang J, et al. Cooperativity within and among Pten, p53, and Rb pathways induces high-grade astrocytoma in adult brain. Cancer cell. 2011;19(3):305-16.
31. Neftel C, Laffy J, Filbin MG, Hara T, Shore ME, Rahme GJ, et al. An integrative model of cellular states, plasticity, and genetics for glioblastoma. Cell. 2019;178(4):835-49. e21.
32. Yabo YA, Niclou SP, Golebiewska A. Cancer cell heterogeneity and plasticity: A paradigm shift in glioblastoma. Neuro-oncology. 2022;24(5):669-82.
33. Sottoriva A, Spiteri I, Piccirillo SG, Touloumis A, Collins VP, Marioni JC, et al. Intratumor heterogeneity in human glioblastoma reflects cancer evolutionary dynamics. Proceedings of the National Academy of Sciences. 2013;110(10):4009-14.
34. Wu H, Guo C, Wang C, Xu J, Zheng S, Duan J, et al. Single-cell RNA sequencing reveals tumor heterogeneity, microenvironment, and drug-resistance mechanisms of recurrent glioblastoma. Cancer science. 2023;114(6):2609-21.
35. Yi G-z, Huang G, Guo M, Zhang Xa, Wang H, Deng S, et al. Acquired temozolomide resistance in MGMT-deficient glioblastoma cells is associated with regulation of DNA repair by DHC2. Brain. 2019;142(8):2352-66.
36. Silvia N, Dai G. Cerebral organoids as a model for glioblastoma multiforme. Current opinion in biomedical engineering. 2020;13:152-9.
37. Dapash M, Hou D, Castro B, Lee-Chang C, Lesniak MS. The interplay between glioblastoma and its microenvironment. Cells. 2021;10(9):2257.
38. Collado J, Boland L, Ahrendsen JT, Miska J, Lee-Chang C. Understanding the glioblastoma tumor microenvironment: leveraging the extracellular matrix to increase immunotherapy efficacy. Frontiers in immunology. 2024;15:1336476.
39. Crivii C-B, Boșca AB, Melincovici CS, Constantin A-M, Mărginean M, Dronca E, et al. Glioblastoma Microenvironment and Cellular Interactions. Cancers. 2022;14(4).
40. Tamma R, Ingravallo G, Annese T, d'Amati A, Lorusso L, Ribatti D. Tumor microenvironment and microvascular density in human Glioblastoma. Cells. 2022;12(1):11.
41. Wolf KJ, Chen J, Coombes JD, Aghi MK, Kumar S. Dissecting and rebuilding the glioblastoma microenvironment with engineered materials. Nature Reviews Materials. 2019;4(10):651-68. (Permission ID: 1613969-1)
42. Brat DJ, Van Meir EG. Vaso-occlusive and prothrombotic mechanisms associated with tumor hypoxia, necrosis, and accelerated growth in glioblastoma. Laboratory investigation. 2004;84(4):397-405. (Permission ID: 1613980-1)

43. Marino S, Menna G, Di Bonaventura R, Lisi L, Mattogno P, Figà F, et al. The extracellular matrix in glioblastomas: a glance at its structural modifications in shaping the tumoral microenvironment—a systematic review. Cancers. 2023;15(6):1879.
44. Bauer R, Ratzinger S, Wales L, Bosserhoff A, Senner V, Grifka J, et al. Inhibition of collagen XVI expression reduces glioma cell invasiveness. Cellular Physiology and Biochemistry. 2011;27(3-4):217-26.
45. Chen J-WE, Pedron S, Shyu P, Hu Y, Sarkaria JN, Harley BA. Influence of hyaluronic acid transitions in tumor microenvironment on glioblastoma malignancy and invasive behavior. Frontiers in Materials. 2018;5:39.
46. Safarians G, Sohrabi A, Solomon I, Xiao W, Bastola S, Rajput BW, et al. Glioblastoma Spheroid Invasion through Soft, Brain-Like Matrices Depends on Hyaluronic Acid–CD44 Interactions. Advanced healthcare materials. 2023;12(14):2203143.
47. Mohiuddin E, Wakimoto H. Extracellular matrix in glioblastoma: opportunities for emerging therapeutic approaches. American journal of cancer research. 2021;11(8):3742.
48. Di Vito A, Donato A, Bria J, Conforti F, La Torre D, Malara N, et al. Extracellular matrix structure and interaction with immune cells in adult astrocytic tumors. Cellular and Molecular Neurobiology. 2024;44(1):54.
49. Sivakumar H, Strowd R, Skardal A. Exploration of dynamic elastic modulus changes on glioblastoma cell populations with aberrant EGFR expression as a potential therapeutic intervention using a tunable hyaluronic acid hydrogel platform. Gels. 2017;3(3):28.
50. Yan T, Wang K, Li J, Hu H, Yang H, Cai M, et al. Suppression of the hyaluronic acid pathway induces M1 macrophages polarization via STAT1 in glioblastoma. Cell Death Discovery. 2022;8(1):193.
51. Faisal SM, Comba A, Varela ML, Argento AE, Brumley E, Abel C, et al. The complex interactions between the cellular and non-cellular components of the brain tumor microenvironmental landscape and their therapeutic implications. Frontiers in Oncology. 2022;12:1005069.
52. Cesarini V, Silvestris DA, Tassinari V, Tomaselli S, Alon S, Eisenberg E, et al. ADAR2/miR-589-3p axis controls glioblastoma cell migration/invasion. Nucleic acids research. 2018;46(4):2045-59.
53. Kesanakurti D, Chetty C, Dinh DH, Gujrati M, Rao JS. Role of MMP-2 in the regulation of IL-6/Stat3 survival signaling via interaction with α5β1 integrin in glioma. Oncogene. 2013;32(3):327-40.
54. Cha J, Kang S-G, Kim P. Strategies of mesenchymal invasion of patient-derived brain tumors: microenvironmental adaptation. Scientific reports. 2016;6(1):24912.
55. Pointer KB, Clark PA, Schroeder AB, Salamat MS, Eliceiri KW, Kuo JS. Association of collagen architecture with glioblastoma patient survival. Journal of neurosurgery. 2016;126(6):1812-21.
56. Turtoi A, Blomme A, Bianchi E, Maris P, Vannozzi R, Naccarato AG, et al. Accessibilome of human glioblastoma: collagen-VI-alpha-1 is a new target and a marker of poor outcome. Journal of proteome research. 2014;13(12):5660-9.

57. Oldak L, Chludzinska-Kasperuk S, Milewska P, Grubczak K, Reszec J, Gorodkiewicz E. Laminin-5, fibronectin, and type IV collagen as potential biomarkers of brain glioma malignancy. Biomedicines. 2022;10(9):2290.
58. Sun T, Patil R, Galstyan A, Klymyshyn D, Ding H, Chesnokova A, et al. Blockade of a laminin-411–notch axis with CRISPR/Cas9 or a nanobioconjugate inhibits glioblastoma growth through tumor-microenvironment cross-talk. Cancer research. 2019;79(6):1239-51.
59. Fu Z, Zhu G, Luo C, Chen Z, Dou Z, Chen Y, et al. Matricellular protein tenascin C: Implications in glioma progression, gliomagenesis, and treatment. Frontiers in Oncology. 2022;12:971462.
60. Ventura E, Weller M, Macnair W, Eschbach K, Beisel C, Cordazzo C, et al. TGF-β induces oncofetal fibronectin that, in turn, modulates TGF-β superfamily signaling in endothelial cells. Journal of cell science. 2018;131(1):jcs209619.
61. Setargew YF, Wyllie K, Grant RD, Chitty JL, Cox TR. Targeting lysyl oxidase family meditated matrix cross-linking as an anti-stromal therapy in solid tumours. Cancers. 2021;13(3):491.
62. Wei J, Yao J, Yan M, Xie Y, Liu P, Mao Y, et al. The role of matrix stiffness in cancer stromal cell fate and targeting therapeutic strategies. Acta biomaterialia. 2022;150:34-47.
63. Guimarães CF, Gasperini L, Marques AP, Reis RL. The stiffness of living tissues and its implications for tissue engineering. Nature Reviews Materials. 2020;5(5):351-70.
64. Budday S, Sommer G, Birkl C, Langkammer C, Haybaeck J, Kohnert J, et al. Mechanical characterization of human brain tissue. Acta biomaterialia. 2017;48:319-40.
65. Bhargav AG, Domino JS, Chamoun R, Thomas SM. Mechanical properties in the glioma microenvironment: Emerging insights and theranostic opportunities. Frontiers in Oncology. 2022;11:805628.
66. Mahaffey BJ, Fowler ZP, Lung Z, Dang V, Lee H, Johnson AM, et al. The prognostic effect of mechanical, ultrastructural, and ECM signatures in glioblastoma core and rim. APL bioengineering. 2024;8(3).
67. Xiong J, Xiao R, Zhao J, Zhao Q, Luo M, Li F, et al. Matrix stiffness affects tumor-associated macrophage functional polarization and its potential in tumor therapy. Journal of Translational Medicine. 2024;22(1):85.
68. Casati G, Giunti L, Iorio AL, Marturano A, Galli L, Sardi I. Hippo pathway in regulating drug resistance of glioblastoma. International Journal of Molecular Sciences. 2021;22(24):13431.
69. Khoonkari M, Liang D, Kamperman M, Kruyt FA, van Rijn P. Physics of brain cancer: Multiscale alterations of glioblastoma cells under extracellular matrix stiffening. Pharmaceutics. 2022;14(5):1031.
70. Guerra-Rebollo M, Garrido C, Sánchez-Cid L, Soler-Botija C, Meca-Cortés O, Rubio N, et al. Targeting of replicating CD133 and OCT4/SOX2 expressing glioma stem cells selects a cell population that reinitiates tumors upon release of therapeutic pressure. Scientific reports. 2019;9(1):9549.

71. Jo H, Lee S, Kim M-H, Park S, Lee S-Y. Recapitulating Glioma Stem Cell Niches Using 3D Spheroid Models for Glioblastoma Research. Biosensors. 2024;14(11):539.
72. Soeda A, Hara A, Kunisada T, Yoshimura S-i, Iwama T, Park DM. The evidence of glioblastoma heterogeneity. Scientific reports. 2015;5(1):1-7.
73. Pine AR, Cirigliano SM, Singhania R, Nicholson J, Da Silva B, Leslie CS, et al. Microenvironment-driven dynamic chromatin changes in glioblastoma recapitulate early neural development at single-cell resolution. Cancer research. 2023;83(10):1581-95.
74. Lin H, Liu C, Hu A, Zhang D, Yang H, Mao Y. Understanding the immunosuppressive microenvironment of glioma: mechanistic insights and clinical perspectives. Journal of hematology & oncology. 2024;17(1):31.
75. Mączyńska J, Raes F, Da Pieve C, Turnock S, Boult JK, Hoebart J, et al. Triggering anti-GBM immune response with EGFR-mediated photoimmunotherapy. BMC medicine. 2022;20(1):16.
76. Solomou G, Young AM, Bulstrode HJ. Microglia and macrophages in glioblastoma: landscapes and treatment directions. Molecular Oncology. 2024;18(12):2906-26.
77. Poon CC, Sarkar S, Yong VW, Kelly JJ. Glioblastoma-associated microglia and macrophages: targets for therapies to improve prognosis. Brain. 2017;140(6):1548-60.
78. Hambardzumyan D, Gutmann DH, Kettenmann H. The role of microglia and macrophages in glioma maintenance and progression. Nature neuroscience. 2016;19(1):20-7.
79. Zheng Y, Fuse H, Alzoubi I, Graeber MB. Microglia-derived brain macrophages associate with glioblastoma stem cells: a potential mechanism for tumor progression revealed by AI-assisted analysis. Cells. 2025;14(6):413.
80. Lauko A, Lo A, Ahluwalia MS, Lathia JD, editors. Cancer cell heterogeneity & plasticity in glioblastoma and brain tumors. Seminars in cancer biology; 2022;82:162-175.
81. Becker AP, Sells BE, Haque SJ, Chakravarti A. Tumor heterogeneity in glioblastomas: from light microscopy to molecular pathology. Cancers. 2021;13(4):761.
82. Nader NE, Frederico SC, Miller T, Huq S, Zhang X, Kohanbash G, et al. Barriers to T Cell Functionality in the Glioblastoma Microenvironment. Cancers. 2024;16(19):3273.
83. Pace A, Scirocchi F, Napoletano C, Zizzari IG, D'Angelo L, Santoro A, et al. Glycan-lectin interactions as novel immunosuppression drivers in glioblastoma. International journal of molecular sciences. 2022;23(11):6312.
84. Zhang Y, He H, Fu X, Liu G, Wang H, Zhong W, et al. Glioblastoma-associated macrophages in glioblastoma: from their function and mechanism to therapeutic advances. Cancer Gene Therapy. 2025:1-13.
85. Wang X, Ge Y, Hou Y, Wang X, Yan Z, Li Y, et al. Single-cell atlas reveals the immunosuppressive microenvironment and Treg cells landscapes in recurrent Glioblastoma. Cancer Gene Therapy. 2024;31(5):790-801.

86. Awad NS, Salkho NM, Abuwatfa WH, Paul V, AlSawaftah NM, Husseini GA. Tumor vasculature vs tumor cell targeting: Understanding the latest trends in using functional nanoparticles for cancer treatment. OpenNano. 2023;11:100136.
87. Park S, Avera AD, Kim Y. Biomanufacturing of glioblastoma organoids exhibiting hierarchical and spatially organized tumor microenvironment via transdifferentiation. Biotechnology and Bioengineering. 2022;119(11):3252-74.
88. Pantazopoulou V, Jeannot P, Rosberg R, Berg TJ, Pietras A. Hypoxia-induced reactivity of tumor-associated astrocytes affects glioma cell properties. Cells. 2021;10(3):613.
89. Wu J, Li R, Wang J, Zhu H, Ma Y, You C, et al. Reactive Astrocytes in Glioma: Emerging Opportunities and Challenges. International Journal of Molecular Sciences. 2025;26(7):2907.
90. Perelroizen R, Philosof B, Budick-Harmelin N, Chernobylsky T, Ron A, Katzir R, et al. Astrocyte immunometabolic regulation of the tumour microenvironment drives glioblastoma pathogenicity. Brain. 2022;145(9):3288-307.
91. Chen W-L, Wang C-C, Lin Y-J, Wu C-P, Hsieh C-H. Cycling hypoxia induces chemoresistance through the activation of reactive oxygen species-mediated B-cell lymphoma extra-long pathway in glioblastoma multiforme. Journal of translational medicine. 2015;13:1-13.
92. Chou C-W, Wang C-C, Wu C-P, Lin Y-J, Lee Y-C, Cheng Y-W, et al. Tumor cycling hypoxia induces chemoresistance in glioblastoma multiforme by upregulating the expression and function of ABCB1. Neuro-oncology. 2012;14(10):1227-38.
93. Linsenmann T, Jawork A, Westermaier T, Homola G, Monoranu CM, Vince GH, et al. Tumor growth under rhGM-CSF application in an orthotopic rodent glioma model. Oncology Letters. 2019;17(6):4843-50.
94. Chigurupati S, Venkataraman R, Barrera D, Naganathan A, Madan M, Paul L, et al. Receptor channel TRPC6 is a key mediator of Notch-driven glioblastoma growth and invasiveness. Cancer research. 2010;70(1):418-27.
95. Huang W-J, Chen W-W, Zhang X. Glioblastoma multiforme: Effect of hypoxia and hypoxia inducible factors on therapeutic approaches. Oncology letters. 2016;12(4):2283-8.
96. De Groot JF, Fuller G, Kumar AJ, Piao Y, Eterovic K, Ji Y, et al. Tumor invasion after treatment of glioblastoma with bevacizumab: radiographic and pathologic correlation in humans and mice. Neuro-oncology. 2010;12(3):233-42.
97. Bao B, Azmi AS, Ali S, Ahmad A, Li Y, Banerjee S, et al. The biological kinship of hypoxia with CSC and EMT and their relationship with deregulated expression of miRNAs and tumor aggressiveness. Biochimica et Biophysica Acta (BBA)-Reviews on Cancer. 2012;1826(2):272-96.
98. Barthel L, Hadamitzky M, Dammann P, Schedlowski M, Sure U, Thakur BK, et al. Glioma: molecular signature and crossroads with tumor microenvironment. Cancer and Metastasis Reviews. 2022:1-23.

99. Hsieh C-H, Lin Y-J, Wu C-P, Lee H-T, Shyu W-C, Wang C-C. Livin contributes to tumor hypoxia–induced resistance to cytotoxic therapies in glioblastoma multiforme. Clinical Cancer Research. 2015;21(2):460-70.
100. Yu MO, Park K-J, Park D-H, Chung Y-G, Chi S-G, Kang S-H. Reactive oxygen species production has a critical role in hypoxia-induced Stat3 activation and angiogenesis in human glioblastoma. Journal of neuro-oncology. 2015;125:55-63.
101. Rosenberg T, Thomassen M, Jensen SS, Larsen MJ, Sørensen KP, Hermansen SK, et al. Acute hypoxia induces upregulation of microRNA-210 expression in glioblastoma spheroids. CNS oncology. 2015;4(1):25-35.
102. Wu W, Hu Q, Nie E, Yu T, Wu Y, Zhi T, et al. Hypoxia induces H19 expression through direct and indirect Hif-1α activity, promoting oncogenic effects in glioblastoma. Scientific reports. 2017;7(1):45029.
103. Agrawal R, Pandey P, Jha P, Dwivedi V, Sarkar C, Kulshreshtha R. Hypoxic signature of microRNAs in glioblastoma: insights from small RNA deep sequencing. BMC genomics. 2014;15:1-16.
104. Hanif F, Muzaffar K, Perveen K, Malhi SM, Simjee SU. Glioblastoma multiforme: a review of its epidemiology and pathogenesis through clinical presentation and treatment. Asian Pacific journal of cancer prevention: APJCP. 2017;18(1):3.
105. Anjum K, Shagufta BI, Abbas SQ, Patel S, Khan I, Shah SAA, et al. Current status and future therapeutic perspectives of glioblastoma multiforme (GBM) therapy: A review. Biomedicine & Pharmacotherapy. 2017;92:681-9.
106. Ocana A, Pandiella A, Privat C, Bravo I, Luengo-Oroz M, Amir E, et al. Integrating artificial intelligence in drug discovery and early drug development: a transformative approach. Biomarker Research. 2025;13(1):45.
107. Esposito A, Ferraresi A, Vallino L, Garavaglia B, Dhanasekaran DN, Isidoro C. Three-Dimensional In Vitro Cell Cultures as a Feasible and Promising Alternative to Two-Dimensional and Animal Models in Cancer Research. International Journal of Biological Sciences. 2024;20(13):5293.
108. Brancato V, Oliveira JM, Correlo VM, Reis RL, Kundu SC. Could 3D models of cancer enhance drug screening? Biomaterials. 2020;232:119744.
109. Skardal A, Mack D, Atala A, Soker S. Substrate elasticity controls cell proliferation, surface marker expression and motile phenotype in amniotic fluid-derived stem cells. Journal of the mechanical behavior of biomedical materials. 2013;17:307-16.
110. Dai X, Ma C, Lan Q, Xu T. 3D bioprinted glioma stem cells for brain tumor model and applications of drug susceptibility. Biofabrication. 2016;8(4):045005.
111. Barbosa MA, Xavier CP, Pereira RF, Petrikaitė V, Vasconcelos MH. 3D cell culture models as recapitulators of the tumor microenvironment for the screening of anti-cancer drugs. Cancers. 2021;14(1):190.

112. Pollard SM, Yoshikawa K, Clarke ID, Danovi D, Stricker S, Russell R, et al. Glioma stem cell lines expanded in adherent culture have tumor-specific phenotypes and are suitable for chemical and genetic screens. Cell stem cell. 2009;4(6):568-80.
113. Pencheva N, de Gooijer MC, Vis DJ, Wessels LF, Würdinger T, van Tellingen O, et al. Identification of a druggable pathway controlling glioblastoma invasiveness. Cell reports. 2017;20(1):48-60.
114. Wang C, Tong X, Yang F. Bioengineered 3D brain tumor model to elucidate the effects of matrix stiffness on glioblastoma cell behavior using PEG-based hydrogels. Molecular pharmaceutics. 2014;11(7):2115-25.
115. Idrisova K, Simon H-U, Gomzikova M. Role of patient-derived models of cancer in translational oncology. Cancers. 2022;15(1):139.
116. Akolawala Q, Keuning F, Rovituso M, van Burik W, van der Wal E, Versteeg HH, et al. Micro-Vessels-Like 3D Scaffolds for Studying the Proton Radiobiology of Glioblastoma-Endothelial Cells Co-Culture Models. Advanced Healthcare Materials. 2024;13(6):2302988.
117. Carvalho EM, Ding EA, Saha A, Garcia DC, Weldy A, Zushin PJH, et al. Viscoelastic High-Molecular-Weight Hyaluronic Acid Hydrogels Support Rapid Glioblastoma Cell Invasion with Leader–Follower Dynamics. Advanced Materials. 2024;36(50):2404885.
118. Zhang C, Jin M, Zhao J, Chen J, Jin W. Organoid models of glioblastoma: advances, applications and challenges. American Journal of Cancer Research. 2020;10(8):2242.
119. Mangena V, Chanoch-Myers R, Sartore R, Paulsen B, Gritsch S, Weisman H, et al. Glioblastoma Cortical Organoids Recapitulate Cell-State Heterogeneity and Intercellular Transfer. Cancer Discovery. 2025;15(2):299-315.
120. Azzarelli R, Ori M, Philpott A, Simons BD. Three-dimensional model of glioblastoma by co-culturing tumor stem cells with human brain organoids. Biology Open. 2021;10(2):bio056416.
121. Tung YT, Chen YC, Derr K, Wilson K, Song MJ, Ferrer M. A 3D bioprinted human neurovascular unit model of glioblastoma tumor growth. Advanced Healthcare Materials. 2024;13(15):2302831.
122. Tang M, Xie Q, Gimple RC, Zhong Z, Tam T, Tian J, et al. Three-dimensional bioprinted glioblastoma microenvironments model cellular dependencies and immune interactions. Cell research. 2020;30(10):833-53.
123. Heinrich MA, Bansal R, Lammers T, Zhang YS, Michel Schiffelers R, Prakash J. 3D-bioprinted mini-brain: a glioblastoma model to study cellular interactions and therapeutics. Advanced materials. 2019;31(14):1806590.
124. Bayona C, Alza L, Ranđelović T, Sallán MC, Visa A, Cantí C, et al. Tetralol derivative NNC-55-0396 targets hypoxic cells in the glioblastoma microenvironment: an organ-on-chip approach. Cell Death & Disease. 2024;15(2):127.
125. Dou J, Mao S, Li H, Lin J-M. Combination stiffness gradient with chemical stimulation directs glioma cell migration on a microfluidic chip. Analytical chemistry. 2019;92(1):892-8.

126. Diep YN, Park HJ, Zhu X, Nam JH, Shim JK, Chang JH, et al. A Neuroimmune-Oncology Microphysiological Analysis Platform (NEO-MAP) for Evaluating Astrocytic Scar Formation and Microgliosis in Glioblastoma Microenvironment. Advanced Healthcare Materials. 2025;14(11):2404821.
127. Martins AM, Brito A, Barbato MG, Felici A, Reis RL, Pires RA, et al. Efficacy of molecular and nano-therapies on brain tumor models in microfluidic devices. Biomaterials Advances. 2023;144:213227.
128. Rane A, Tate S, Sumey JL, Zhong Q, Zong H, Purow B, et al. Open-top patterned hydrogel-laden 3D glioma cell cultures for creation of dynamic chemotactic gradients to direct cell migration. ACS Biomaterials Science & Engineering. 2024;10(5):3470-7.
129. Amemiya T, Hata N, Mizoguchi M, Yokokawa R, Kawamura Y, Hatae R, et al. Mesenchymal glioblastoma-induced mature de-novo vessel formation of vascular endothelial cells in a microfluidic device. Molecular biology reports. 2021;48:395-403.
130. Adjei-Sowah EA, O'Connor SA, Veldhuizen J, Lo Cascio C, Plaisier C, Mehta S, et al. Investigating the Interactions of Glioma Stem Cells in the Perivascular Niche at Single-Cell Resolution using a Microfluidic Tumor Microenvironment Model. Advanced Science. 2022;9(21):2201436.
131. Song J, Lee Y, Kim M-S, Ha G, Jang W, Batjargal U, et al. High throughput drug screening platform utilizing capillary and artery cell layered models based on tumor–vascular cell interactions. Lab on a Chip. 2025.
132. Pun S, Prakash A, Demaree D, Krummel DP, Sciumè G, Sengupta S, et al. Rapid Biofabrication of an Advanced Microphysiological System Mimicking Phenotypical Heterogeneity and Drug Resistance in Glioblastoma. Advanced Healthcare Materials. 2024;13(30):2401876.
133. Shi Y, He X, Wang H, Dai J, Fang J, He Y, et al. Construction of a novel blood brain barrier-glioma microfluidic chip model: Applications in the evaluation of permeability and anti-glioma activity of traditional Chinese medicine components. Talanta. 2023;253:123971.
134. Simsa R, Rothenbücher T, Gürbüz H, Ghosheh N, Emneus J, Jenndahl L, et al. Brain organoid formation on decellularized porcine brain ECM hydrogels. PloS one. 2021;16(1):e0245685.
135. Jaffer S, Bleiweiss IJ. Beyond hematoxylin and eosin—the role of immunohistochemistry in surgical pathology. Cancer investigation. 2004;22(3):445-65.
136. Ji Y, Yang X, Ji Z, Zhu L, Ma N, Chen D, et al. DFT-calculated IR spectrum amide I, II, and III band contributions of N-methylacetamide fine components. ACS omega. 2020;5(15):8572-8.
137. Lozano M, Rodríguez-Ulibarri P, Echeverría J, Beruete M, Sorolla M, Beriain M. Mid-infrared spectroscopy (MIR) for simultaneous determination of fat and protein content in meat of several animal species. Food Analytical Methods. 2017;10(10):3462-70.
138. Freytes DO, Martin J, Velankar SS, Lee AS, Badylak SF. Preparation and rheological characterization of a gel form of the porcine urinary bladder matrix. Biomaterials. 2008;29(11):1630-7.

139. Dabaghi M, Saraei N, Carpio MB, Nanduri V, Ungureanu J, Babi M, et al. A robust protocol for decellularized human lung bioink generation amenable to 2D and 3D lung cell culture. Cells. 2021;10(6):1538.
140. Bencherif SA, Srinivasan A, Horkay F, Hollinger JO, Matyjaszewski K, Washburn NR. Influence of the degree of methacrylation on hyaluronic acid hydrogels properties. Biomaterials. 2008;29(12):1739-49.
141. Isik S, Yucel D, Hasirci V. Development of a Hydrogel Platform with GBM and Microglia: A Potential Glioblastoma Tumor Model. ACS Applied Bio Materials. 2025;8(9):7757-7770.
142. Velasco-Rodriguez B, Diaz-Vidal T, Rosales-Rivera LC, García-González CA, Alvarez-Lorenzo C, Al-Modlej A, et al. Hybrid methacrylated gelatin and hyaluronic acid hydrogel scaffolds. Preparation and systematic characterization for prospective tissue engineering applications. International Journal of Molecular Sciences. 2021;22(13):6758.
143. Mendoza-Cerezo L, Rodríguez-Rego JM, Macías-García A, Callejas-Marín A, Sánchez-Guardado L, Marcos-Romero AC. Three-Dimensional bioprinting of GelMA hydrogels with culture medium: balancing printability, rheology and cell viability for tissue regeneration. Polymers. 2024;16(10):1437.
144. Yucel D, Kose GT, Hasirci V. Tissue engineered, guided nerve tube consisting of aligned neural stem cells and astrocytes. Biomacromolecules. 2010;11(12):3584-91.
145. Antmen E, Demirci U, Hasirci V. Micropatterned Surfaces Expose the Coupling between Actin Cytoskeleton-Lamin/Nesprin and Nuclear Deformability of Breast Cancer Cells with Different Malignancies. Advanced biology. 2021;5(1):2000048.
146. Ayuso JM, Monge R, Martínez-González A, Virumbrales-Muñoz M, Llamazares GA, Berganzo J, et al. Glioblastoma on a microfluidic chip: Generating pseudopalisades and enhancing aggressiveness through blood vessel obstruction events. Neuro-oncology. 2017;19(4):503-13.
147. Wang P, Zhao L, Gong S, Xiong S, Wang J, Zou D, et al. HIF1α/HIF2α–Sox2/Klf4 promotes the malignant progression of glioblastoma via the EGFR–PI3K/AKT signalling pathway with positive feedback under hypoxia. Cell Death & Disease. 2021;12(4):312.
148. Wang Y, Liu T, Yang N, Xu S, Li X, Wang D. Hypoxia and macrophages promote glioblastoma invasion by the CCL4-CCR5 axis. Oncology reports. 2016;36(6):3522-8.
149. Wu Y, Clark KC, Nguyen EV, Niranjan B, Horvath LG, Taylor RA, et al. Proteomic characterisation of prostate cancer intercellular communication reveals cell type-selective signalling and TMSB4X-dependent fibroblast reprogramming. Cellular Oncology. 2022;45(6):1311-28.
150. Soni V, Adhikari M, Simonyan H, Lin L, Sherman JH, Young CN, et al. In vitro and in vivo enhancement of temozolomide effect in human glioblastoma by non-invasive application of cold atmospheric plasma. Cancers. 2021;13(17):4485.
151. Castro GN, Cayado-Gutiérrez N, Zoppino FCM, Fanelli MA, Cuello-Carrión FD, Sottile M, et al. Effects of temozolomide (TMZ) on the expression and interaction of heat shock proteins (HSPs)

and DNA repair proteins in human malignant glioma cells. Cell Stress and Chaperones. 2015;20(2):253-65.

152. Narciso M, Otero J, Navajas D, Farré R, Almendros I, Gavara N. Image-based method to quantify decellularization of tissue sections. International journal of molecular sciences. 2021;22(16):8399.

153. Mendibil U, Ruiz-Hernandez R, Retegi-Carrion S, Garcia-Urquia N, Olalde-Graells B, Abarrategi A. Tissue-specific decellularization methods: rationale and strategies to achieve regenerative compounds. International journal of molecular sciences. 2020;21(15):5447.

154. Crapo PM, Gilbert TW, Badylak SF. An overview of tissue and whole organ decellularization processes. Biomaterials. 2011;32(12):3233-43.

155. Ju H, Liu X, Zhang G, Liu D, Yang Y. Comparison of the structural characteristics of native collagen fibrils derived from bovine tendons using two different methods: modified acid-solubilized and pepsin-aided extraction. Materials. 2020;13(2):358.

156. Fazel Anvari Yazdi A, Tahermanesh K, Ejlali M, Babaei-Ghazvini A, Acharya B, Badea I, et al. Comparative analysis of porcine-uterine decellularization for bioactive-molecule preservation and DNA removal. Frontiers in Bioengineering and Biotechnology. 2024;12:1418034.

157. Villamil Ballesteros AC, Segura Puello HR, Lopez-Garcia JA, Bernal-Ballen A, Nieto Mosquera DL, Munoz Forero DM, et al. Bovine decellularized amniotic membrane: Extracellular matrix as scaffold for mammalian skin. Polymers. 2020;12(3):590.

158. Kanchanawong P, Calderwood DA. Organization, dynamics and mechanoregulation of integrin-mediated cell–ECM adhesions. Nature Reviews Molecular Cell Biology. 2023;24(2):142-61.

159. Comba A, Faisal SM, Dunn PJ, Argento AE, Hollon TC, Al-Holou WN, et al. Spatiotemporal analysis of glioma heterogeneity reveals COL1A1 as an actionable target to disrupt tumor progression. Nature communications. 2022;13(1):3606.

160. Chédeville AL, Lourdusamy A, Monteiro AR, Hill R, Madureira PA. Investigating glioblastoma response to hypoxia. Biomedicines. 2020;8(9):310.

161. Stanke KM, Wilson C, Kidambi S. High expression of glycolytic genes in clinical glioblastoma patients correlates with lower survival. Frontiers in Molecular Biosciences. 2021;8:752404.

162. D'Aprile S, Denaro S, Gervasi A, Vicario N, Parenti R. Targeting metabolic reprogramming in glioblastoma as a new strategy to overcome therapy resistance. Frontiers in Cell and Developmental Biology. 2025;13:1535073.

163. Lee S-H, Golinska M, Griffiths JR. HIF-1-independent mechanisms regulating metabolic adaptation in hypoxic cancer cells. Cells. 2021;10(9):2371.

164. Infantino V, Santarsiero A, Convertini P, Todisco S, Iacobazzi V. Cancer cell metabolism in hypoxia: role of HIF-1 as key regulator and therapeutic target. International journal of molecular sciences. 2021;22(11):5703.

165. Hohmann T, Dehghani F. The cytoskeleton—a complex interacting meshwork. Cells. 2019;8(4):362.

166. Kumar R, Mishra A, Gautam P, Feroz Z, Vijayaraghavalu S, Likos EM, et al. Metabolic pathways, enzymes, and metabolites: opportunities in cancer therapy. Cancers. 2022;14(21):5268.
167. Hagemann C, Anacker J, Ernestus R-I, Vince GH. A complete compilation of matrix metalloproteinase expression in human malignant gliomas. World journal of clinical oncology. 2012;3(5):67.
168. Fang W, Yang M, Wang L, Li W, Liu M, Jin Y, et al. Hydrogels for 3D bioprinting in tissue engineering and regenerative medicine: Current progress and challenges. International journal of bioprinting. 2023;9(5):759.
169. Askari M, Naniz MA, Kouhi M, Saberi A, Zolfagharian A, Bodaghi M. Recent progress in extrusion 3D bioprinting of hydrogel biomaterials for tissue regeneration: a comprehensive review with focus on advanced fabrication techniques. Biomaterials science. 2021;9(3):535-73.
170. Miroshnikova YA, Mouw JK, Barnes JM, Pickup MW, Lakins JN, Kim Y, et al. Tissue mechanics promote IDH1-dependent HIF1α–tenascin C feedback to regulate glioblastoma aggression. Nature cell biology. 2016;18(12):1336-45.
171. Kondapaneni RV, Gurung SK, Nakod PS, Goodarzi K, Yakati V, Lenart NA, et al. Glioblastoma mechanobiology at multiple length scales. Biomaterials Advances. 2024:213860.
172. Cha J, Ding EA, Carvalho EM, Fowler A, Aghi MK, Kumar S. Collagen VI deposition primes the glioblastoma microenvironment for invasion through mechanostimulation of β-catenin signaling. PNAS nexus. 2024;3(9):pgae355.
173. Schregel K, Nazari N, Nowicki MO, Palotai M, Lawler SE, Sinkus R, et al. Characterization of glioblastoma in an orthotopic mouse model with magnetic resonance elastography. NMR in Biomedicine. 2018;31(10):e3840.
174. Parkins CC, McAbee JH, Ruff L, Wendler A, Mair R, Gilbertson RJ, et al. Mechanically matching the rheological properties of brain tissue for drug-delivery in human glioblastoma models. Biomaterials. 2021;276:120919.
175. Maity S, Jewell C, Yilgor C, Kawakita S, Sharma S, Gomez A, et al. Deciphering pericyte-induced temozolomide resistance in glioblastoma with a 3D microphysiological system mimicking the biomechanical properties of brain tissue. Acta Biomaterialia. 2025;200:202-217.
176. Peng Z, Lv X, Sun H, Zhao L, Huang S. 3D tumor cultures for drug resistance and screening development in clinical applications. Molecular Cancer. 2025;24(1):93.
177. Zhang Y, Fu Q, Sun W, Yue Q, He P, Niu D, et al. Mechanical forces in the tumor microenvironment: roles, pathways, and therapeutic approaches. Journal of Translational Medicine. 2025;23(1):313.
178. Johnson AM, Froman-Glover C, Mistry A, Yaddanapudi K, Chen J. The impact of compression and confinement in tumor growth and progression: emerging concepts in cancer mechanobiology. Frontiers in Materials. 2025;12:1492438.
179. Oros-Peusquens A-M, Keil F, Langen K, Herzog H, Stoffels G, Weiss C, et al. Fast and accurate water content and T2∗ mapping in brain tumours localised with FET-PET. Nuclear Instruments and

Methods in Physics Research Section A: Accelerators, Spectrometers, Detectors and Associated Equipment. 2014;734:185-90.

180. Oros-Peusquens A-M, Loução R, Abbas Z, Gras V, Zimmermann M, Shah N. A single-scan, rapid whole-brain protocol for quantitative water content mapping with neurobiological implications. Frontiers in Neurology. 2019;10:1333.

181. Lin Z-X. Glioma-related edema: new insight into molecular mechanisms and their clinical implications. Chinese journal of cancer. 2013;32(1):49.

182. Thai VL, Ramos-Rodriguez DH, Mesfin M, Leach JK. Hydrogel degradation promotes angiogenic and regenerative potential of cell spheroids for wound healing. Materials Today Bio. 2023;22:100769.

183. Zhang F, King MW. Biodegradable polymers as the pivotal player in the design of tissue engineering scaffolds. Advanced healthcare materials. 2020;9(13):1901358.

184. González-Callejo P, Vázquez-Aristizabal P, García-Astrain C, de Aberasturi DJ, Henriksen-Lacey M, Izeta A, et al. 3D bioprinted breast tumor-stroma models for pre-clinical drug testing. Materials Today Bio. 2023;23:100826.

185. Hewawasam RS, Blomberg R, Šerbedžija P, Magin CM. Chemical modification of human decellularized extracellular matrix for incorporation into phototunable hybrid-hydrogel models of tissue fibrosis. ACS applied materials & interfaces. 2023;15(12):15071-83.

186. Wu X, Shi W, Liu X, Gu Z. Recent advances in 3D-printing-based organ-on-a-chip. EngMedicine. 2024:100003.

187. Lanza M, Casili G, Campolo M, Paterniti I, Colarossi C, Mare M, et al. Immunomodulatory effect of microglia-released cytokines in gliomas. Brain sciences. 2021;11(4):466.

188. Reiche L, Plaack B, Lehmkuhl M, Weyers V, Gruchot J, Picard D, et al. HERV-W envelope protein is present in microglial cells of the human glioma tumor microenvironment and differentially modulates neoplastic cell behavior. Microbes and Infection. 2024:105460.

189. Liu H, Sun Y, Zhang Q, Jin W, Gordon RE, Zhang Y, et al. Pro-inflammatory and proliferative microglia drive progression of glioblastoma. Cell reports. 2021;36(11).

190. Yeini E, Ofek P, Pozzi S, Albeck N, Ben-Shushan D, Tiram G, et al. P-selectin axis plays a key role in microglia immunophenotype and glioblastoma progression. Nature communications. 2021;12(1):1912.

191. Madan A, Saini R, Dhiman N, Juan S-H, Satapathy MK. Organoids as Next-Generation Models for Tumor Heterogeneity, Personalized Therapy, and Cancer Research: Advancements, Applications, and Future Directions. Organoids. 2025;4(4):23.

192. Li W, Zhou Z, Zhou X, Khoo BL, Gunawan R, Chin YR, et al. 3D biomimetic models to reconstitute tumor microenvironment in vitro: spheroids, organoids, and tumor-on-a-chip. Advanced healthcare materials. 2023;12(18):2202609.

193. Yi HG, Jeong YH, Kim Y, Choi YJ, Moon HE, Park SH, et al. A bioprinted human-glioblastoma-on-a-chip for the identification of patient-specific responses to chemoradiotherapy. Nat Biomed Eng. 2019;3(7):509-19.
194. Hatanpaa KJ, Burma S, Zhao D, Habib AA. Epidermal growth factor receptor in glioma: signal transduction, neuropathology, imaging, and radioresistance. Neoplasia. 2010;12(9):675-84.
195. Dahlrot RH, Bangsø JA, Petersen JK, Rosager AM, Sørensen MD, Reifenberger G, et al. Prognostic role of Ki-67 in glioblastomas excluding contribution from non-neoplastic cells. Scientific reports. 2021;11(1):17918.
196. Steponaitis G, Skiriutė D, Kazlauskas A, Golubickaitė I, Stakaitis R, Tamašauskas A, et al. High CHI3L1 expression is associated with glioma patient survival. Diagnostic pathology. 2016;11:1-8.
197. Brochu-Gaudreau K, Charbonneau M, Harper K, Dubois CM. Hypoxia selectively increases a SMAD3 signaling Axis to promote cancer cell invasion. Cancers. 2022;14(11):2751.
198. Chen A, Jiang Y, Li Z, Wu L, Santiago U, Zou H, et al. Chitinase-3-like 1 protein complexes modulate macrophage-mediated immune suppression in glioblastoma. The Journal of clinical investigation. 2021;131(16).
199. Macharia LW, Muriithi W, Nyaga DK, de Mattos Coelho-Aguiar J, de Sampaio e Spohr TCL, Moura-Neto V. Evaluation of MiRNA Expression in Glioblastoma Stem-Like Cells: A Comparison between Normoxia and Hypoxia Microenvironment. Onco. 2022;2(2):113-28.
200. Liu D, Wan Y, Qu N, Fu Q, Liang C, Zeng L, et al. LncRNA-FAM66C was identified as a key regulator for modulating tumor microenvironment and hypoxia-related pathways in glioblastoma. Frontiers in public health. 2022;10:898270.
201. Abd Elmaogod EA, Daoud SA, Mostafa ZM, Mahmoud EMM. Prognostic significance of HIF1-α immunohistochemical expression in gliomas and it's relation to IDH1 mutation status. Beni-Suef University Journal of Basic and Applied Sciences. 2022;11(1):140.
202. Coniglio SJ, Segall JE. Molecular mechanism of microglia stimulated glioblastoma invasion. Matrix Biology. 2013;32(7-8):372-80.
203. Nishikawa M, Inoue A, Ohnishi T, Yano H, Ozaki S, Kanemura Y, et al. Hypoxia-induced phenotypic transition from highly invasive to less invasive tumors in glioma stem-like cells: Significance of CD44 and osteopontin as therapeutic targets in glioblastoma. Translational oncology. 2021;14(8):101137.
204. Yosef G, Hayun H, Papo N. Simultaneous targeting of CD44 and MMP9 catalytic and hemopexin domains as a therapeutic strategy. Biochemical Journal. 2021;478(5):1139-57.
205. Wei K-C, Huang C-Y, Chen P-Y, Feng L-Y, Wu T-WE, Chen S-M, et al. Evaluation of the prognostic value of CD44 in glioblastoma multiforme. Anticancer research. 2010;30(1):253-9.
206. Lubanska D, Alrashed S, Mason GT, Nadeem F, Awada A, DiPasquale M, et al. Impairing proliferation of glioblastoma multiforme with CD44+ selective conjugated polymer nanoparticles. Scientific Reports. 2022;12(1):12078.

207. Ouanouki A, Lamy S, Annabi B. Periostin, a signal transduction intermediate in TGF-β-induced EMT in U-87MG human glioblastoma cells, and its inhibition by anthocyanidins. Oncotarget. 2018;9(31):22023.
208. Joseph JV, Conroy S, Pavlov K, Sontakke P, Tomar T, Eggens-Meijer E, et al. Hypoxia enhances migration and invasion in glioblastoma by promoting a mesenchymal shift mediated by the HIF1α–ZEB1 axis. Cancer letters. 2015;359(1):107-16.
209. Monteiro AR, Hill R, Pilkington GJ, Madureira PA. The role of hypoxia in glioblastoma invasion. Cells. 2017;6(4):45.
210. Torres Á, Erices JI, Sanchez F, Ehrenfeld P, Turchi L, Virolle T, et al. Extracellular adenosine promotes cell migration/invasion of Glioblastoma Stem-like Cells through A3 Adenosine Receptor activation under hypoxia. Cancer letters. 2019;446:112-22.
211. Tian Y, Cheng T, Sun F, Zhou Y, Yuan C, Guo Z, et al. Effect of biophysical properties of tumor extracellular matrix on intratumoral fate of nanoparticles: Implications on the design of nanomedicine. Advances in Colloid and Interface Science. 2024:103124.
212. Ge X, Pan M-H, Wang L, Li W, Jiang C, He J, et al. Hypoxia-mediated mitochondria apoptosis inhibition induces temozolomide treatment resistance through miR-26a/Bad/Bax axis. Cell death & disease. 2018;9(11):1128.
213. Poon MT, Bruce M, Simpson JE, Hannan CJ, Brennan PM. Temozolomide sensitivity of malignant glioma cell lines–a systematic review assessing consistencies between in vitro studies. BMC cancer. 2021;21:1-9.

8 APPENDIX

APPENDIX 1

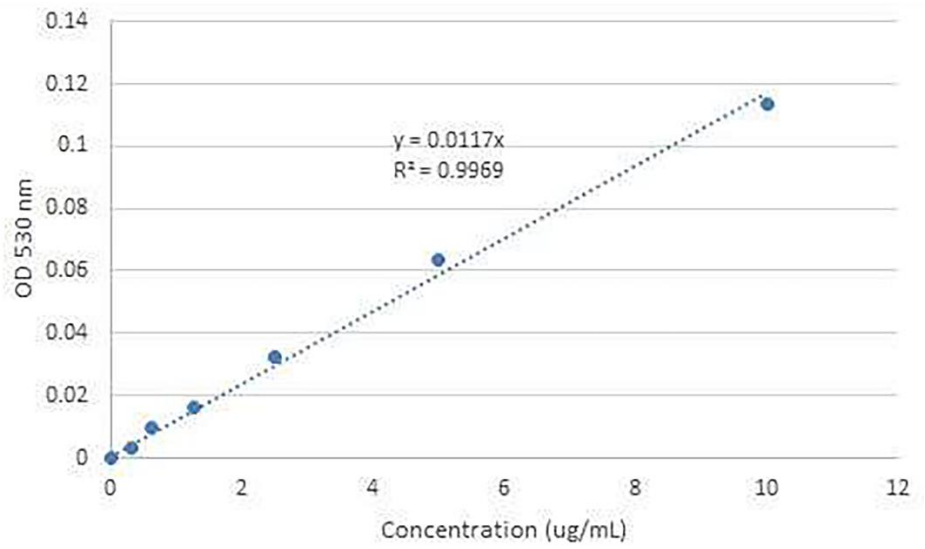

Appentix 1. Chondroitin sulfate standard curve

APPENDIX 2

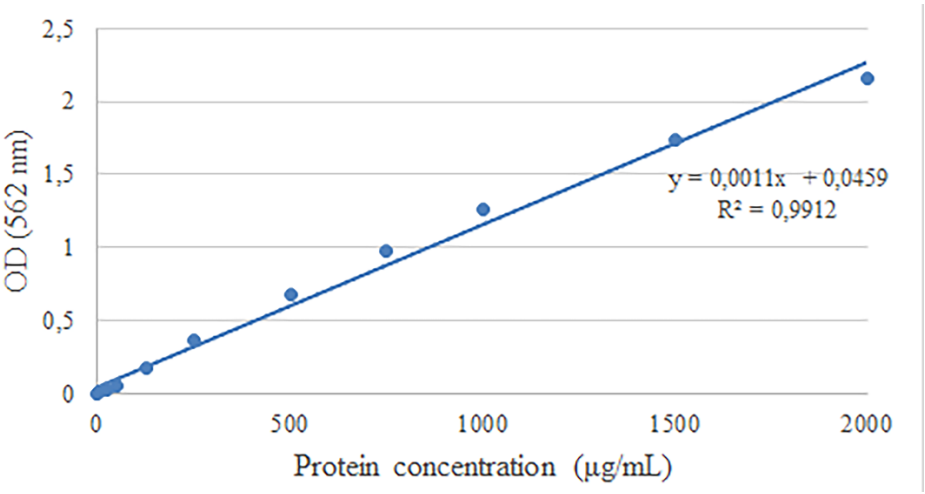

Appentix 2. BSA standard curve

APPENDIX 3

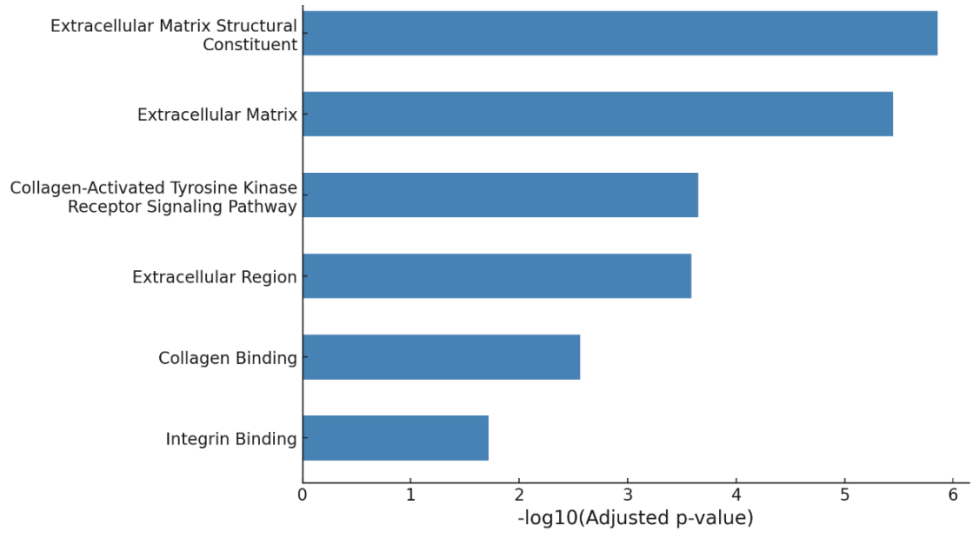

Appentix 3. Proteomic analysis of dECM1. Bar plot showing the top Gene Ontology (GO) terms enriched among proteins identified in the dECM1 sample using LC-MS/MS. Bar height represents statistical significance as –log10(adjusted p-value), based on GO enrichment analysis performed with g:Profiler.

APPENDIX 4

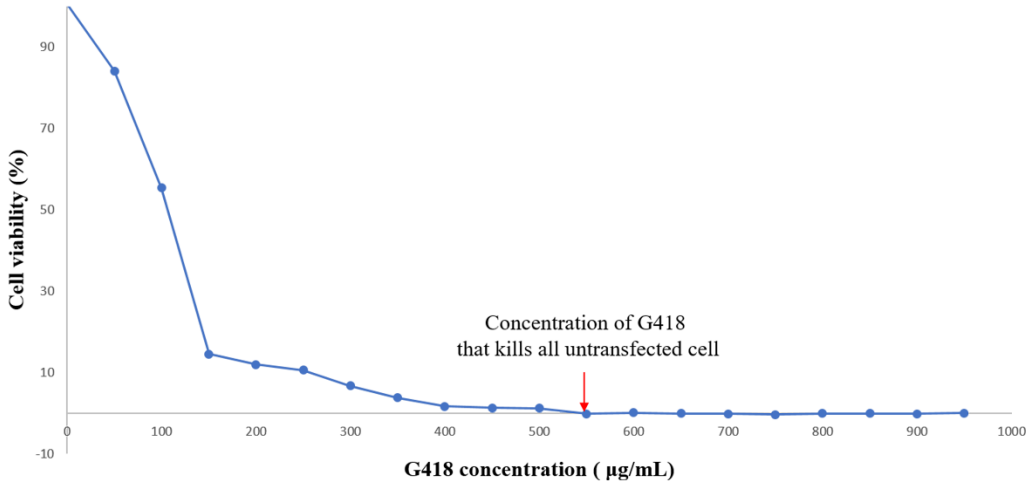

Appentix 4. Kill curve determination. U87 kill curves were constructed at day 10 using a range of G418 concentrations.

APPENDIX 5

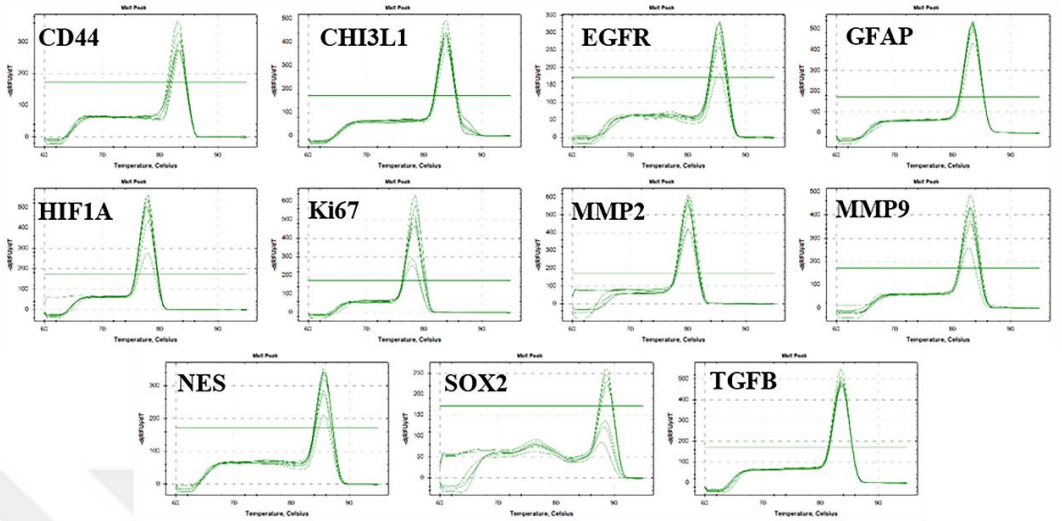

Appentix 5. Melting curve analysis from the real time PCR assay.

9 CURRICULUM VITAE